Doctoral Dissertations        Student Scholarship

Spring 2002

# Application of characteristic mode analysis to variable antenna placement on devices operating in the near -resonant range

David Anthony Strohschein
*University of New Hampshire, Durham*

Follow this and additional works at: https://scholars.unh.edu/dissertation

# INFORMATION TO USERS

This manuscript has been reproduced from the microfilm master. UMI films the text directly from the original or copy submitted. Thus, some thesis and dissertation copies are in typewriter face, while others may be from any type of computer printer.

**The quality of this reproduction is dependent upon the quality of the copy submitted.** Broken or indistinct print, colored or poor quality illustrations and photographs, print bleedthrough, substandard margins, and improper alignment can adversely affect reproduction.

In the unlikely event that the author did not send UMI a complete manuscript and there are missing pages, these will be noted. Also, if unauthorized copyright material had to be removed, a note will indicate the deletion.

Oversize materials (e.g., maps, drawings, charts) are reproduced by sectioning the original, beginning at the upper left-hand corner and continuing from left to right in equal sections with small overlaps.

Photographs included in the original manuscript have been reproduced xerographically in this copy. Higher quality 6" x 9" black and white photographic prints are available for any photographs or illustrations appearing in this copy for an additional charge. Contact UMI directly to order.

# Application of Characteristic Mode Analysis to Variable Antenna Placement on Devices Operating in the Near-Resonant Range

BY

David A. Strohschein

B.S., University of Utah (1988)
M.S., University of Utah (1994)

DISSERTATION

Submitted to the University of New Hampshire
in partial fulfillment of
the requirements for the degree of

Doctor of Philosophy

in

Engineering: Electrical

May 2002
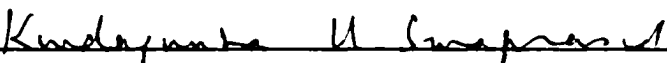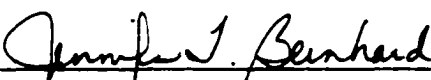
UMI Number: 3045340

# UMI®

UMI Microform 3045340

ProQuest Information and Learning Company
300 North Zeeb Road
P.O. Box 1346
Ann Arbor, MI 48106-1346

This dissertation has been examined and approved.
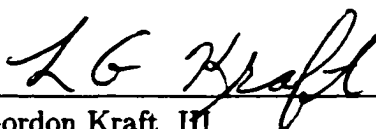
_Kondagunta U. Sivaprasad_
Dissertation Director, Kondagunta U. Sivaprasad
Professor of Electrical Engineering

_Jennifer J. Bernhard_
Jennifer T. Bernhard
Adjunct Assistant Professor of Electrical Engineering

_Kelly Black_
Kelly J. Black
Associate Professor of Mathematics

_Michael J. Carter_
Michael J. Carter
Associate Professor of Electrical Engineering

_Kent Chamberlin_
Kent A. Chamberlin
Professor of Electrical Engineering

_L. Gordon Kraft_
L. Gordon Kraft, III
Professor of Electrical Engineering

4/24/02
Date

# Dedication

To Mom and Dad.

.

# Acknowledgments

I would like to thank Dr. Sivaprasad, Dr. Bernhard and my other committee members. I would also like to thank Dick Austin of Austin Antenna, Bob Champlain of the Kingsbury Machine Shop. and John Rockway and Jim Logan of EMSci. Inc for their donation of time. expertise. and the software. EMBPro. Finally, I would like to especially thank my wife. Michele. who has always provided her support and understanding during this lengthy process.

iv

# CONTENTS

v

# LIST OF TABLES

viii

# LIST OF FIGURES

x

# ABSTRACT

APPLICATION OF CHARACTERISTIC MODE ANALYSIS TO VARIABLE ANTENNA
PLACEMENT ON DEVICES OPERATING IN THE NEAR-RESONANT RANGE

by

David A. Strohschein

University of New Hampshire, May, 2002

As antenna sizes on portable wireless devices decrease to the dimensions of the device itself and to that of the operating wavelength, the system begins to operate in the near-resonant frequency range. Currently, a straightforward synthesis approach for determining optimal antenna placement within such near-resonant range systems does not exist. Previously, characteristic mode analysis had only been applied to systems with constant geometry that operated in the near-resonant range and the system had constant characteristic modes independent of the probe location. Successful application of characteristic mode analysis to radiating systems with a constant characteristic mode response suggest that a similar technique may be useful for antenna placement in systems that exhibit a variable characteristic mode response to antenna position.

In this research, we investigate system characteristic mode response to variable antenna placement in systems operating in the near-resonant frequency range where the dimensions of the antenna and wireless device are both comparable to a wavelength. To achieve this, new characteristic mode software was developed and a number of dynamic systems composed of a driven dipole antenna positioned close to either a wire or planar arrangement of parallel wires, simulating the antenna / wireless device system, were studied and their computational and experimental results were obtained. The results clearly demonstrate, that as expected, the dominant system characteristic modes are dependent upon antenna position due to the interaction between the antenna and the device. Additionally, these results suggest that a knowledge of the isolated characteristic modes, the geom-

etry of the antenna, and the non-driven portion of the structure may be sufficient to predict the

behavior of the characteristic mode response of the system to an antenna repositioned above the

non-driven structure. In conclusion, this work establishes the foundation for the development of

an antenna placement algorithm for systems operating in the near-resonant range with variable an-

tenna placement by examining the relationship between antenna position and the variation of the

system characteristic modes.

.

# Chapter 1
# INTRODUCTION

An antenna system's radiation pattern depends on the shape of the antenna and its immediate surroundings. The ratio of antenna size to the size of the device upon which it is mounted varies considerably across applications. In some cases the antenna is much larger than the device upon which it is mounted (e.g., a whip antenna for a 3-30MHz portable backpack radio). In other cases, the antenna is small compared to the structure upon which it is mounted as in the case of a car-mounted GPS antenna. Additionally, there are cases when size of the antenna and the device upon which the antenna is mounted are comparable to the operating wavelength. One such example is an antenna mounted on a laptop computer that operates as part of a wireless local area network (WLAN) in the 2.45GHz range. In such cases, antenna position has considerable impact on the radiation pattern of the antenna / laptop combination [1],[2].

In many instances, the position of the antenna on the radio or the supporting structure makes little difference in terms of the far-field pattern or in terms of design requirements. However, for systems operating in the near-resonant range this is not true. In this case, the relative positions of the antenna with respect to the radio or mounting structure impacts the pattern significantly, as the geometry of the antenna / device system varies when the antenna is repositioned. As the first step in understanding how the antenna placement impacts this pattern, this work examines the application of the characteristic mode approach to systems that have more than one potential antenna location.

Until recently, antenna placement, particularly on consumer wireless devices, was not a great concern due to the size of the antenna with respect to the device size and operating wavelength. However, as we use systems that operate in the near-resonant range, the importance of proper

1

antenna placement is demonstrated by its direct effect on the antenna pattern [1],[2],[3].

Because of the relative size of the antenna, the device, and the operating wavelength of interest, the radiation pattern from the device and the antenna is not simply a function of the antenna alone. Rather, the pattern results from the interaction between the antenna, the object's shape and the antenna's location on the object. This knowledge provides the antenna designer with a certain degree of control over the radiation pattern by varying the position of the antenna on the object. By allowing the antenna to be placed in one of several potential locations, the problem becomes one of pattern generation from a variable geometry system. A variable system geometry means that the total geometry changes due to the relocation of the antenna. Antenna placement within such a geometry can be determined using one of a number of approaches.

## 1.1 Antenna Positioning

Antenna positioning problems can be divided into the following two classes: those where design requirements fix the location of the antenna on the object and those where the system design provides sufficient latitude in antenna position. Those systems with a fixed or defined antenna position on the object shall be defined as static geometry problems, while those systems with several potential antenna locations shall be considered as variable geometry problems.

Given a dynamic geometry problem, a designer may use one or a combination of the following approaches for obtaining an antenna placement solution. These methods are the approximation method, the intuitive method and the multiple-location approach.

The approximation method treats the problem as either a low-frequency (LF) or a high-frequency (HF) problem. In the low-frequency (LF) range, the object or chassis upon which the antenna is mounted is typically at least an order of magnitude smaller than the wavelength of the frequency

2

of operation. Additionally, the antenna size is usually on the order of a wavelength. In this case, the antenna is mounted or positioned in such a way that the presence of the device does not significantly distort the far-field antenna pattern from that of the antenna's free-space pattern. Instead the device appears as a load on the antenna and thereby changes the antenna's input impedance at the feed point. The low-frequency approximation suggests that the electrical presence of the device can be largely ignored when calculating the far-field pattern of the system. This approach is not appropriate for the present system under study since the device, antenna, and operating wavelength are comparable in size.

In the high-frequency (HF) range, the antenna is typically mounted on an object much larger (at least an order of magnitude) than the wavelength of operation. Additionally, the antenna is much smaller than the size of the mounting object. Then techniques such as the Geometric Theory of Diffraction (GTD) and the method of images provide reasonable approximations of the actual radiation pattern.

The intuitive approach relies upon the designer's experience related to antenna placement. In this case the designer draws upon his / her experience in similarly constrained systems in positioning antennas. However, this skill is not easily transferable between individuals and can take years to develop.

Finally, the multiple location approach can be a combination of simulation and experimental brute-force studies. The antenna can be modeled at one or several locations and then the resultant radiation pattern is computed. Likewise, the antenna can be physically positioned on the device in each of several different locations and the resultant pattern is measured. The antenna is then positioned at the location that provides the best approximation to the desired pattern. Depending on the resources and time available, this method can be time consuming and prove to be an inefficient way

3

to determine antenna position. This method typifies the *analysis* approach to antenna placement. A much better approach would be to calculate or synthesize a solution using a functional relationship between the desired radiation pattern and the electromagnetic characteristics of the isolated antenna and the isolated device. However, a straight forward *synthesis* approach for determining antenna placement within dynamic near-resonant systems currently does not exist.

We propose using characteristic modes as the basis for such an approach. This work is the first step towards developing a characteristic mode-based algorithm for antenna placement within near-resonant range dynamic systems. The following section defines the near-resonant range and the implications of operating within this range.

## 1.1.1 The Near-Resonant Range

As operating frequencies increase to hundreds of MHz or low GHz with wavelengths from tens of centimeters to a few centimeters and antenna size decreases to centimeters, the antenna size becomes of the same order as the wavelength of operation. Additionally, the device size (e.g., the typical cellular phone, PDA, or laptop computer) is now of the same order as the operating wavelength. When an antenna that has size of the order of a wavelength and is positioned on a portable device of similar size, the system operates in the near-resonant range. In such a system, the richness of the electromagnetic interaction of the antenna and the device results in a radiation pattern that is typically inadequately modeled using the approximations inherent to either high or low-frequency analysis. Due to the near-resonant size of the device, it cannot be modeled as either an electrically-small or electrically-large conductor in the presence of an antenna. Similarly, the system radiation pattern cannot be accurately modeled using the radiation pattern of an antenna above an infinite ground plane. Instead, the device itself is a near-resonant-sized structure capable

4

of resonating and radiating energy supplied by the antenna.

The system becomes one of a near-resonant length parasitic element (the device) positioned very close to the driven antenna (the antenna proper). The problem now becomes one of analyzing a system of two antennas, one driven and one passive, positioned close to each other. Therefore, the placement of the antenna on the device can significantly impact the system's radiation pattern in a manner similar to placing a driven antenna near a parasitic antenna of similar size.

## 1.2 Synthesis vs. Analysis

Comparison of an analysis-based approach and a synthesis-based approach for antenna placement begins with a review of the multiple-location based approach, an analysis-based approach. The multiple-location approach relies on a computational or experimental brute-force approach that evaluates the radiation pattern obtained for antenna placement at several uniformly distributed sites across the device with the desired radiation pattern. However, even this approach lacks efficiency. The inefficiency stems from the fundamental approach to the problem: these methods rely on the *analysis* of the radiation patterns generated at each of several antenna positions. A much more efficient way to determine antenna placement is to calculate or synthesize a solution based on knowledge of the system.

Analysis of the pattern generated by an antenna at a specific position on the device can be performed using methods such as the Finite-Difference Time Domain (FDTD) method or the Method of Moments (MoM). However, as previously described, these are "brute force" approaches. This begs the question, " Is there a more efficient way to determine antenna placement on a device for a system operating in this range?" As more and more systems begin to operate in the near-resonant range and the demand for more controlled radiation increases, there will be a similar demand for

5

more efficient ways to determine antenna placement in these systems. Therefore, the development of a paradigm or computational process that simplifies the process of determining antenna placement would be very useful.

A more efficient method would *synthesize* a solution instead of analyzing several potential ones. A synthesis approach would make use of the quantitative relationship between antenna position on a device and the resultant radiation pattern. Application of this relationship would then determine the proper location of the antenna. A synthesis approach strives to compute a solution from our knowledge of the system rather than pick the best solution from a limited number of possibilities, as seen in the analysis method.

Therefore, a synthesis approach relies on quantifying the relationships between antenna placement on an object and the resultant radiation pattern. A review of FDTD and MoM suggests that the MoM approach may be useful in addressing this requirement. MoM uses a linear algebra-based approach to describe and solve the relationship between the electric fields and currents associated with the structures under study. Additionally, forming algebraic relationships between the constants and variables of the problem enables the application of standard linear algebra and optimization methods to solve such problems.

Such a synthesis approach has been applied to a system operating in the near-resonant range and that has a geometry that remains constant, despite feeding or probing the structure at one or more locations [4]. This approach used characteristic modes (CM) to solve this problem. This was the motivation for a similar synthesis approach using CM analysis for systems operating in the near-resonant range that have an antenna repositionable to one of several locations within the system.

6

## 1.3 Characteristic Modes

Characteristic modes are based on an eigenvalue /eigenvector analysis of the MoM matrix relationships describing the system. This analysis creates a set of basis functions. From the electromagnetic point of view, a weighted sum of these basis functions approximates any surface current distribution that can be supported by the system when it is probed or fed at a specific frequency. Similarly, the far-field radiation pattern of the system is a weighted sum of the patterns generated by each of the characteristic modes. While not every possible pattern can be generated, by appropriately weighting and summing these modes, the resulting system pattern approximates the desired pattern to the best of the system's ability to generate such a pattern. The basis function approach has been used successfully to determine where to feed a structure to generate an approximation to a desired radiation pattern or to obtain maximum coupling between the power fed into the system and the power radiated[5],[4]. These results suggest that a similar approach can be applied to systems with dynamic geometry.

## 1.4 Objectives of this Work

Determination of antenna placement using characteristic modes for dynamic geometries for systems operating in the near-resonant (NR) range requires examination of a number of issues. Foremost is the analysis of the interaction between antenna placement and changes in the system's characteristic mode response. To analyze the interaction of one antenna and structure effectively, a study of the characteristic modes of an isolated dipole, isolated wire and isolated rectangular plates was first undertaken. Then the study was extended to analyze the characteristic modes of systems created from combinations of the isolated structures. This enabled us to compare those portions

7

of the system's modes that lie on the antenna, wire, and plate with the characteristic modes of the isolated dipole, wire, and plate.

Using this work as a foundation, the relationships between antenna position, characteristic mode shape, and antenna system geometry may be formulated into a unified, generalizable approach. This synthesis-based approach will enable the engineer to specify the desired antenna location on an object to obtain an approximation to the desired system radiation pattern to the best of the ability of the system to generate the desired pattern.

## 1.5   Outline

Chapter 2 (Background) begins with a discussion of the antenna / object electromagnetic environment. The object can be thought of as the device upon which the antenna is mounted. This discussion is a review of the method of moments as it applies to antenna radiation analysis / prediction. Following this review is a discussion on characteristic mode analysis. The chapter concludes with an examination of previous applications of characteristic mode analysis to antenna problems.

Chapter 3 (Methods) examines, in detail, the application of characteristic modes to the near-resonant dynamic geometry problem at hand. Additionally, this chapter discusses the specific tasks of the research, how they were addressed, the development of computational tools, and the laboratory methods. Chapter 4 (Results) describes how these methods were applied to obtain data from both measurements and simulations. Additionally, data obtained from this work is presented and discussed. The dissertation concludes in chapter 5 with conclusions for the work and suggestions for future work.

8

# Chapter 2
# BACKGROUND

The power of characteristic mode analysis cannot be fully appreciated without first understanding the method of moments approach. As shall be shown, characteristic-mode analysis transforms the method-of-moments analysis results into a more useful product. The power of this transformation lies in its capability to delineate the relationship between a structure, its surface current distribution, and the resulting radiation pattern in a efficient manner based on orthogonal functions. Additionally, the characteristic mode approach provides a better understanding of how the characteristic modes of the isolated antenna and the device are modified as the antenna and the device become collocated. This information will be helpful in positioning an antenna in the proximity of a portable electronic device chassis so that the combination of the antenna and the chassis produce a desired radiation pattern.

## 2.1   Method of Moments

The method of moments (MoM) is useful for solving the following type of equation [6].

$$L(f) = g \qquad (1)$$

where $L()$ is a linear operator, $g$ is the known variable, and $f$ is the unknown vector. The power of the method of moments lies in its capability to solve the continuous equation (1) using a linear algebraic approximation. Once written as a set of linear equations, a new set of mathematical tools and approaches, such as eigenvalue / eigenvector analysis (characteristic mode analysis) can be applied. As antenna problems in the near-resonant range lend themselves to being cast in the form of equation (1), MoM is useful technique for antenna analysis.

9

MoM is based on the idea that a continuous function can be approximated by an appropriately scaled and summed set of 'test functions'. Consider the function $f$, from equation (1), approximated by $\hat{f}$ from the approximation

$$f \approx \hat{f} = \sum_{n=1}^{N} a_n f_n \tag{2}$$

where $a_n$ is a scaling factor or constant and $f_n$ is a *test or expansion function*. A graphical interpretation is shown in Figure 1.
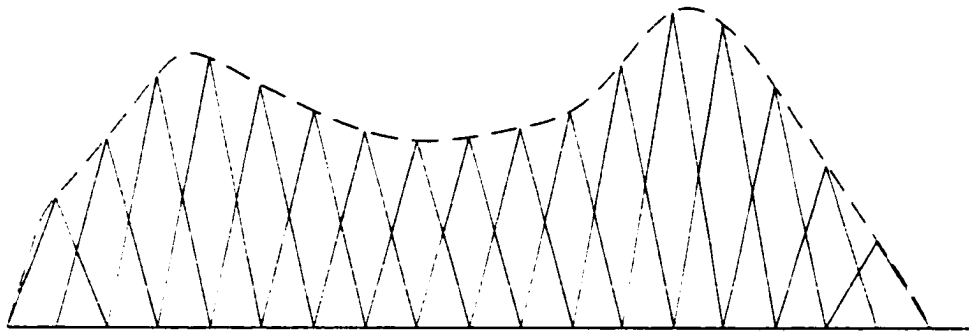


Figure 1:Approximation of a smooth function using the weighted sum of triangular test functions.

The desired function $f$ is the continuous function, represented by the dashed line, and $f_n$ represents one of the triangular test functions. Summing the shifted triangular functions produces the approximation, $\hat{f}$, of $f$.

Consider the following: if $f$ is the function we wish to approximate, then the residual error of approximation, $R$, may be written as

$$R = \sum_{n=1}^{N} a_n f_n - f. \tag{3}$$

By appropriately choosing $a_n$, the error between $f$ and $f_n$ will be zero only at the center of $f_n$. This is the *point matching* method. However, the error between these points is unknown. This error can

10

be minimized, in an average sense, by using the method of weighted residuals [7]. This method is based on the introduction of an additional set of functions $\{w_m\}_{m=1}^{N}$. These *weighting functions* may be delta functions, sinusoids, the same functions as $f_n$ or some other finite length function. Additionally, the inner product of $R$ and $w_m$, $\langle R, w_m \rangle$, is defined as follows:

$$\langle R, w_m \rangle = \int \int (R \bullet w_m) \, ds. \tag{4}$$

If the $f_n$ are orthogonal functions and $w_m$ are the same set of functions as $f_n$, then $R$ can be minimized, in an average sense, by using the following equation [8],[9]:

$$\langle R, w_m \rangle = 0. \tag{5}$$

Substituting the function $g$ from equation (1) for the function $f$ in equation (3) and including the effects of the $L$ operator on the product $a_n f_n$ equation (6) is obtained.

$$R = \sum_{n=1}^{N} a_n L\left(f_n\right) - g \tag{6}$$

Taking the inner product of both sides of equation (6) with respect to $w_m$ results in the following expression:

$$\langle w_m, R \rangle = \sum_{n=1}^{N} a_n \langle w_m, L\left(f_n\right), \rangle - \langle w_m, g \rangle = 0. \tag{7}$$

Rearranging this equation yields

$$\sum_{n=1}^{N} a_n \langle w_m, L\left(f_n\right), \rangle = \langle w_m, g \rangle. \tag{8}$$

To write this expression in a more compact and usable form, the following substitutions are made,

$$l_{mn} = \langle w_m, L\left(f_n\right) \rangle, \tag{9}$$

$$g_m = \langle w_m, g \rangle. \tag{10}$$

11

Substitution of equations (9) and (10) into equation (8) yields the following equation

$$\sum_{n=1}^{N} a_n l_{mn} = g_m \tag{11}$$

In matrix form this equation can be written as

$$[l][a] = [g] \tag{12}$$

where

$$[l] = \begin{bmatrix} \langle w_1, L(f_1) \rangle & \cdots & \langle w_1, L(f_N) \rangle \\ \vdots & \ddots & \vdots \\ \langle w_M, L(f_1) \rangle & \cdots & \langle w_M, L(f_N) \rangle \end{bmatrix}, \tag{13}$$

$$[a] = \begin{bmatrix} a_1 \\ \vdots \\ a_N \end{bmatrix}, \tag{14}$$

$$[g] = \begin{bmatrix} \langle w_1, g \rangle \\ \vdots \\ \langle w_M, g \rangle \end{bmatrix}. \tag{15}$$

Rearranging equation (12) to solve for $a$ yields the following expression:

$$[a] = [l]^{-1}[g]. \tag{16}$$

Values for $a_n$ can then be substituted into equation (2) to compute the approximate function $\tilde{f}$.

## 2.1.1 Application of the Method of Moments to Antennas

The previous section demonstrates how the method of moments can be applied to problems of the type generalized by equation (1). Equations solvable by MoM are frequently encountered in the study of antennas. One such equation is Pocklington's integral equation [8]. This equation relates the surface current on an antenna with the impressed or incident electric field, $E^i$.

A wire antenna has two fields associated with it: $E^i$ and the scattered or radiated electric field, $E^s$. Due to boundary conditions (Appendix A), the following equation must hold.

$$E^i_{\text{tan}} + E^s_{\text{tan}} = 0 \tag{17}$$

For a thin, linear antenna of length $L$ parallel to the $z$-axis, the general form of the expression

12

for $E^s$ can be written as [8]

$$E^s = E_z = \frac{1}{j\omega\varepsilon_o} \int_{-\frac{L}{2}}^{\frac{L}{2}} I\left(z'\right) \left(\frac{\partial^2}{\partial z^2}\psi(z,z') + \beta^2\psi(z,z')\right) dz'. \tag{18}$$

Where $I\left(z'\right)$ represents the value of the current at location $z'$ along the antenna. The function $\psi(z,z')$ is the free-space Green's function defined as follows:

$$\psi(z,z') = \frac{e^{-j\beta R}}{4\pi R}. \tag{19}$$

Where $R$ is defined as

$$R = \sqrt{(x-x')^2 + (y-y')^2 + (z-z')^2}. \tag{20}$$

The coordinates $(x', y', z')$ are those of the source location, while coordinates $(x, y, z)$ are those of the observation point. Combining equations (17) and (18) produces the following equation well known Pocklington's equation:

$$E_z^i = -\frac{1}{j\omega\varepsilon_o} \int_{-\frac{L}{2}}^{\frac{L}{2}} I\left(z'\right) \left(\frac{\partial^2}{\partial z^2}\psi(z,z') + \beta^2\psi(z,z')\right) dz'. \tag{21}$$

Equation (21) is used to calculate the surface current on the antenna from the impressed or incident electric field on the antenna. The impressed field is generated due to the voltage applied across the antenna terminals. Now let

$$K(z,z') = \frac{1}{j\omega\varepsilon_o} \left(\frac{\partial^2}{\partial z^2}\psi(z,z') + \beta^2\psi(z,z')\right).$$

Using this substitution in equation (21) results in the following simplified expression

$$E_z^i = -\int_{-\frac{L}{2}}^{\frac{L}{2}} I\left(z'\right) K(z,z')dz'. \tag{22}$$

The current function, $I\left(z'\right)$, can be approximated by a summation similar to the approximation of equation (2). However, in this case $\{I_n\}_{n=1}^{N}$ are the scaling factors and $\{F_n(z')\}_{n=1}^{N}$ are the test functions. This approximation is written as

$$I\left(z'\right) \approx \sum_{n=1}^{N} I_n F_n(z')$$

13

where $F_n(z')$ is defined as

$$F_n(z') = \begin{Bmatrix} 1 & \text{for } z' \text{ in } \Delta z'_n \\ 0 & \text{otherwise} \end{Bmatrix} \tag{23}$$

and each of the $N$ segments along the wire has length $\Delta z'_n$. This assumes that the antenna, of length $L$, is divided into segments of length $\Delta z'$ where $\Delta z' \ll \lambda$ and $\Delta z' \ll L$. Note for this example that the test functions are orthogonal pulse functions. However, the test function could just as easily have been a triangle or sine function. Substituting these relationships into equation (22) results in

$$E_z^i \approx - \int_{-\frac{L}{2}}^{\frac{L}{2}} \sum_{n=1}^{N} I_n F_n(z') K(z, z') dz'. \tag{24}$$

This equation is further simplified by writing it in terms of the contribution to the impressed electric field from each of the segments. Incorporating this simplification and the nature of the function $F_n(z')$ yields

$$E_z^i(z_m) \approx - \sum_{n=1}^{N} I_n \int_{\Delta z'_n} K(z_m, z') dz'. \tag{25}$$

Where $E_z^i(z_m)$ is the incident field located on the wire segment at $z_m$. The integral portion of this equation is simplified with the substitution

$$f(z_m, z'_n) = - \int_{\Delta z'_n} K(z_m, z') dz'. \tag{26}$$

Utilizing this substitution, the summation may be written as

$$E_z^i(z_m) \approx \sum_{n=1}^{N} I_n f(z_m, z'_n). \tag{27}$$

Substituting

$$Z_{mn} = f(z_m, z'_n) \tag{28}$$

and

$$V_m = E_z^i(z_m) \tag{29}$$

into the $E_z^i(z_m)$ expression results in the following matrix equation:

$$[Z_{mn}][I_n] = [V_m]. \tag{30}$$

14

From this relationship, the current distribution can be obtained by rearranging the equation and solving for the unknown current matrix. A further benefit of this approach is the generation of the $[Z_{mn}]$ or the impedance matrix. This matrix relates the electric field on any segment with the current on any other segment on the antenna. If $[Z_{mn}]$ is formed using the Galerkin approach [9](the weighting function is the same as the testing function) then the impedance matrix possesses certain qualities that will be discussed in the next section. These qualities enable eigenanalysis of the system. Such analysis is the core of the characteristic mode approach.

## 2.2 Characteristic Mode Analysis

Characteristic mode analysis is simply eigenanalysis. While the matrix relations obtained from the method of moments provide the relationship between the generated electric fields and the currents, eigenanalysis provides a compact way of expressing this relationship using orthogonal functions. The benefits of this orthogonality are discussed below. However, the mathematics behind eigenanalysis and characteristic modes are reviewed first.

### 2.2.1 Determination of Eigenvalues

The eigenvalues and eigenvalues of a matrix are identified by the following equation

$$Ax = \lambda x \tag{31}$$

Rewriting this equation yields

$$(\lambda I - A)x = 0, \tag{32}$$

where $I$ is the identity matrix. Taking the determinant of the matrix within the parentheses computes the eigenvalues, $\lambda$. This is shown by

$$\det(\lambda I - A) = 0. \tag{33}$$

15

The eigenvectors or characteristic modes can then be calculated using the eigenvalues.

In general, eigenvalues and eigenvectors form a compact notation for describing certain aspects regarding the "dynamics" of a system. Applied to mechanical systems, these dynamics describe the vibrations or the dynamic modes associated with a structure. In electromagnetic systems, the characteristic mode analysis links surface current distribution with both the impressed and radiated electric fields.

In the early 1970s, Harrington and Mautz [10] broadened the application of eigenanalysis as it applies to radiating structures by expanding the characteristic mode work of Garbacz [11] and Garbacz and Turpin [12]. Their work resulted in a simpler theory to compute the characteristic or eigenfunction modes of arbitrarily shaped objects.

As described in [10], knowledge of the impedance matrix, $[Z]$, from the following equation that relates the surface current distribution, $J$, and $[Z]$, with the impressed or applied electric field, $E$, on the antenna can be used to determine the eigenvalues and eigenvectors of the system,

$$[Z] J = E. \tag{34}$$

Using the impedance matrix as a starting point, a generalized eigenequation that relates $[Z]$ to the eigenvalues and the eigenvectors is introduced. The authors express this relationship with the following equation,

$$Z J_n = \nu_n M J_n. \tag{35}$$

where $\nu_n$ are the eigenvalues, $J_n$ are the eigenvectors or characteristic modes and $M$ is a rotation matrix. Choosing the matrix, $M$, to be a symmetric matrix such that

$$M = R \tag{36}$$

yields orthogonality of the far-field radiation patterns produced by the characteristic modes [10].

16

The $Z$ matrix is generated using the Galerkin method (testing and weighting functions are the same). As a result, $Z$ is symmetric and invertible. Additionally, Harrington sets

$$Z = R + jX \tag{37}$$

such that $R$ and $X$ are real matrices and

$$\nu_n = 1 + j\lambda_n. \tag{38}$$

Combining these relationships with equations (36) and (35) results in the following equation:

$$(R + jX)\,J_n = (1 + j\lambda_n)\,RJ_n. \tag{39}$$

This equation simplifies to

$$XJ_n = \lambda_n RJ_n. \tag{40}$$

This reduced expression yields a new expression with eigenvalues $\lambda_n$ and the same eigenvectors. Rearranging equation (40) results in the expression

$$R^{-1}XJ_n = \lambda_n IJ_n. \tag{41}$$

While this form is not the same form as equation (32), it still provides a mathematical relationship between the eigenvalues, eigenfunctions, and the resistance and the reactance of the impedance matrix. It is also important to note that the $J_n$ are orthogonal to one another. The importance of this orthogonality is discussed in the next section.

A second paper by Harrington and Mautz [13] addresses the calculation and evaluation of characteristic modes. The methods discussed here and in [13] form the basis for the software developed as part this research. Software development is described in the Chapter 3 of this dissertation.

## 2.2.2 Approximating a Function

Any function within a function space can be generated by a weighted sum of orthogonal functions spanning the space. Therefore, any surface current that can be supported by a structure can

17

be expressed as a weighted sum of the orthogonal functions, the characteristic modes, that span the set of possible surface current distributions on the structure. Similarly, using only a subset of these characteristic modes approximates the surface current distribution. While this is an interesting result mathematically, it is even more interesting in terms of pattern synthesis.

Harrington and Mautz [10] show that the far-field power radiated by each characteristic mode is orthogonal to the power radiated by every other characteristic mode. Therefore, the total far-field power radiated by an excited structure can be expressed by

$$P_d = \sum_{n=1}^{N} a_n p_n, \tag{42}$$

where $P_d$ represents the total far-field power pattern and $a_n$ is the weight of a far-field power pattern $p_n$ produced by the $n$th characteristic mode. This equation is a powerful result in terms of functional analysis. Using error-minimization techniques for linear systems, the relative weighting of each eigenfunction or characteristic mode can be calculated so that the sum approximates the desired pattern. Understanding the orthogonal nature of the characteristic mode currents and patterns is fundamental to understanding the next section.

Characteristic mode orthogonality enables the total surface current density on a structure to be expressed as a weighted sum of eigencurrents or characteristic modes. This is shown by

$$J = \sum_{n=1}^{N} a_n J_n, \tag{43}$$

where $a_n$ is a scaling factor and $J_n$ are the eigencurrents of the object. Varying the feed location on the structure determines the degree to which each characteristic mode is excited ($a_n$) and, therefore, the degree to which the mode radiates.

Let the expression $[Z] J$ in equation (34) be replaced by a linear operator $L$ such that the fol-

18

lowing equation is true.

$$LJ = E^i \tag{44}$$

where $E^i$ is the *impressed electric field* which, for a radiation problem, is the electric field on the antenna due to excitation at various points on the structure or antenna. Typically, but not necessarily, this refers to a single point of excitation on the antenna, for example, the transmission line feedpoint. The location and magnitude of the excitation points define the elements of the array $E^i$.

Substituting equation (44) into equation (43) results in

$$\sum_{n=1}^{N} \left(a_n L J_n - E^i\right) = 0. \tag{45}$$

To simplify this equation, the inner product of each of the arguments of the summation is calculated as follows:

$$\sum_{n=1,\, n \neq m}^{N} a_n \langle J_m L J_n \rangle - \langle J_m E^i \rangle = 0. \tag{46}$$

Noting that $L = Z$ the following equation is derived

$$\sum_{n=1}^{N} a_n \langle J_m Z J_n \rangle = \langle J_m E^i \rangle \tag{47}$$

Due to orthogonality relationships of $J_m$, $Z$, and $J_n$ [10] the following expression is true:

$$\langle J_m Z J_n \rangle = (1 + j\lambda)\,\delta_{nm}, \tag{48}$$

where

$$\delta_{nm} = \left\{ \begin{array}{ll} 1 & \text{for } n = m \\ 0 & \text{for } n \neq m \end{array} \right\}.$$

Substituting equation (48) and taking into account the qualities of $\delta_{nm}$ equation (47) reduces to

$$a_n(1 + j\lambda) = \langle J_n E^i \rangle, \; \forall\, n. \tag{49}$$

The term $\langle J_n E^i \rangle$ is the *modal excitation* and its value is computed by the following equation.

$$V_n^i = \langle J_n E^i \rangle = \oint_s J_n \cdot E^i ds \tag{50}$$

19

This equation demonstrates the importance of the proper placement and magnitude of the elements of $E^i$. For $E^i$ generated by a single feed point, the magnitude of the modal excitation will vary in direct relation to the feed point's position with respect to the characteristic mode's magnitude. This array is one of two dominant factors that define the contribution of $J_n$ to the total surface current. Substituting the results of equations (49) and (50) into (43) results in

$$J = \sum_{n=1}^{N} \frac{V_n^i J_n}{(1 + j\lambda)} \tag{51}$$

This equation illustrates the second dominant factor in determining the contribution of $J_n$ to the overall surface current density; the second factor is $\lambda$. If $\lambda \gg 1$ then the contribution will be mostly imaginary ($J_n$ and $E^i$ are real and all $E^i$ are equiphase [10]). Alternatively as $\lambda$ approaches zero, the contribution of the particular $J_n$ will be mostly real. Since the electric and magnetic far-fields are linearly related to the currents the following equations are valid descriptions of these fields:

$$E = \sum_{n=1}^{N} \frac{V_n^i E_n}{(1 + j\lambda)} \tag{52}$$

and

$$H = \sum_{n=1}^{N} \frac{V_n^i H_n}{(1 + j\lambda)} \tag{53}$$

where $E_n$ and $H_n$ are the electric and magnetic far-fields generated by $J_n$ and $E$ and $H$ are the sum of the weighted electric and magnetic far-fields, respectively. Equation (52) illustrates the effect of varying $E_n$ and the impact of the magnitude of $\lambda$. Depending on the value of $\lambda$ and the composition of the array $E_n$, the overall electric field, $E$, can be controlled to a large degree. This result enables the synthesis of far-field patterns. The degree of approximation of the synthesized pattern to the desired pattern is limited by the shape of the original structure and the latitude in placement of field-excitation or probe points on the structure or the antenna. A simple example of how the overall surface current can be controlled by placement of the impressed field is demonstrated using

20

the example of the dipole antenna.

## 2.2.2.1 Characteristic Mode Analysis of the Dipole Antenna

In this example, a center-fed dipole of length $\frac{\lambda}{2}$ is considered. Figure 2 illustrates the first three dominant eigenvalues and their associated eigenvectors. With the feed placed at the center of the dipole antenna, the modal excitation factor for each of the first three modes is as follows.

| Eigenmode Order of Dominance | Eigenvalue | Modal Excitation Factor |
|---|---|---|
| $\lambda_1$ | 0.41 | 1.00 |
| $\lambda_2$ | -175.21 | 0.00 |
| $\lambda_3$ | -11465.44 | 1.00 |

Table 1:Dipole modal excitation factors.

The left hand column represents the eigenmodes arranged in their order of dominance. This order is based on the eigenvalue for each mode, the middle column. The data in the right hand column represents the degree of relative excitation of each mode (Modal Excitation Factor [14]). The Modal Excitation Factor is calculated using the following equation.

$$\frac{\{J_n(i) \mid i = probe\ location\}}{J_n\ max\ value} \tag{54}$$

This expression indicates the probe's ability to excite the mode when the probe is placed at a particular node location.

The characteristic modes associated with the first three dominant eigenvalues are shown in figure 2.
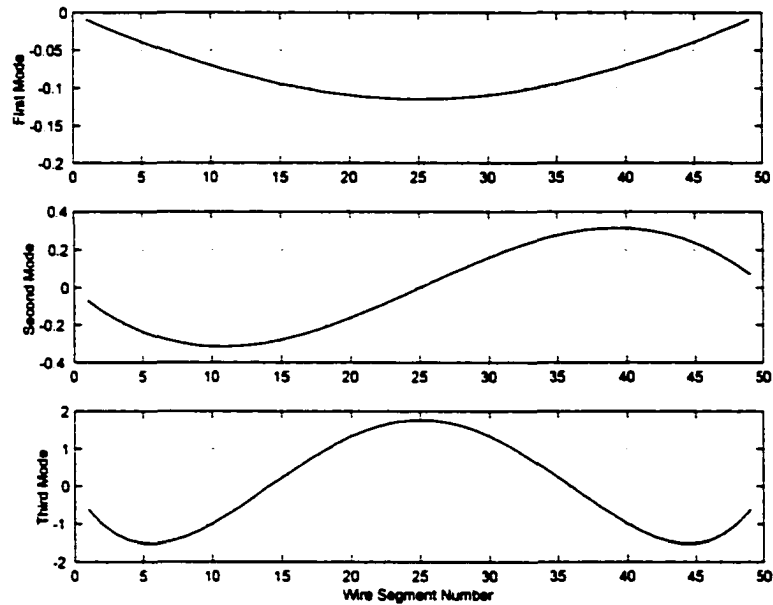
Figure 2:First three most dominant characteristic modes for the half-wave dipole antenna.

The segment number corresponds to ?n short current element that is one of many such elements that are used to model the current distribution across the antenna. Applying equation (51) to the characteristic mode data in Figure 2 in conjunction with probing or feeding the dipole in the center results in the "CM plot" data portion of Figure 3. The result is plotted with the more customary $\sin(x)$ current distribution across a half-wavelength dipole.

22
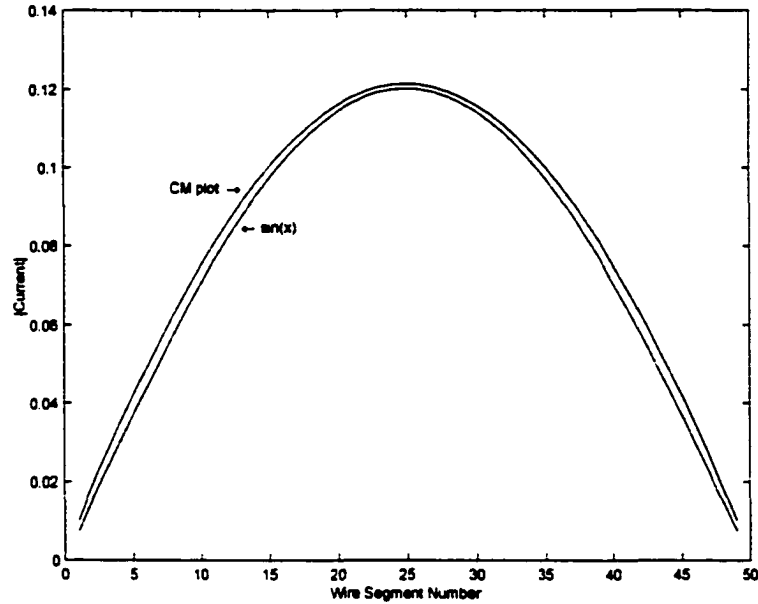
Figure 3:Comparison of current magnitude on a half-wave dipole using the characteristic mode approach versus a sine wave approximation.

Note, that despite the greater "maximum value" of the third characteristic mode, it had almost insignificant contribution to the overall current magnitude on the antenna (refer to Table (1)). This can be attributed to the magnitude of $|\lambda_3|$ versus $|\lambda_1|$, where $|\lambda_3| >> |\lambda_1|$, and from equation (51) the greater the $|\lambda|$ the less real contribution this characteristic mode has to the overall current on the object.

This section used a simple example to demonstrate the application of the characteristic mode approach to determine the total current distribution across a center-fed half-wavelength dipole antenna. Additionally, the results are in good agreement with a more traditional approach using a sinusoidal current distribution. This example helps to highlight the role that probe location plays in exciting various modes and also the contribution of those modes, based on their eigenvalues, to the overall current distribution on the structure. This introduction to the application of characteristic

23

modes to calculate surface current plays a central role in determining where to excite a structure to generate a desired radiation pattern or to maximize the coupling of feed power to radiated power.

## 2.2.3 Constant Geometry / Variable Probe Location

Recently Austin and Murray [4] and [14] applied characteristic modes to the problem of determining where to excite a structure in order to generate a desired radiation pattern. The structure consisted of a vehicle with a "loop-type" structure attached to the vehicle body. Both the vehicle and the loop are of near-resonant size. The authors' goal was to determine where to feed the combined loop / vehicle structure to generate a radiation pattern that approximated a desired radiation pattern. For a given geometry, characterized by its modes and driven at a particular frequency, there are only so many surface current distributions that can be generated. Therefore, only an approximate match to the desired pattern is possible due to the limitations of the fixed nature of the system geometry.

A wire-grid model of the loop and vehicle was created. Then the characteristic modes for the model were calculated. Since the modes are orthogonal, an error-minimization approach was developed to calculate the relative weighting of each mode. From this information the probe locations could then be determined. The following expression was used to calculate the error between the desired far-field and the actual pattern generated from the contribution of a particular mode:

$$e = \frac{\langle (E_A - E_D), (E_A - E_D) \rangle_{s_\infty}}{\langle E_D, E_D \rangle_{s_\infty}}, \tag{55}$$

where $s_\infty$ indicates that the fields were evaluated at an observation point at infinity, $E_D$ is the desired far-field pattern from the composite system of the vehicle and antenna, and $E_A$ is the actual pattern radiated by the system. Additionally, $E_A$ is defined as

$$E_A = \sum_{n=1}^{N} \alpha_n E_n, \tag{56}$$

24

where

$$\alpha_n = \frac{\langle E_D, E_n \rangle_{s_\infty}}{Z_o},$$ (57)

and

$$Z_o = 377\Omega.$$ (58)

The inner product is defined as

$$\langle E_D, E_n \rangle_{s_\infty} = \iint_{s_\infty} E_D \bullet E_n^* ds,$$ (59)

where $E_n$ is the radiation pattern generated by the characteristic mode, $J_n$.

Using an iterative error-minimization procedure [4],[14], the error is minimized until it is within an acceptable, pre-determined range. The resultant set of $\alpha_n$ can be used to determine the voltage feed locations and magnitudes. This is expressed as

$$\alpha_n = \frac{I_n^T V}{1 + j\lambda_n}$$ (60)

where $I_n$ are the mode currents, $V$ is the source voltage array, and $\lambda_n$ are the eigenvalues of the modes.

Using this approach, the authors synthesized feed locations to excite the structure for generation of the desired pattern. This work demonstrates the value of using characteristic modes to determine the probe location(s) for a static, near-resonant structure. But what happens in an environment where the antenna is repositioned, but is now electrically very small? This was the premise of work done by Newman[5].

## 2.2.4    Variable Geometry / Electrically Small Antenna

Characteristic modes have also been applied to systems that have a variable geometry, i.e. the antenna could be repositioned on a structure. However, in this case the structure was of near-resonant size and the antenna was electrically small and used essentially to make the structure

25

radiate. The structure studied by Newman [5] consisted of a loop antenna positioned at various locations on a simplified aircraft model. The model consisted of two wires crossing at right angles, representing the wings and body of an aircraft. Newman sought to determine the best of several positions to place the loop antenna so that the structure was maximally resonated and achieving maximum radiation from the system. His approach was based on positioning the antenna at several locations and analyzing the resulting excitation of each of the first four characteristic modes of the system.

Using a simple analysis of the dominant modes of the system at a particular frequency, Newman determined a location that he predicted would generate the most radiation compared to other positions. The loop antenna was used not as a radiator, due to its inefficiency, but, instead, as a 'probe' to excite the modes of the aircraft. Despite the physical presence of the loop antenna, Newman negates or assumes a minimum interaction (mutual impedance effect) between the loop antenna and the aircraft wire-grid model. The rationale behind this approach is better understood following a discussion of the impedance matrix's structure.

## 2.2.5   Impedance Matrix Composition

When considering the interaction between an structure and a near-by antenna, it is informative to look at the two cases when the structure and the antenna are isolated from each other and again when positioned near one another: an antenna placed somewhere on a portable device is illustrative of the latter case. In the first instance, wire-grid models for the antenna and the structure are created and their impedance matrices, $[Z_{ant}]$ and $[Z_{struc}]$ are computed. Then the antenna and the structure are positioned close to one another, such that they are considered one system. A new impedance matrix for the system, $[Z_{sys}]$, is computed.

26

Inspection of $[Z_{sys}]$ reveals that it can be divided into submatrices revealing the following structure:

$$[Z_{sys}] = \left[ \begin{array}{cc} [Z_{struc}] & [Z_{mut}] \\ [Z_{mut}] & [Z_{ant}] \end{array} \right].$$  (61)

Note that the submatrices along the diagonal are the original impedance matrices of the isolated structure and antenna, $[Z_{struc}]$ and $[Z_{ant}]$ respectively, while the off-diagonal matrices capture the mutual impedances between the antenna and the structure.

Two points can be drawn from this observation. First, regardless of the antenna's position with respect to the structure (or on the structure) the diagonal matrices are unaffected by the position of the antenna with respect to the structure. Second, if there is little interaction between the antenna and the structure, then no matter where the antenna is moved these off-diagonal matrices will show little change. If repositioning the antenna causes minor changes in the structure of the $[Z_{sys}]$ then the $\lambda$ and $\bar{\lambda}$ (eigenvalue and eigenvector, respectively) for this system will show little change. This apparently was the case for the antenna and the aircraft arrangement in Newman's study. Movement of the loop changed the $[Z_{sys}]$, but not sufficiently enough to change the characteristic mode response of the system. Instead of the loop being a far-field radiator, it acted as a probe having a predominately local excitation upon the aircraft's characteristic modes. Unfortunately, a similar simplification can not be made in this research. We are interested in both an antenna and structure that are of the same magnitude size in the near-resonant range. In this case, $[Z_{ant}]$ and $[Z_{struc}]$ have a much greater interaction leading to noticeable changes in the system characteristic modes as the antenna is repositioned.

### 2.2.5.1    Evolution of Characteristic Modes

The previous section examined the relationship of the modes of the isolated antenna and structure to the modes of the combined system. An antenna placement paradigm based on characteristic modes

27

requires a better understanding of the relationship between system characteristic modes with respect to antenna position, and to the modes of the isolated antenna and the structure. Ideally, such an investigation will identify associations or relationships between antenna position / structure shape and size, and thereby enable the formalization of such information into functional relationships. Such relationships could be incorporated into a standardized antenna placement paradigm for radiating systems that have a dynamic geometry and operate in the near-resonant region.

Reducing the necessary computations and obtaining a solution in a reasonable time using a standardized approach creates a compelling argument for using characteristic modes to determine antenna placement. However, this approach requires understanding of the relationship between antenna placement and the change in characteristic mode shape. Another possible approach is based on first obtaining characteristic mode information for the isolated structures. This information could then be used to predict the characteristic modes of a system composed of the formerly previously isolated structures. As a step toward this goal, this research creates tools for calculating the characteristic modes, visualizing these modes, and performing initial analysis of the modes. Application of characteristic modes to antenna placement within a system of dynamic geometry operating in the near-resonant range serves as an initial step toward formalization of an antenna placement paradigm based on characteristic modes.

28

# Chapter 3
# METHODS

## 3.1 Introduction

Accomplishing the research objectives required the development of several resources. These resources encompass both computational and experimental tools and their development plan is described here. Of paramount importance was the development of software to calculate the characteristic modes of wire-grid models of structures. Also, software needed to be developed to properly plot the distribution of characteristic modes in one and two dimensions. This enabled graphical evaluation of the modes and assisted in understanding how the modes of the system changed with respect to antenna position. The structures and systems under study were modeled using wire-grid models.

Additional software was written to evaluate the far-field based on the computed characteristic modes. The results from the characteristic mode analysis were then passed to software designed to compute the far-field radiation from arbitrarily oriented current distributions in three-dimensional space. In addition to the computer software, this project required the construction of a test system to measure the patterns generated from an antenna placed at multiple locations on a test structure.

While the computational portion of this research enabled prediction of system response and the pattern generated, the experimental work provided measurements for evaluating the prediction accuracy of the software. The combination of the computational and experimental approaches provided two major benefits. First, the accuracy of the computational model is verified by comparing the predicted radiation patterns with data obtained from antenna measurements. Additionally, fol-

29

lowing validation of the software for the calculation of the characteristic modes and the far-field radiation patterns, the computational approach could be used for accurate theoretical study of the characteristic modes and patterns of other systems.

## 3.2 Computational / Analytical Work

### 3.2.1 Characteristic Mode Calculation

The work of Harrington *et al* [13] provided the basis for the characteristic mode software. He presents an algorithm for calculating the characteristic modes of an object. However, Harrington's approach requires knowledge of the impedance matrix, $[Z]$. This matrix describes the relationship between the voltages and currents on the surface of the object(s). The matrix is one of the products from a method of moments analysis of the system. Harrington states that the impedance matrix will be symmetric due to electromagnetic reciprocity. In theory, the matrix will be symmetric if the Galerkin method is used to calculate $Z$. Recall that the Galerkin method requires that the testing and weighting functions used in the MoM analysis be the same function. Since several method of moment software packages exist, the decision was made to use one of them to calculate $Z$ rather than write and debug original code. However, this process was complicated by the requirement that the method of moment algorithm be based on the Galerkin method. Finally, Drs. Logan and Rockway at EMSci donated a modified version of their software package, Expert Mininec Broadcast Professional (ExpertMBPro). This version was able to generate the desired impedance matrix.

Concurrently, conversion of the algorithm from Harrington [13] to a form suitable for coding began. The software, written in a combination of "C"- files and Matlab "M"-files, is provided in the appendix. Calculation of the eigenvalues and eigenvectors (or characteristic modes) begins by

30

creating a wire-grid model of the structure. The length of each wire segment (distance between current nodes) needs to be between $\frac{1}{10}\lambda$ to $\frac{1}{20}\lambda$ [15].

Having decided on the segmentation scheme, a wire-grid description of the object's geometry is entered into EMBPro. This description may be entered either manually or via an automated process that converts a numerical electromagnetics code (NEC) description of the structure into a format readable by ExpertMBPro. The latter option is chosen whenever possible since simple regular geometric shapes can be generated very easily from a few parameters and they should be more simple to analyze than if more complex shapes were used. Additional software was created to generate NEC descriptions of thin metal plates. The wire-grid model is then used to generate $[Z]$ for the structure.

If computations did not suffer from the inaccuracies induced by the finite precision mathematics of the computer, $[Z]$ would be symmetric, i.e. $z_{ij} = z_{ji}$. However, the matrix is slightly asymmetric. Harrington [13] addressed this possibility by suggesting that elements $z_{ij}$ and $z_{ji}$ each be replaced with the element $\frac{z_{ij}+z_{ji}}{2}$, thereby enforcing this symmetry.

Having preprocessed the impedance data to ensure symmetry, the matrix is then ready for input into the program *cmcomp01.c*. This program is a 'C'- code implementation of the algorithm described in [13]. A listing of this program, along with the appropriate header files, can be found in the appendix. The outputs of the program *cmcomp01.c* are the files *b_lambda* and *cmvector*. The file *b_lambda* contains the eigenvalues of interest for the problem. Similarly, the file *cmvector* contains the eigenvectors or characteristic modes.

The algorithms for calculating the eigenvalues and eigenvectors of a structure are summarized in Figures 4 and 5.

31
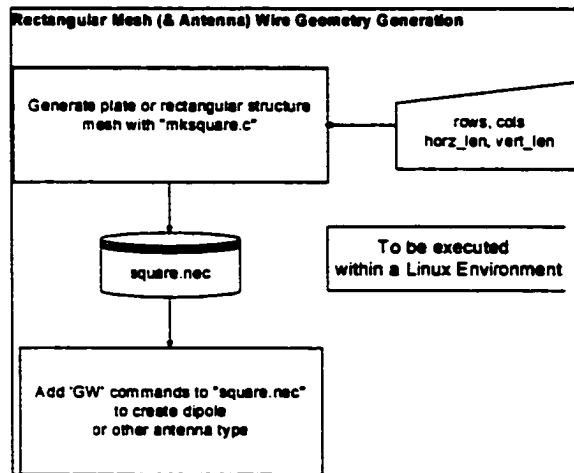
Figure 4:Algorithm used to generate the wire-grid model of a plate.
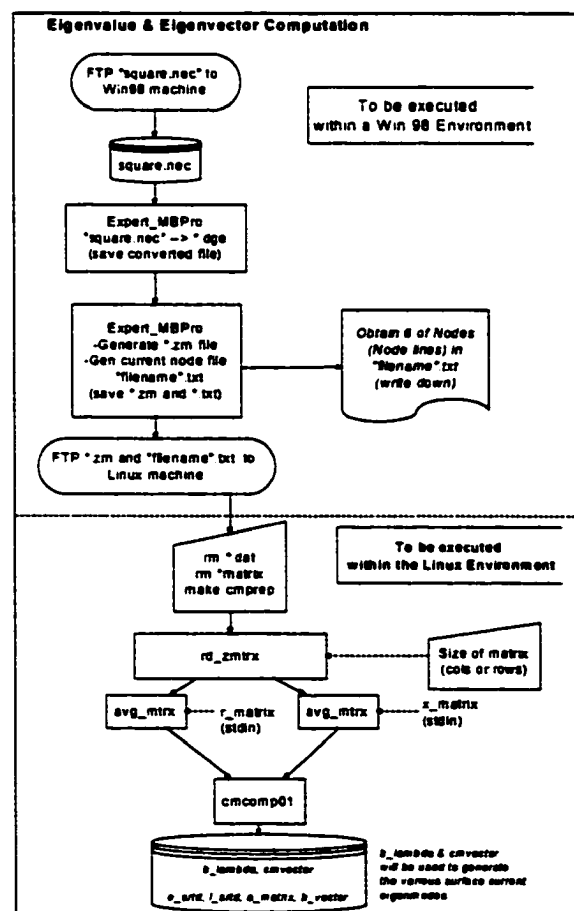


Figure 5:Algorithm for calculation of eigenvalues and eigenvectors (characteristic modes).

32

The position of the eigenvector within the *cmvector* file corresponds to the eigenvalue at the same position within the *b_lambda* file. For example, the third eigenvalue in *b_lambda* corresponds to the third row of values within *cmvector*. This row represents the third eigenvector or characteristic mode.

Therefore, each row within *cmvector* corresponds to a different eigenvector and each element of an eigenvector or characteristic mode corresponds to the value of the characteristic mode at the corresponding current node. This is illustrated by performing a characteristic mode analysis of a half-wavelength dipole antenna. The frequency of interest is 2.450 GHz, which results in an antenna length of 6.096 cm. The wire model was then divided into fifty segments containing forty-nine current nodes. This data was then entered into EMBPro and the impedance matrix $[Z]$ was obtained. Using the algorithm of Figure 5, the characteristic mode data was obtained. The first three eigenvectors of the dipole are shown in Figure 6. This plot represents the normalized surface current on half of the dipole; the dipole current distribution is symmetric.
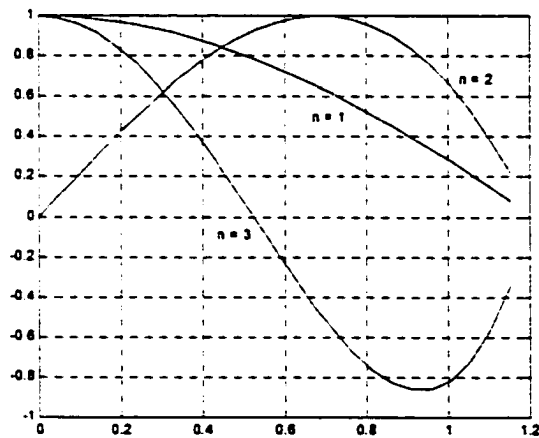


Figure 6:The first three dominant characteristic modes of the dipole, n = 1, 2, 3. Total dipole length was 2.4 inches.

## 3.2.2 Validation

Our software's ability to accurately calculate simple characteristic modes is partially determined by comparing the results of Figure 6 with the data from Thiele [16] as shown in Figure 7.
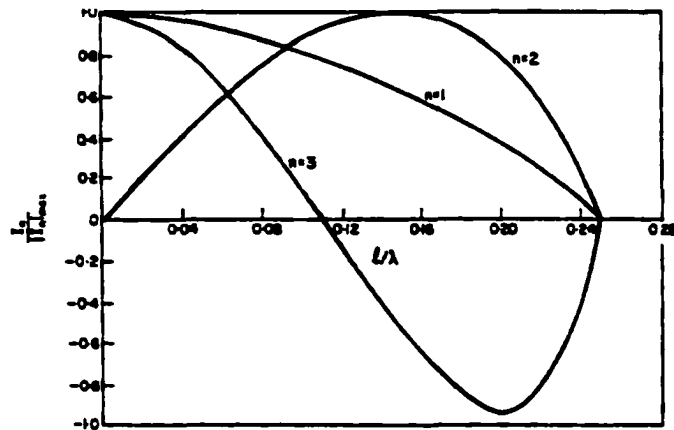


Figure 7:First three characteristic modes normalized to their respective maximums and covering one-half the antenna, 0 to 0.25 lambda [16].

The simplified wire-grid model of an aircraft, as described by Newman [5], was used as another check for proper software operation. This model consisted of two crossed wires with an electrically-small loop "probe" placed at an arbitrary location as shown in Figure 8. Because of the electrical size of the loop, its presence is not included in the calculation of the wire model's characteristic modes.

34
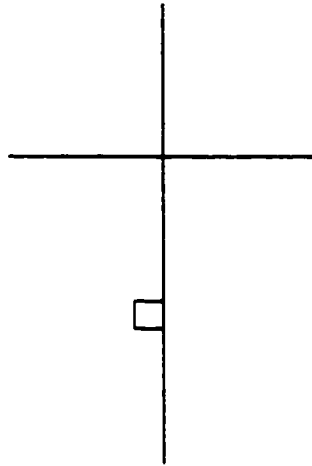
Figure 8:Crossed wires and loop representing the structure of an airplane fuselage and wings with a small loop antenna.

Figure 9, reproduced from Newman [5], shows a plot of the first four characteristic modes of the aircraft model.
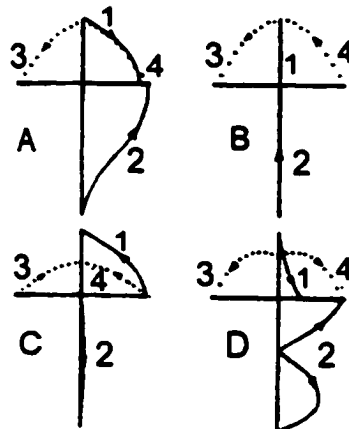
Figure 9:Figures A, B, C, and D represent the first four dominant modes, respectively, of Newman's crossed wires [5]. The solid portion represents the portion of the mode on the vertical segment, while the dotted line represents that portion on the horizontal segment. The direction of the arrow represents "in-phase" or "out-of-phase".

35

The horizontal wire is one wavelength long and the vertical wire is 1.5 wavelength long. The crossed-wire structure was then modeled using EMBPro. The horizontal wire was divided into sixteen segments and the vertical wire was divided into 24 segments. Based on this segmentation, an impedance matrix, $Z$, for the structure was obtained. The dominant eigenvalues and the characteristic modes were then calculated and the first four modes are displayed in Figure 10. Note, in Figure 10, data points one through twenty-three represent that portion of the characteristic mode that lies on the vertical portion of the model. Similarly, points twenty-four through thirty-nine represent that portion of the mode that lies on the horizontal segment of the model.
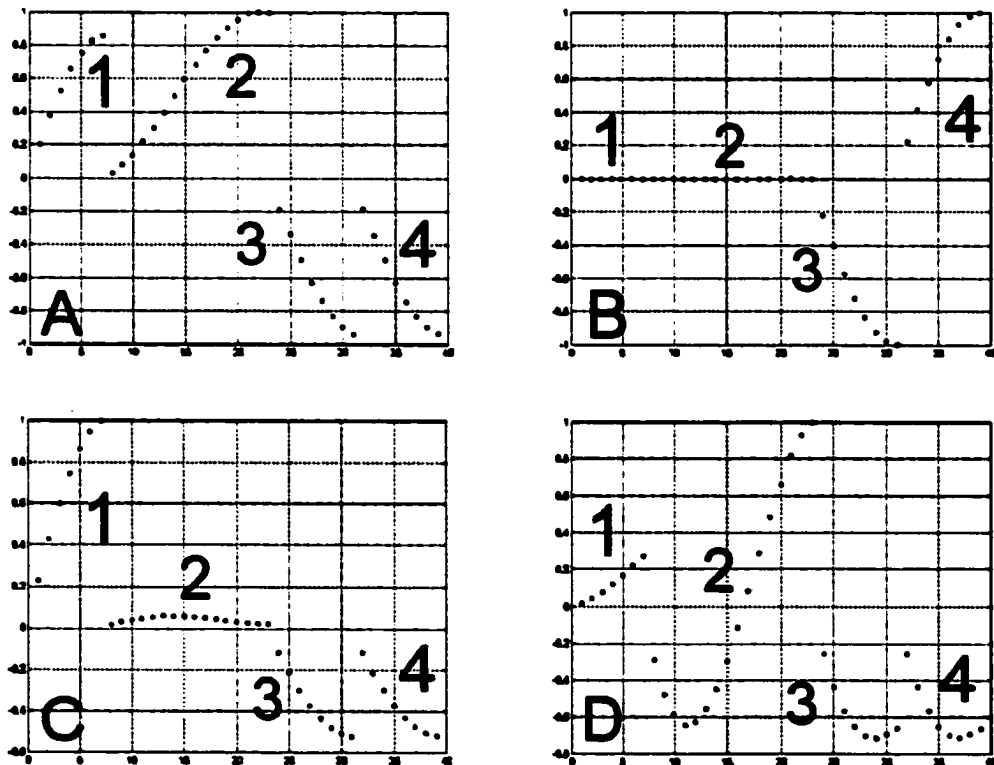


Figure 10:The first four modes of the Newman's model as predicted by our characteristic mode software. Plots A, B, C and D correspond to the same plots in Figure 9. Portions 1 thru 4 on each plot correspond to the similarly labelled areas in Figure 9.

36

Careful inspection of the four plots of Figure 10 reveals close agreement with the characteristic mode shapes of Figure 9. Comparison of Figures 9 and 10 also illustrates the importance of properly numbering the points to facilitate visualization and interpretation of the characteristic modes associated with an object.

### 3.2.3    Mode Visualization

The visualization of modes on the surface of an object is a fundamental tool used in this research. The visualization process applies the spatial processing capability of the human visual system to increase our understanding and internalizing of the relationships between antenna position and the shapes of the characteristic modes for dynamic geometries.

Comparison of Figures 9 and 10 highlights the importance for correctly calculating the modes and displaying them in a spatially accurate manner. Additionally, this comparison identifies two major shortcomings related to the data of Figure 10. First, the characteristic modes are positioned only along the horizontal axis and second, the sequence of the shapes are not consistent with how they appear spatially on either the horizontal or vertical segments. For example, in Figure 10 nodes twenty-four through thirty-nine should be displayed in the following sequence: twenty-four through thirty-one followed by a numerically descending sequence of nodes thirty-nine through thirty-two. Following this re-sequencing, the horizontal portion of the characteristic modes in Figure 10 would more accurately reflect the shapes seen in Figure 9. A similar re-sequencing could be done for those nodes of Figure 10 that represent the vertical portion of the characteristic modes on the aircraft model.

The shortcomings identified during the validation of the Newman work are resolved in two ways. First, the conversion process for converting the geometry of the object into an accurate wire-grid

37

model is modified. This must be done in a way that complements the approach that EMBPro uses to parse the wire grid model and calculate the resultant impedance matrix. The second step focuses on creating an approach that displays the characteristic mode data in a spatially correct manner.

The creation of a wire-grid representation begins by generating an NEC file that approximates a perfect electrically conducting (PEC) structure with a wire-grid. While the surface of wireless devices are a mixture of PEC and dielectric material, approximating the structure as a PEC is a reasonable first-order approximation method for determining the characteristic modes of the actual object. The wire-gridding and accompanying file generation are done rather easily for simple geometries, such as squares and rectangles, by using a computer program that requires only a few input parameters. The NEC file is then parsed by EMBPro to generate a native description of the problem. The NEC file describes the geometry in a very regular fashion. This organization guarantees that the position of elements within $[Z]$, generated by EMBPro, have a well understood and regular relationship with current-node locations on the wire-grid. As a result of this well-defined relationship between $[Z]$ and current-node locations, the characteristic mode file, *cmvector*, maintains this spatial relationship. Figure 11 illustrates the numbering system used for rectangular meshes.

38
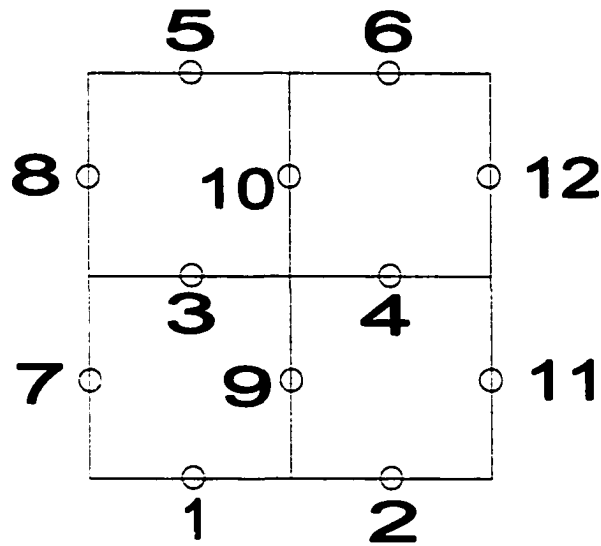
Figure 11:This is an example of the current node numbering system.

The circles along the wires represent the horizontal and vertical (with respect to the plane of the mesh) current node locations. The nodes are numbered in an orderly fashion: first, all the nodes that have horizontally-oriented current, then all the nodes with vertically-oriented current. This numbering process enables the currents across the mesh to be easily separated into horizontal and vertical currents. Note that the current is calculated between the wire intersections.

Another product of EMBPro, *current.txt*, describes the location of each of the current nodes of the wire-grid model. Since this location information was created from the NEC description, the location information has a certain structure to it. This structure enables the orientation of current at each node to be determined. By combining this location and orientation information with the *cmvector* information, there is sufficient information to accurately display characteristic mode data across the surface of the one or two-dimensional object.

Having created a process for describing an object's geometry in a very regular manner, we shall

39

now address how to display the associated characteristic mode information. We begin by examining the structure of the file, *cmvector*. The characteristic mode file contains arrays of numbers that represent the magnitude of a characteristic mode at a particular current node. The arrays are formatted such that all horizontal current information is stored in the first half of each array, while the vertical current information is stored in the second half of the array. To simplify the display of the characteristic mode current distribution, only one orientation of characteristic mode currents, horizontal or vertical, will be displayed at a time. For a particular orientation, this requires node current magnitude to be displayed at a location in two dimensions. Therefore, a combination of false color rendition and orthogonal projections of the mode data will be used to display the mode data.

By using such an approach we were able to extract and view separate surfaces that represent the magnitude of either horizontally or vertically-oriented characteristic modes at each node on the surface of the object. This approach to modeling the structure and the currents on the structure in a predetermined manner proves very useful as the structures become more complex.

### 3.2.4 Far-Field Radiation Computation

Once the characteristic modes have been calculated for an object, they can then be used to calculate the radiation pattern of the system. The algorithm designed to calculate the far-field radiation from the antenna system is based on calculation of the radiation generated from a collection of short dipoles in space. This approach is based on the equation

$$\mathbf{E} = -j\omega \mathbf{A} - j\frac{\nabla(\nabla \bullet \mathbf{A})}{\omega\mu\varepsilon}, \tag{62}$$

where $A$ is the *magnetic vector potential*. For a $\hat{z}$-directed current element, the magnetic vector potential is defined as

$$\mathbf{A} = \hat{z}\mu I \int_{-\Delta z/2}^{\Delta z/2} \frac{e^{-j\beta R}}{4\pi R}d\hat{z}. \tag{63}$$

40

This equation can be reduced to

$$\mathbf{A} = \mu I \frac{e^{-j\beta r}}{4\pi r} \Delta z \hat{z}, \tag{64}$$

where $\Delta z \ll \lambda$, and therefore $R \approx r$. For the purposes of this research, all the current elements are either $\hat{x}$-directed or $\hat{y}$-directed. Expressing $A_{\hat{x}}$ and $A_{\hat{y}}$ in spherical coordinates results in

$$A_{\hat{x}} = A_{\hat{r}} \sin\theta\cos\phi + A_{\hat{\theta}} \cos\theta\cos\phi - A_{\hat{\phi}} \sin\phi, \tag{65}$$

and

$$A_{\hat{y}} = A_{\hat{r}} \sin\theta\sin\phi + A_{\hat{\theta}} \cos\theta\sin\phi + A_{\hat{\phi}} \cos\phi. \tag{66}$$

Applying these conversions to equations (62) and (64) yields the following expressions for the electric-fields, ($\mathbf{E}$), generated from these current segments. The first two equations represent those $\hat{\theta}$- and $\hat{\phi}$-directed electric-fields that are generated from an $x$-directed current element. Similarly, the second two equations are for a $y$-directed element.

$$E_{\hat{\theta}x} = \hat{\theta}\frac{-j\omega\mu e^{-j\beta r} I_x \Delta x}{4\pi r} \cos\theta\cos\phi \tag{67}$$

$$E_{\hat{\phi}x} = \hat{\phi}\frac{j\omega\mu e^{-j\beta r} I_x \Delta x}{4\pi r} \sin\phi \tag{68}$$

$$E_{\hat{\theta}y} = \hat{\theta}\frac{-j\omega\mu e^{-j\beta r} I_y \Delta y}{4\pi r} \cos\theta\sin\phi \tag{69}$$

$$E_{\hat{\phi}y} = \hat{\phi}\frac{-j\omega\mu e^{-j\beta r} I_y \Delta y}{4\pi r} \cos\phi \tag{70}$$

The expression for $E$ in the above expressions is normalized based on a constant distance from the antenna system center. All $\Delta x_{mesh}$ and $\Delta y_{mesh}$ (the length of the $x$-oriented and $y$-oriented segments, respectively, that form the meshed model of the structure) are the same and $\Delta x_{ant} = K\Delta x_{mesh}$, where $K$ is the ratio between the length of an element on the mesh and that of the

41

antenna. Therefore, $E_{\hat{\theta}x}$, $E_{\hat{\phi}x}$, $E_{\hat{\phi}y}$, and $E_{\hat{\theta}y}$ are all just functions of $\theta$ and $\phi$. This approach computes the fields generated from single elements and works for single $x$-directed and $y$-directed elements. This approach must be expanded to encompass the more complex geometries associated with wire grids and linear antennas. The wire-grid approximation of a plate with a linear antenna above it can be modeled by a two-dimensional array of $x$ and $y$-directed elements (the plate) with a linear array of $x$-directed elements (the antenna) placed above the two-dimensional array. To address this situation, an approach based on that of Stutzman *et al.* [8] is used. The authors compute the field generated by an array of current elements as the following:

$$AF(\theta, \phi) = \sum_{n=1}^{N} \sum_{m=1}^{M} I_{mn} e^{j(\beta \hat{r} \bullet \vec{r}_{mn})} \tag{71}$$

where $\vec{r}_{mn} = \dot{x}_{mn}\hat{x} + \dot{y}_{mn}\hat{y} + \dot{z}_{mn}\hat{z}$ represents the vector, in rectangular coordinates, to each current element in the $M \times N$ array. Additionally, $\hat{r} = \hat{x}\sin\theta\cos\phi + \hat{y}\sin\theta\sin\phi + \hat{z}\cos\theta$ represents a spherical coordinate description of the vector pointed at angle $(\theta, \phi)$. Equation (71) computes the complex phase contributed by an element at $(x, y, z)$ to the overall pattern of the array at the angle $(\theta, \phi)$. However, the orientation of each element must also be included into the above expression to calculate the total $E_{\hat{\theta}x}$, $E_{\hat{\phi}x}$, $E_{\hat{\phi}y}$, and $E_{\hat{\theta}y}$ at some angle $(\theta, \phi)$ in the far-field. This expression is calculated by combining the individual patterns of the small $x$- and $y$-directed current elements in the wire mesh and the antenna. Due to the way that the wire mesh is modeled, the current is calculated at the middle of each of the small current elements. Additionally, to generate a smoother, more realistic approximation of the current distribution on the surfaces of both the antenna and the plate, the current distribution across each small current element will be modeled using a sinusoidal approximation. In this approach the current starts at zero at each end of the small current (dipole) element and then increases symmetrically from both ends to the maximum value at the center of the element. This maximum value is the calculated value of current for this element. The following

42

equations represent the electric field (normalized in the far-field) produced by $x$- and $y$-directed current elements respectively.

$$E_{\bar{x}}(\theta,\phi) = I_x \left( \begin{array}{c} \int_{-\frac{L}{2}}^{0} e^{jx\beta\sin\theta\cos\phi}\sin\left(\frac{\beta L}{2} + \beta x\right)dx + \\ \int_{0}^{\frac{L}{2}} e^{jx\beta\sin\theta\cos\phi}\sin\left(\frac{\beta L}{2} - \beta x\right)dx \end{array} \right) \tag{72}$$

$$E_{\bar{y}}(\theta,\phi) = I_y \left( \begin{array}{c} \int_{-\frac{L}{2}}^{0} e^{jy\beta\sin\theta\sin\phi}\sin\left(\frac{\beta L}{2} + \beta y\right)dy + \\ \int_{0}^{\frac{L}{2}} e^{jy\beta\sin\theta\sin\phi}\sin\left(\frac{\beta L}{2} - \beta y\right)dy \end{array} \right) \tag{73}$$

The $\sin\left(\frac{\beta L}{2}...\right)$ term in each expression represents the sinusoidal variation of the current magnitude upon the small dipole. The $e^{jx\beta\sin\theta\cos\phi}$ term represents the spatial phase contribution to the $E_{\bar{x}}$ at $(\theta,\phi)$ from each point along an $x$-oriented small dipole. Similarly, the $e^{jy\beta\sin\theta\sin\phi}$ terms represent the spatial phase contribution to $E_{\bar{y}}$ at $(\theta,\phi)$ from each point along the $y$-oriented small dipole. These exponents are one-dimensional examples of the same approach used in (71). Thus, the above fields represent the normalized $E$-field patterns of each of the small dipoles that form the wire-grid mesh. Equations (72) and (73) can be reduced to the following equations respectively.

$$E_{\bar{x}}(\theta,\phi) = \left\{ I_x \left(\frac{2}{\beta - \beta(\sin^2\theta\cos^2\phi)}\right)\left[\cos\left(\frac{\beta L}{2}\sin\theta\cos\phi\right) - \cos\left(\frac{\beta L}{2}\right)\right] \right. \qquad |\sin\theta\cos\phi| \neq 1 \right\}$$
$$E_{\bar{x}}(\theta,\phi) = \left\{ I_x \left(\frac{L\sin\left(\frac{\beta L}{2}\right)}{4}\right) \qquad |\sin\theta\cos\phi| = 1 \right\} \tag{74}$$

$$E_{\bar{y}}(\theta,\phi) = \left\{ I_y \left(\frac{2}{\beta - \beta(\sin^2\theta\sin^2\phi)}\right)\left[\cos\left(\frac{\beta L}{2}\sin\theta\sin\phi\right) - \cos\left(\frac{\beta L}{2}\right)\right] \qquad |\sin\theta\cos\phi| \neq 1 \right\}$$
$$E_{\bar{y}}(\theta,\phi) = \left\{ I_y \left(\frac{L\sin\left(\frac{\beta L}{2}\right)}{4}\right) \qquad |\sin\theta\cos\phi| = 1 \right\} \tag{75}$$

The expressions for the electric field for the cases when $|\sin\theta\cos\phi| = 1$ and $|\sin\theta\sin\phi| = 1$ are calculated using L'Hopital's rule.

The total field pattern generated from an array of similar antennas is the sum of products of the element and array patterns. This is expressed by equations (76),(77),(78), and (79). These equations

43

combine the results from equations (67), (68), (69), (70), (71), (74), and (75) as shown below:

$$E_{\hat{\theta}x}(\theta,\phi) = \hat{\theta}\cos\theta\cos\phi\sum_{n=1}^{N}\sum_{m=1}^{M}E_{\bar{x}}(\theta,\phi)\,\Delta x e^{j(\beta\bar{r}\cdot\bar{r}_{mn})} \tag{76}$$

$$E_{\hat{\phi}x}(\theta,\phi) = -\hat{\phi}\sin\phi\sum_{n=1}^{N}\sum_{m=1}^{M}E_{\bar{x}}(\theta,\phi)\,\Delta x e^{j(\beta\bar{r}\cdot\bar{r}_{mn})} \tag{77}$$

$$E_{\hat{\theta}y}(\theta,\phi) = \hat{\theta}\cos\theta\sin\phi\sum_{n=1}^{N}\sum_{m=1}^{M}E_{\bar{y}}(\theta,\phi)\,\Delta y e^{j(\beta\bar{r}\cdot\bar{r}_{mn})} \tag{78}$$

$$E_{\hat{\phi}y}(\theta,\phi) = \hat{\phi}\cos\phi\sum_{n=1}^{N}\sum_{m=1}^{M}E_{\bar{y}}(\theta,\phi)\,\Delta y e^{j(\beta\bar{r}\cdot\bar{r}_{mn})} \tag{79}$$

Note that these equations are normalized patterns for the far-field. These expressions are then used in conjunction with the characteristic mode currents to calculate the far-field radiation for the system when it is probed or fed at a particular location on the object. The algorithm in Figure 12 formalizes this process.

44

File "probeloc" format
# of sources <cr>
Source E-field<space>Node#<cr>

cmvector
b_lambda

Expert MBPro
Open desired *.dge file
-Diagnostics
-List of Current Nodes
-Save as "current"

STDIN:
"Number of nodes"
"Total eigenmodes"
"Number of dominant modes"
(Enter the value of each dom. mode)

cmvecdec

current.txt
(record # of current nodes)

current.txt ---> current.nod

cmvector.new ---> cmvector

current.nod

b_lambda.new ---> b_lambda

seg_dir

STDIN:
"number of nodes"

probeloc

seg_dir.dat

STDIN:
"number of nodes"
"number of dominant modes"
(# of modes in b_lambda)

totalcur

J_total

tc

STDIN:
"number of nodes"

current.dat

tc.dat
current.dat

nodesift

current.dat (revised)

efield02

STDIN:
- # of radiating elements (# of rows in current.dat (rvsd))
- # of theta divs
- # of degs / theta div
- # of phi divs
- # of degs / phi div
- Total # of antenna segments
- Antenna to wire mesh segment ratio
- Distance between current nodes (in wire mesh)
- Lambda (in inches)
- # of 'x' rows
- # of 'y' rows

Figure 12:Algorithm for the calculation of the radiation pattern.

The ability of this algorithm to calculate the far-field radiation of an antenna system is demonstrated by attempting to reproduce a set of results from Murray [14]. For this example, the far-field

45

pattern in the E-plane will be predicted for the reflector antenna shown in Figure 13
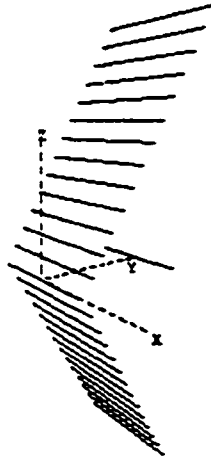


Figure 13:The wire-frame model of a reflector antenna described by Murray [13].

Figure 14 illustrates the E-plane pattern obtained for the previously illustrated reflector antenna. These results were obtained using the far-field algorithm of Figure 12. Note that the plot in this figure represents a summation of the contributions from all of the characteristic modes for the model of the reflector antenna.

46
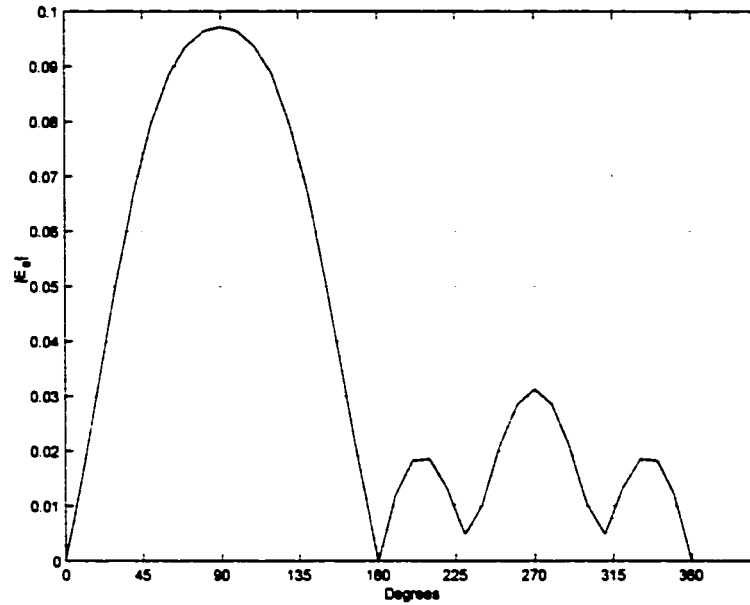
Figure 14:Far-field pattern obtained using a characteristic mode approach.

Figure 15 is a copy of the results from Murray [14] for the E-plane radiation for the same reflector antenna. A qualitative comparison of the two plots (compare with Murray's *triangle* data points) indicates a great deal of similarity between the two shapes.

47
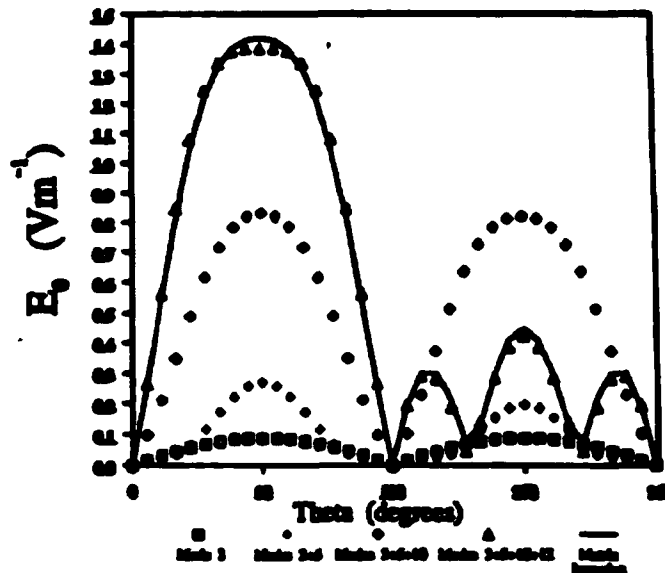
Figure 15:Reflector antenna E-plane pattern.

## 3.3   Experimental Work

The experimental portion of this research is divided into three major sections: measurement system construction, antenna system design and construction, and data measurement.

### 3.3.1   Measurement System Construction

The measurement system is based on two portable anechoic cube that belong to the UNH ECE department. Five sides of each cube are solid, measuring four feet on a side. The final side of the cube remains open and is positioned so that this side faces the open side of the other cube. The structural portions of the cubes are constructed with "Cellotex". This is a relatively sturdy, lightweight, thermal insulation material that has a thin aluminum sheet adhered to each side of the bare insulation. RF anechoic foam was glued to one side of each piece of Cellotex that formed a side of the cube. This arrangement of foam and aluminum provides significant attenuation to signals

48

striking the interior faces of the cube. Additionally, the external aluminium sheeting significantly blocks RF noise that would otherwise be incident upon the reference and test antennas.

Several large velcro patches are attached along the edges of the cube. This allows the cube to be taken apart and moved (through a standard door) to a new location where the cubes can be reassembled to form a portable far-field anechoic chamber for antenna pattern measurements. This arrangement allows for the placement of additional foam within each cube and between them to further reduce multipath interference.

To facilitate the measurement of antenna radiation patterns, an antenna positioning and measurement system was constructed. The positioner and angular-measurement system were designed to be rotated by hand and provide a high degree of accuracy and repeatability for pattern measurement. The positioner system is constructed from non-conductive PVC pipe and fittings. This is done to limit the interaction between the antenna positioning system and the antenna system itself.

The positioning system consists of a PVC pipe that rests on a PVC "bearing" to allow rotation of the positioner. The pipe then passes through the bottom of the anechoic chamber that contains the test antenna (system). Above the floor of the chamber, the pipe is bent in a modified "C" shape. This orientation allows the antenna under test to be rotated about a point in space while imparting very little phase distortion from the positioning system itself. Cable is passed up the center of the positioning pipe and stops at the top end of the "C" structure. The end of the positioner is shaped to accommodate the antenna system mounting piece. This piece attaches the antenna system to the positioning system so that the antenna system center lies on the axis of rotation for the positioning system.

The network analyzer is placed in the *trigger-on-point* mode to obtain measurements. *Trigger-on-point* works by recording a power level on the screen when a TTL level pulse is injected into the

49

analyzer. The angular measurement system is designed to produce a trigger input to the network analyzer for every 1.8 degrees of rotation of the positioning support. If done correctly, the network analyzer can record a rectangular antenna plot for a full 360 degree rotation. For the purposes of this study, the network analyzer was set for 201 points. This means that 201 data points will equal the distance across the screen. Dividing these points into the degrees in a circle results in the 1.8 factor listed above. To achieve this triggering, a circular clear plastic sheet with 201 small black bars around its periphery is attached to the shaft of the positioning pipe. An infrared LED and detector are used to generated the pulse to the network analyzer as the beam is interrupted by the passing of each of the small black bars as the system is rotated. By beginning each rotation of the antenna at the same black bar on the plastic sheet, a high degree of accuracy (in terms of pattern measurement) is obtained.



Figure 16:The plate and antenna attached to the antenna positioning system within the antenna system under test (ASUT) cube at UNH.

50

## 3.3.2 Antenna Mount

Testing required that a center-fed half-wavelength dipole antenna be positioned at arbitrary locations above a square plate. This system should allow easy repositioning of the antenna and enable repeatable trials. Additionally, the antenna needed to be fed with a balanced feedline to avoid radiation from the feedline itself. During the test, the antenna was to be relocated over several positions during the tests or antenna measurements.

Initial work was directed at fabricating a balun to convert the feed from the cable connected to the analyzer to a balanced antenna feed. The "bazooka balun", Figure 17, design [17] and [18] was chosen to address these requirements.



Figure 17:The balun with the dipole attached.

After fabricating the balun, the next step was to build a mounting structure that supported the antenna at the proper height above the conducting plate and at the proper location. This mount also needed to be sturdy enough to connect the plate / antenna combination to the antenna positioning

51

device. Both of these requirements were met using the design shown in Figures 16 and 18.



Figure 18:Antenna / balun mount on the back of the plate.

Properly securing the balun/antenna combination in the *Balun Compression Structure* and adjusting this structure's position within the *Antenna Plate Mounting Collar*, enabled the antenna to be positioned at the correct height and orientation with respect to the plate. An *Antenna Plate Mounting Collar* was mounted at each of the potential antenna test positions. Once the antenna was moved to one of these locations, copper tape was applied across the hole through which the feed-line passed. This approximated a continuous perfect electric conductor (PEC) beneath the antenna. To move the antenna, the tape is removed, the antenna released from the compression structure and mounting collar, the antenna is re-mounted at a new location and the previous hole is covered with a small section of copper tape. This approach requires only one antenna and plate to calculate the far-field response of many antenna/plate combinations.

### 3.3.3 Pattern Measurement

Pattern measurement begins by placing the cubes sufficiently far apart so that the reference and

52

test antennas are spaced in the *far-field* of each other. The antenna system under test (ASUT) is mounted on the antenna positioning structure, while in the other cube a horn antenna is statically mounted. Both the ASUT and the horn are positioned so that, by rotating the ASUT, a measurement with the correct polarization and field orientation relative to the two antennas is obtained. The following figure represents a schematic of this arrangement.



Figure 19:Test chamber schematic.

The diagram on the right-hand side of Figure 19 represents the horn antenna positioned so that its boresight is pointing toward the ASUT in the left-hand portion of the figure. The left ASUT is represented by the heavy black vertical line on the end of the antenna positioner shown here as the thin horizontal rectangle. The curving, dashed line indicates the ASUT's rotation path. Additionally, RF anechoic foam is placed on the ceiling and the wall of the laboratory to further reduce multipath interference.

A network analyzer is attached between the ASUT and the horn antenna. The ASUT is rotated and the patterns are recorded by the network analyzer. Once the data is collected, it is sent via the network analyzer's GPIB port to a data logging program on a nearby computer and stored for future analysis.

53

# Chapter 4
# RESULTS

Having described the background and discussed the methods for calculating characteristic modes we shall now discuss the results obtained from this research. Both computational and experimental methods were used to obtain data. This dual approach enabled the further development of tools and techniques for characteristic mode analysis and provided an opportunity for validation and comparison of the data generated from these tools with the measured system patterns. The computational approach was used in both the one and two-dimensional systems, while the experimental investigation was limited to a two-dimensional system.

To facilitate the calculation of the characteristic modes of simple structures (dipoles, wires, and plates) and systems composed of these structures, special software presented in the previous chapter was developed. In order to interoperate with the commercial software that was used to determine the impedance matrix and the current node placement descriptions, a strictly formatted description of the geometry was required and this was achieved by using NEC files that described the system geometry. These files that described the antennas, wires, and plates were generated automatically with only the input of a few descriptive parameters by using the associated, specialized algorithm developed in the course of the software development.

## 4.1 One-Dimensional System

### 4.1.1 Isolated One-Dimensional Structures

A half-wavelength, center-fed dipole and a 1.5 wavelength section of wire were the first structures modeled. These sizes were chosen to ensure that both objects were of near-resonant size.

54

Characteristic mode analysis was performed at a frequency of 2.45GHz. This translates to an antenna and wire with lengths 6.096 cm and 18.288 cm, respectively. The antenna and the wire were initially modeled independently. This data provided baseline information for later comparison to the characteristic mode data generated when the antenna and the wire were in close proximity to each other.

An upper limit on the size of each segment in the wire-frame model was $\frac{1}{10}\lambda - \frac{1}{20}\lambda$. This limit was chosen based on historical work as described in the chapter 2. While the lower limit of segment size offered more leeway, a segment size of $0.042\lambda$ was chosen. This divided the antenna into twelve wire segments with eleven current nodes and the wire into thirty-six segments with thirty-five current nodes. Current nodes only exist between wire segments. This segment size proved to be a reasonable choice in terms of the number of segments required to provide an accurate portrayal of current distribution while reducing the number of required segments. The wire-frame model of the dipole and the wire used a wire radius of $0.000208\lambda$. This ensured that the wire radius was very small compared to a wavelength. This relationship, wire radius $<< \lambda$, is one requirement to ensure accurate system modeling when using an MoM approach such as the EMBPro software. A characteristic mode analysis was then performed on the model of the antenna and the wire using the steps outlined in Chapter 3.

The first three eigenvalues of the antenna are shown in Table 2. The eigenvalues' order is based on $\left| \frac{1}{1+j\lambda} \right|$ as described by equation 51. The corresponding characteristic modes are shown in Figure 20.

| Eigenvalue Order | Eigenvalue |
|---|---|
| $\lambda_1$ | 0.40 |
| $\lambda_2$ | $-180.76$ |
| $\lambda_3$ | $-12665.37$ |

Table 2:The first three eigenvalues of the dipole antenna.
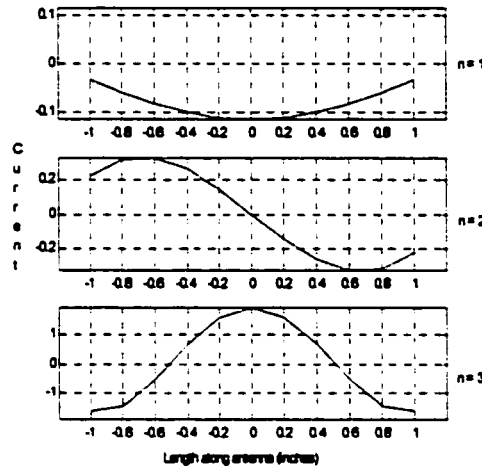


Figure 20:The first three characteristic modes of the isolated half-wavelength dipole.

Notice that the antenna model extends from $-1.2$ to $1.2$ (inches). However, the characteristic mode plots only extend from $-1.0$ to $1.0$ (inches). Recall that the current nodes only exist between contiguous segments. As a result, the ends of the antenna do not have current segments and the current is not calculated at these points. However, it is known from electromagnetic theory that boundary conditions set the axial current to zero at the end of the wires. Therefore, the plots of Figure 20 are accurate approximations for each of the first three characteristic modes on the dipole.

Comparing corresponding values of the eigenvalues and eigenvectors obtained for the dipole model of chapter two and the results here indicates a great deal of similarity, both in the relative magnitudes of the eigenvalues and the general shape of the eigenvectors associated with these

56

eigenvalues. The difference in the general shape of the eigenvectors and the values of the eigenvalues can be attributed to the number of segments used to model the dipole in chapter 2 versus the smaller number of segments used for this model. This similarity further justifies using a segment size of $0.2''$.

The results for the first three eigenvalues of the wire are shown in Table 3. Again, the ordering of the eigenvalues is based on $\left|\frac{1}{1+j\lambda}\right|$. The corresponding characteristic modes are shown in Figure 21.

| Eigenvalue Order | Eigenvalue |
|---|---|
| $\lambda_1$ | 0.224 |
| $\lambda_2$ | -1.075758 |
| $\lambda_3$ | -1.208634 |

Table 3:The first three eigenvalues of the 1.5 wavelength wire.
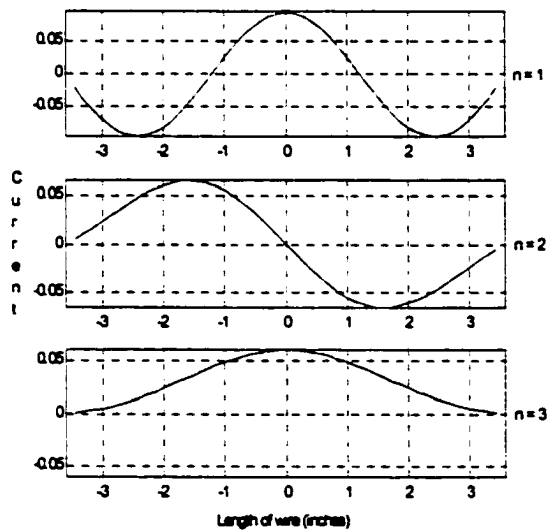


Figure 21:These are the first three characteristic modes of the 1.5 wavelength wire.

It is of interest to note that if the wire were fed at its center, and the approach of section 2.2 were applied, the resultant current distribution would closely approximate the plot of the first mode

57

in Figure 21. This result is very similar to the surface current distribution expected if the typical $\sin(x)$ current approximation were used for the wire antenna.

## 4.1.2 System of One-Dimensional Structures

The isolated antenna and wire structures were then assumed to be close to each other. This created a new antenna system. The system is composed of the half-wavelength center-fed dipole positioned parallel to and $0.021\lambda$ above the $1.5\lambda$ wire. The wire and antenna radii and segment lengths were as previously described. The antenna was moved to five positions and the characteristic modes of the system were computed. At each of these positions, the antenna is the same height above the wire. The final arrangement places the antenna above the wire such that one end of the antenna is even with the end of the wire. The initial and final positions of the antenna above the wire are shown in Figure 22.

Position 1

Position 2

Position 3

Position 4
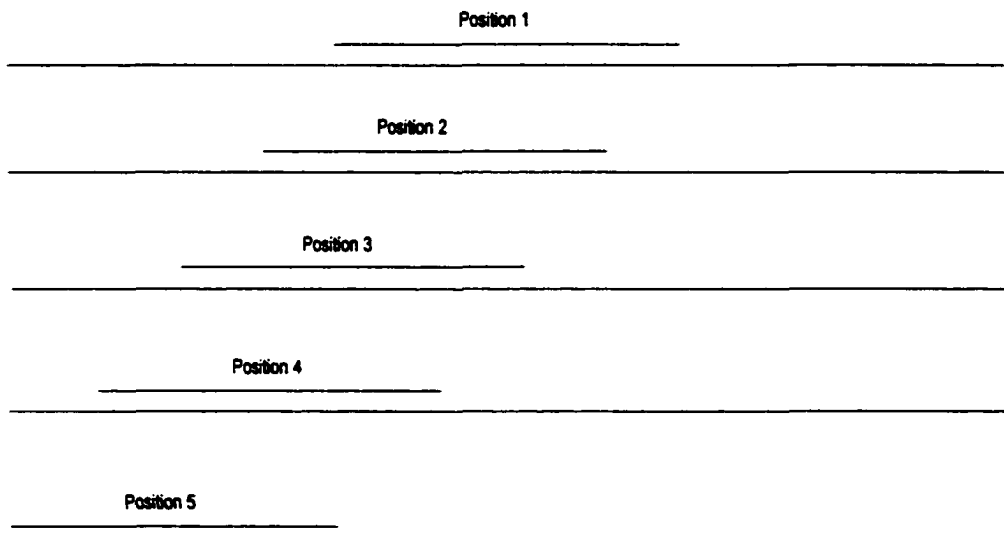
Position 5

Figure 22:The dipole shown at each of the five positions above the wire.

58

Table 4 lists the center and endpoint coordinates of the wire. Table 5 lists the center and endpoint

coordinates for the antenna at each of the five locations. All the coordinates are in inches.

| Left Endpoint | Center | Right Endpoint |
|---|---|---|
| $(-3.6, 0, 0)$ | $(0, 0, 0)$ | $(3.6, 0, 0)$ |

Table 4:Center and endpoints coordinates for the wire.

A simple process was created to generate NEC descriptions of the wire / antenna system. First,

a NEC file description for the wire is created. Then a NEC description of the antenna is appended

to the first NEC file. The resultant NEC file organization simplified the interpretation and post-

processing of EMBPro products that described the current node locations and the impedance matrix.

This same approach will be expanded upon later during the study of two dimensional structures.

It is important to note that these characteristic modes of the system will have a portion of their

values / or shape corresponding to current nodes that lie on the antenna structure and nodes that

lie on the wire structure. These become an important consideration when interpreting the results

obtained or recorded in the characteristic mode file, $cmvector$.

Once the system has been described and modeled, the characteristic modes of the system are

calculated. The most dominant eigenvalue for the system when the antenna is at each of the five

positions above the wire are listed in Table 6. Again, dominance is determined by $\left|\frac{1}{1+j\lambda}\right|$. For

example, of all the eigenvalues calculated for the antenna / wire arrangement of position 1, 0.220886

results in the largest value of $\left|\frac{1}{1+j\lambda}\right|$.

Additionally, Figures 23 - 25 are plots of the current distributions calculated for the wire portion

and antenna portion of the first dominant, second dominant and the third dominant characteristic

modes of the wire and antenna system for the antenna at each of the five different positions.

59

| Left endpoint | Antenna center | Right endpoint |
|---|---|---|
| (−1.2,0,0.1) | (0,0,0.1) | (1.2,0,0.1) |
| (−1.8,0,0.1) | (−0.6,0,0.1) | (0.6,0,0.1) |
| (−2.4,0,0.1) | (−1.2,0,0.1) | (0,0,0.1) |
| (−3.0,0,0.1) | (−1.8,0,0.1) | (−0.6,0,0.1) |
| (−3.6,0,0.1) | (−2.4,0,0.1) | (−1.2,0,0.1) |

Table 5:Center and endpoints coordinates for the antenna at each of the five positions.
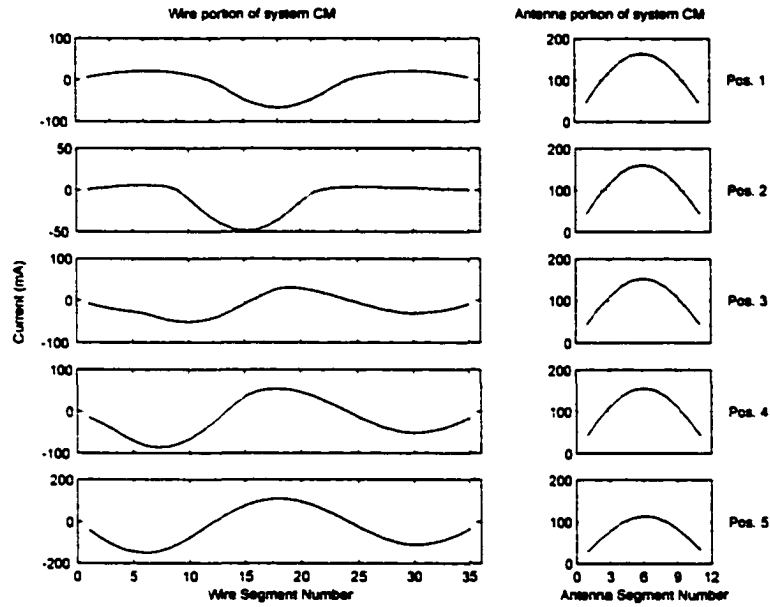


Figure 23:Current distributions for the wire and antenna portions of the dominant system mode for the antenna at positions 1 - 5.

60

| Position | Eigenvalue |
|----------|-----------|
| 1 | 0.220886 |
| 2 | 0.223543 |
| 3 | 0.185340 |
| 4 | 0.162690 |
| 5 | 0.157992 |

Table 6:The most dominant system eigenvalues at each of the five positions.
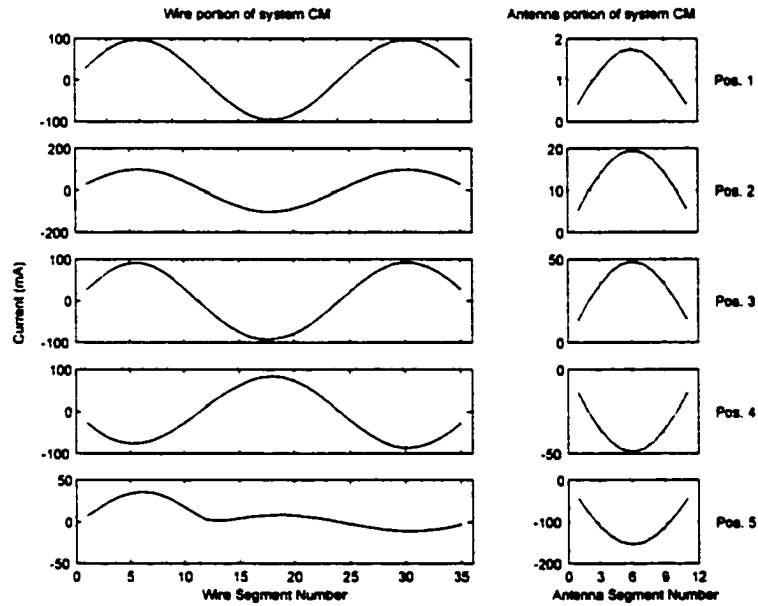


Figure 24:Current distributions for the wire and antenna portions of the second dominant system mode for the antenna at positions 1 - 5.

61
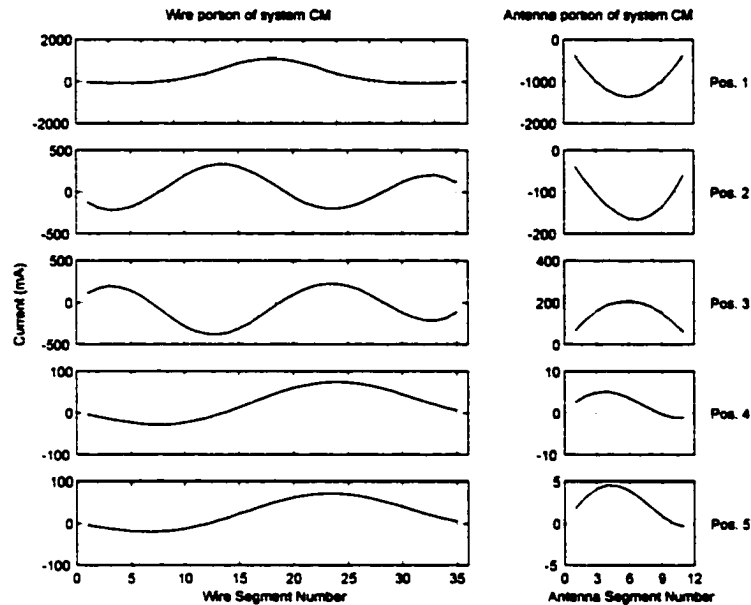
Figure 25:Current distributions for the wire and antenna portions of the third dominant system mode for the antenna at positions 1 - 5.

### 4.1.3 Characteristic Mode Interpretation for One-Dimensional Systems

As the antenna is positioned in each of the five positions the characteristic modes of the system change accordingly. However, closer inspection of these modes reveals a number of recurring trends in the shape of these modes. Examination of the plots begins by separating the system characteristic mode response into a portion that is associated with the wire and a portion that is associated with the antenna.

Examination of the wire portion of the system mode responses seen in Figures 23 - 25 suggest that it too can be divided into two parts: the general and local effect. The general effect is that portion of the wire response that is expressed over the entire length of the wire. The shape of the general effect closely resembles one of the characteristic modes of the isolated wire. Conversely,

62

the local effect is limited to the region on the wire directly below the antenna. In many of the plots of the wire portion in Figures 23 - 25, the local effect resembles the negative image of the antenna portion of the system characteristic mode, which, in many of these plots, resembles one of the characteristic modes of the isolated antenna.

The data in Figures 23 - 25 suggests that, for certain antenna positions, the local effect dominates the combination of the local and general effects. At other positions, the local effect does not seem to be present, only the general effect is seen. However, at still other positions, the overall response on the wire resembles a combination of the general and local responses. These results suggest that the wire portion response may be approximated by a weighted sum of the general and local responses. The relative weighting of such a approximation appears to be related to the antenna position with respect to certain qualities of the system, i.e. the antenna distance from the center of the wire or the distance of the antenna from the edge of the wire.

Examination of the antenna portion of the first two dominant system modes indicates that, for all positions in Figures 23 and 24, the shape is very similar to a weighted version of the dominant characteristic mode of the isolated dipole. However, this trend changes in Figure 25. Here the shape of the antenna portion becomes increasingly asymmetric as the antenna approaches the edge of the wire. Extending the discussion of the wire portion of the system modes to the antenna portion of the system response suggests the following. For the less dominant system modes, the shape of the antenna portion may be approximated by a function relating the shape of a mode from the isolated antenna to the antenna's position with respect to some feature of the wire, such as the distance of the antenna from the center of the wire.

Such relationships or correlations hold promise for determining functional relationships between antenna position and how the antenna portion and the wire portions of the system characteristic

63

mode may be approximated using sums of distorted versions of the characteristic modes of the isolated antenna and the isolated wire.

## 4.2 Two-Dimensional Structures and Systems

### 4.2.1 Transition from 1-D to 2-D structures

This portion of the research focused on the application of characteristic mode analysis to a system composed of an antenna positioned a fraction of a wavelength above a square plate. A plate structure was chosen to be studied because it represents the simplest two-dimensional geometry. The height above the plate was chosen to model the effect of an antenna that was located very close (in terms of a wavelength) to the structure, in this case the plate. This models the effect of an embedded antenna similarly positioned on a near-resonant size wireless device. By increasing the complexity of the structure under study (from one to two dimensions), we hope to improve our understanding of the relationship between the antenna position and its interaction with the structure, as exhibited by differences between the characteristic modes of the isolated plate and the isolated antenna and the characteristic modes of the system.

In transitioning from one-dimensional to two-dimensional structures, a number of issues were encountered that required resolution. Some of the issues were extensions of work already addressed in the one-dimensional case. However, certain issues were unique to structures in two-dimensions. These issues identified some of the subtleties specific to this approach and to characteristic mode analysis in general.

One of the first issues to be resolved was whether to use a wire-grid model of the plate or simply a collection of parallel wires. Initially, a fully-meshed wire grid approach was to be used for modeling the wire plate. However, initial attempts to model the plate using a gridding scheme,

64

similar to that of Figure 11, resulted in the generation of asymmetric $[Z]$ matrices. Different models using a given number of wires with a particular radius and segment length were tried. However, none of these models produced a symmetric $[Z]$.

The asymmetry of the impedance matrix was thought to have been the result of exceeding the EMBPro software's geometry limitations, while, at the same time, keeping the number of wires needed to model the plate small enough to make the calculation of the problem tractable for the available computer resources. The geometry limitations were based on the following suggestions: wire segment length to wire radius ratio $> 8$, wires should be thin, so that only the axial currents are significant, and wires, that are not connected, should not be close to each other [19]. As the model began to approach these limitations, EMBPro's solution could no longer generate a symmetric $[Z]$, as was expected based on the principle of reciprocity and the use of the Galerkin method by EMBPro to solve the method of moments problem.

Due to the symmetry requirement on the impedance matrix required by the Harrington-based mode calculation method another approach for modeling the plate was pursued. As a result of the problem associated with using a fully-meshed wire grid, a parallel-wire model was used to approximate the plate. This was thought to be a reasonable approximation based on the fact that the antenna orientation would be parallel with the wires forming the model of the plate, as shown in Figure 26.

65
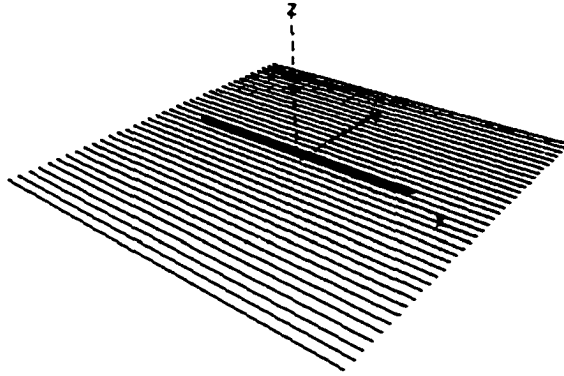
Figure 26:Antenna above the parallel wire approximation of a plate. The antenna is centered on the $Z$-axis.

However, several questions remained to be answered: what wire radius should be used, how

close should the parallel wires be placed, how many wires should be used and what antenna segment

and wire segment sizes should be used?

The antenna segment and wire segment sizes were both chosen to be 0.508 cm in length based

on the $\frac{\lambda}{10}$ - $\frac{\lambda}{20}$ upper limit in size and the results of the work completed for the one-dimensional

case. The number of wires, their radius and the spacing of the wires are related by equations 80 and

81 from [20] and [21].

$$D_w = \frac{W}{N\pi}$$  (80)

This translates to a spacing given by equation 81.

$$S = N\pi$$  (81)

where $D_w$ is the diameter of the wire, $W$ is the width of the plate, $N$ is the number of wires, and

$S$ is the distance between each of the parallel wires. While these ratios were originally used to

model long, narrow plates, the results obtained in this research suggest that they may be extended

66

to square plates. The width and length of the plates were pre-determined based on the type of experiment that was going to be run. However, $N$ and $D_w$ were determined using the geometry guidelines described in the EMBPro manual, and by comparing the surface current distribution and radiation patterns calculated using a characteristic mode approach with the current and radiation patterns calculated using results obtained from a completed EMBPro evaluation of the model.

Initially, an example plate was modeled using several models and each successive model used an increasing number of parallel wires positioned so that they satisfied the spacing and wire constraints described above. However, as the number of wires was increased and the spacing between the wires decreased, the surface currents and far-field patterns obtained using characteristic mode analysis were not converging, as would be expected, toward the same solution obtained using an EMBPro analysis of the model. Review of the program $cmcomp01.c$, used to calculate the characteristic modes, suggested that changing the matrix conditional cut-off number, $\mu_{min}$, may resolve the problem. This is better understood by reviewing Harrington's procedure for calculating the eigenvalues of the impedance matrix.

The eigenvalues of $[Z]$ will satisfy the equation (40), $XJ_n = \lambda_n RJ_n$, shown here again for clarity. In theory, solution of this equation requires that $R$ should be positive definite. However, due to numerical inaccuracies this may not be true. Therefore, Harrington modifies the standard approach for calculating $\lambda_n$ by first computing the matrix $[U]$, that diagonalizes $R$ such that

$$[\mu] = \left[\tilde{U}RU\right] = \begin{bmatrix} \mu_1 & 0 & 0 & \cdots \\ 0 & \mu_2 & 0 & \cdots \\ \cdots & \cdots & \cdots & \cdots \end{bmatrix} \tag{82}$$

where the $\mu_i$ are the eigenvalues of R ordered $\mu_1 \geq \mu_2 \geq \cdots$. Pre-multiplying the generalized form of equation (40) by $\left[\tilde{U}\right]$ and using the results of equation (82), results in

$$\left[\tilde{U}XU\right]\left[\tilde{U}I\right] = \lambda\,[\mu]\,[UI] \tag{83}$$

67

where $I$ is the identity matrix. However, only the larger $\mu_i$ can be considered accurate and all

$\mu_i \leq M\mu_1$ equal to zero, where $M$ is some small number based on the estimated accuracy of $[R]$.

Harrington suggests setting $M = 10^{-3}$. This value of $M$ was initially used in our characteristic

mode software. However, far-field patterns using characteristic modes computed using this value

failed to agree with the results obtained with EMBPro. This may have been due to the fact that the

software for this research was written using variables of type *float* versus using variables of type

*double* and that the value chosen for $M$ was too large. As a result, $M$ was decreased such that $M$

= 0.000001. Following this change, re-calculation of characteristic mode data indicated that the

surface current distribution and the radiation patterns were very similar to those that were computed

using EMBPro. This will be seen by comparing the data in Figure 61 with that of Figures 62 - 66.

Once convergence of the results for the test cases was obtained, the number of wires and their

spacing for a given plate size was quickly determined. A ratio of 15 wires per 3.81 cm was chosen

based on preliminary characteristic mode algorithm development. Additionally, as a result of dis-

cussions with Dr. Rockway [22], an odd number of wires were used to model the plate. This was

done in order to keep a wire of the plate centered under the antenna wire. He thought that given

the small distances between the antenna and the collection of parallel wires more accurate results

would be obtained if the antenna was placed directly over a wire.

Generating well formed NEC file descriptions of the plate and antenna remained the last signif-

icant step in transitioning from one-dimensional geometries to two-dimensional geometries. Be-

cause parallel wires were used to generate the plate approximation, the process of creating the

NEC files was simplified considerably. First, the number of wires, their spacing, segment length

and radii were entered into a Matlab M-file and a NEC description of the geometry was generated.

Then using the same radii and segment size, the antenna information was appended to the end of the

68

NEC file. Formatting the NEC file in this way facilitated the interpretation and post-processing of EMBPro products that described the current node locations and the impedance matrix. This eventually enabled the characteristic mode results to be converted into a relatively easy-to-understandable graphical format.

## 4.2.2 Computational and Experimental Work

The two-dimensional work was divided into six major sections. Initially, the changes in characteristic modes of the antenna and plate were examined as the antenna was moved across the face of the plate for various plate sizes. Similarly, characteristic mode changes were studied for a fixed plate size, but the antenna length and height above the plate were varied. Next, E- and H-plane measurements were compared for those computed using an antenna positioned at different locations above a plate. Then, the significance of each of the first four modes' contributions to the overall E- and H-plane patterns was examined. Finally, results were obtained by comparing radiation patterns from a simple superposition of the isolated antenna and plate models, the characteristic mode approach, and a method of images approach.

### 4.2.2.1 Characteristic Modes vs. Antenna Position and Plate Size

Three different plate sizes, $0.75\lambda \times 0.75\lambda$, $1.00\lambda \times 1.00\lambda$ and $1.25\lambda \times 1.25\lambda$, and six antenna locations on each plate were used to investigate the response of the characteristic modes for the antenna / plate systems. The center of the antenna was positioned at six different locations at a height of 0.254 cm above the plate as shown in Table 7. These positions represent a uniform distribution of antenna locations in one quadrant of the plate.

These positions are illustrated in the Figure 27.

69

| Position | Description |
|---|---|
| 1 | The center of the plate |
| 2 | Half-way between the center of the plate and the point where the center of the antenna lies when one end of the antenna is flush with the side edge of plate |
| 3 | At a location such that one edge of the antenna is flush with the side of the plate |
| 4 | Center of the plate horizontally, but moved vertically away from the center the same distance as the center was moved toward the side edge in the second position |
| 5 | The antenna is flush with the top edge |
| 6 | The center of the antenna is moved horizontally as in position two and vertically as position four |

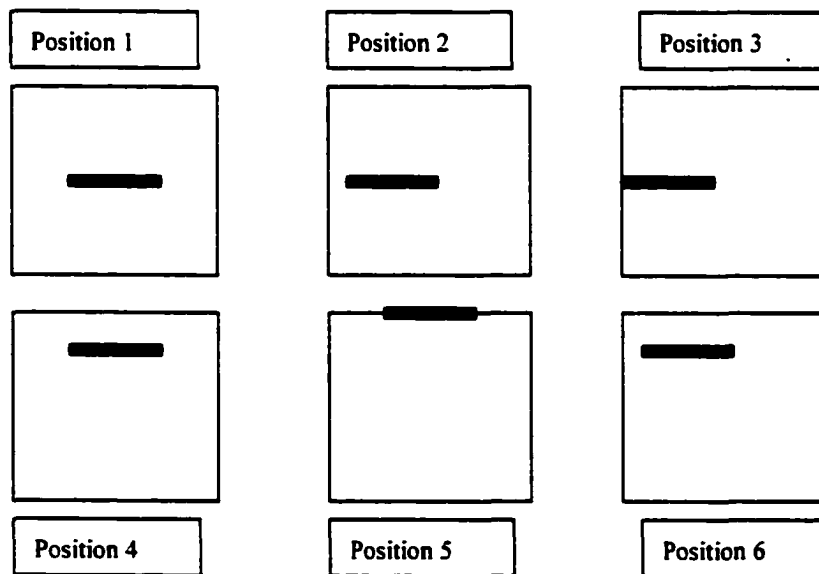Table 7:Antenna test positions above the plates



Figure 27:Antenna (heavy black bar) positioned at each of the approximate locations.

The modeling parameters used for this section of the work are provided in Tables 8 and 9.

The segment size for both the antenna and the wire was 0.508 cm. The antenna was positioned 0.254 cm above the plate, regardless of plate size or the $x$-$y$ location of the antenna center. The antenna was also parallel to the plate surface and to the wires forming the plate model. A schematic

70

| Plate Size | Number of Wires | Elements in each Wire |
|---|---|---|
| 0.75λ x 0.75λ | 37 | 18 |
| 1.00λ x 1.00λ | 49 | 24 |
| 1.25λ x 1.25λ | 61 | 30 |

Table 8:Number of Wires and the elements in each wire for the three plate sizes.

of this general arrangement was shown in Figure 26.

### 4.2.2.2    Isolated Plate Data

Based on the preceding development, the modes of the isolated plate and antenna were calculated. The first three dominant modes of each of these structures is shown in Figures 28 - 30. Note, these modes represent the first three, natural modes of each plate. In these figures, positive current densities are shown with a reddish hue and negative densities are shown with a bluish hue; the greater the surface current density. the deeper the color.
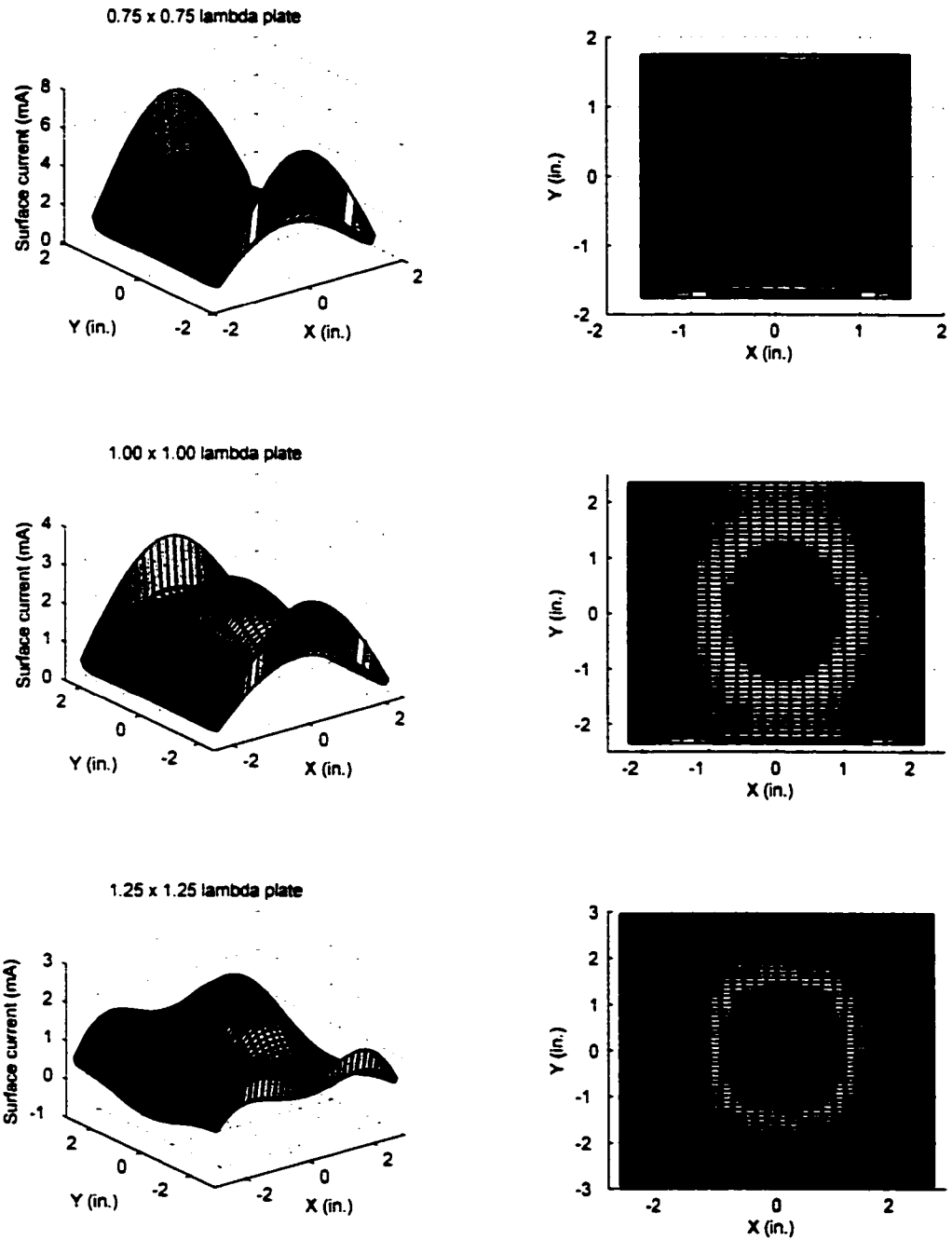
71

**0.75 x 0.75 lambda plate**

**1.00 x 1.00 lambda plate**

**1.25 x 1.25 lambda plate**

Figure 28:Oblique and overhead views of the first dominant modes of the isolated plates.

72

| Plate Size | Wire and Antenna Radii | Interwire Spacing |
|---|---|---|
| $0.75\lambda \times 0.75\lambda$ | $0.039332\ cm$ | $0.24713\ cm$ |
| $1.00\lambda \times 1.00\lambda$ | $0.039601\ cm$ | $0.24882\ cm$ |
| $1.25\lambda \times 1.25\lambda$ | $0.039764\ cm$ | $0.24983\ cm$ |

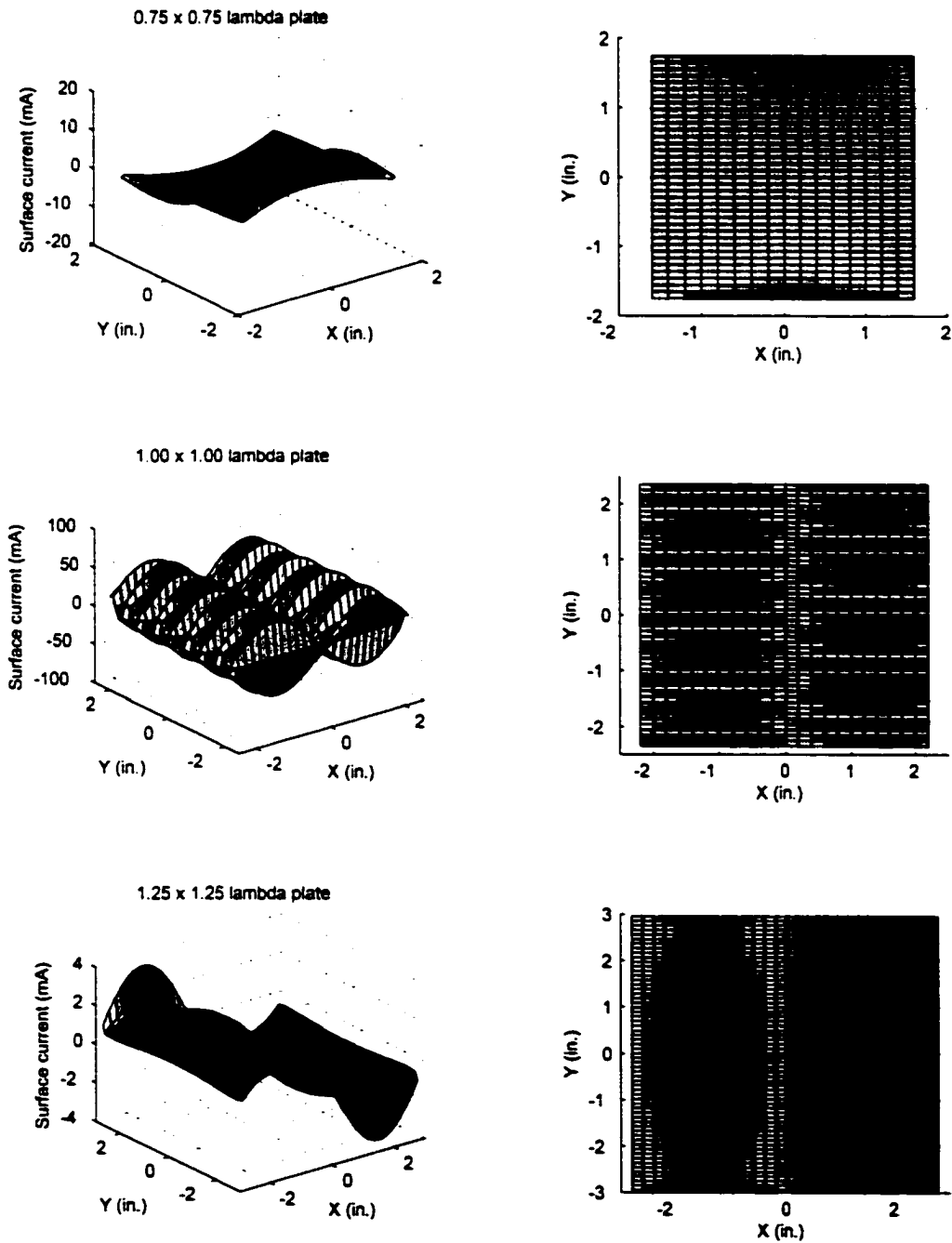Table 9:The wire and antenna radii and the interwire spacing for the three plate sizes.



73

Figure 29:Oblique and overhead views of the second dominant modes of the isolated plates.

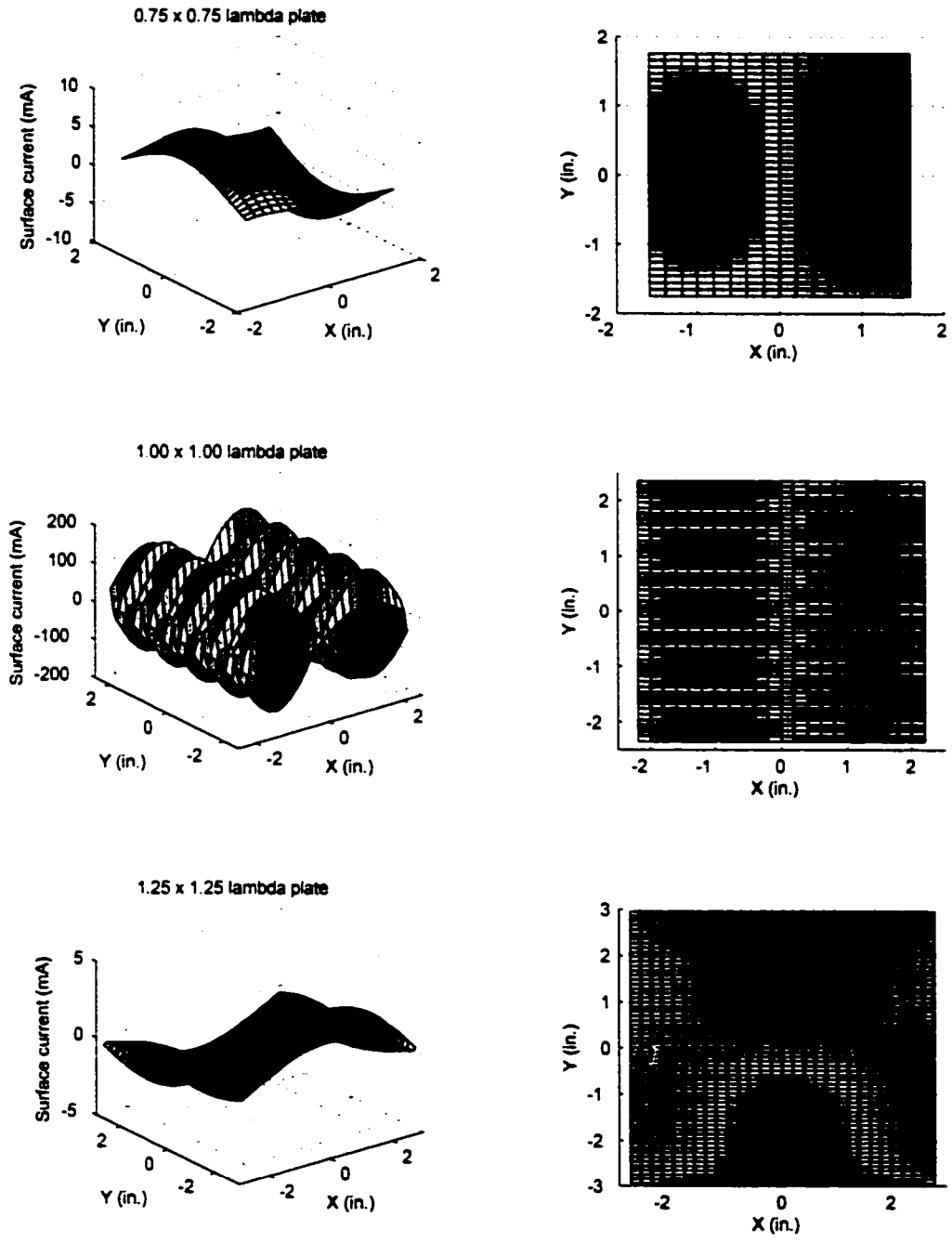Figure 30:Oblique and overhead views of the third dominant mode of the isolated plates.

Note that the order of dominance was determined not only by the eigenvalue magnitude, but also

74

by the modal excitation factor as discussed in Chapter 2. Refer to Figure 20 for the characteristic modes of the isolated dipole.

### 4.2.2.3    Characteristic Mode Interpretation for Isolated Plates

Depending on the size of the plate, the variation in characteristic mode shape for an isolated plate can be quite significant. For example, compare the variation between the first modes for the three different sized plates. For the $0.75\lambda \times 0.75\lambda$ plate, it takes until the third mode before there is significant distortion of the generally flat surface. Most of the variation in surface current density takes place along the edges of the plate.

The $1.0\lambda \times 1.0\lambda$ plate exhibits a similar distortion of the surface current density as in the $0.75\lambda \times 0.75\lambda$ example. However, the center of the plate exhibits significantly more distortion than was seen in the $0.75\lambda \times 0.75\lambda$ plate. In the second and third modes, the $1.0\lambda \times 1.0\lambda$ exhibits much greater distortion in the surface current density than was exhibited in the first mode. In both of these modes, the distortion looks very similar to identical sets of parallel standing waves. Additionally, the extrema of the second and third modes are generally greater than the magnitude of the first mode's surface. This may be related to the fact that the plate is $1.0\lambda \times 1.0\lambda$ square and more readily supports characteristic modes of this shape.

Finally, the $1.25\lambda \times 1.25\lambda$ plate shows the most variation in the characteristic mode surface from mode to mode. In the first mode, the edge currents that were so prominent in the first modes of the other plates are comparatively attenuated. However, in the second and third modes the edge currents increase significantly.

### 4.2.2.4    Antenna / Plate System Data

Characteristic mode data was obtained by computer calculation for the antenna / plate systems.
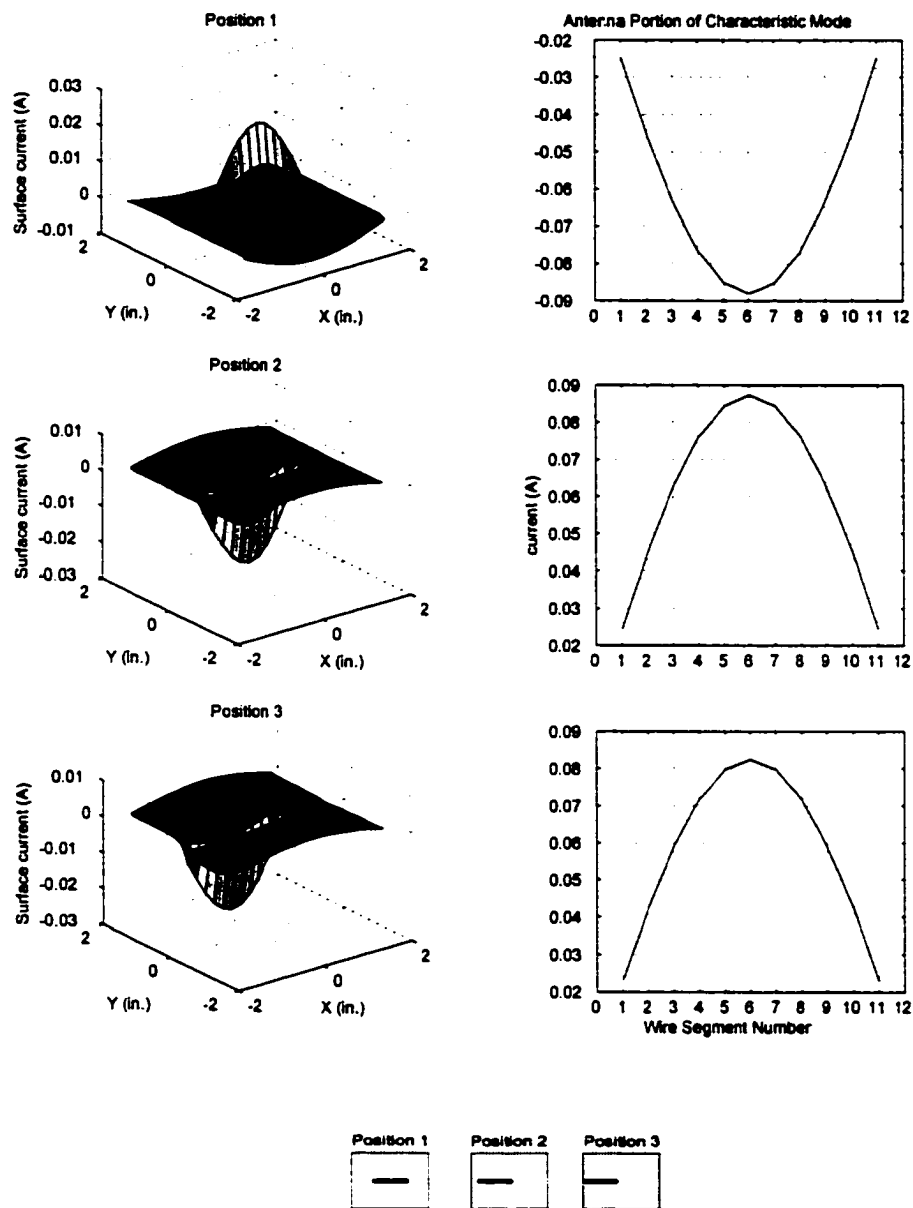
75

This data is shown in Figures 31 - 48.



Figure 31:The plate and antenna portion of the 1st dominant system mode for the 0.75 x 0.75λ system for antenna positions 1 - 3.

76

Figure 32:The plate and antenna portions of the first dominant system mode for the 0.75λ x 0.75λ system for antenna positions 4 - 6.

77

Figure 33:The plate and antenna portions of the second dominant system mode for the $1.0\lambda$ x $1.0\lambda$ system for antenna positions 1 - 3.
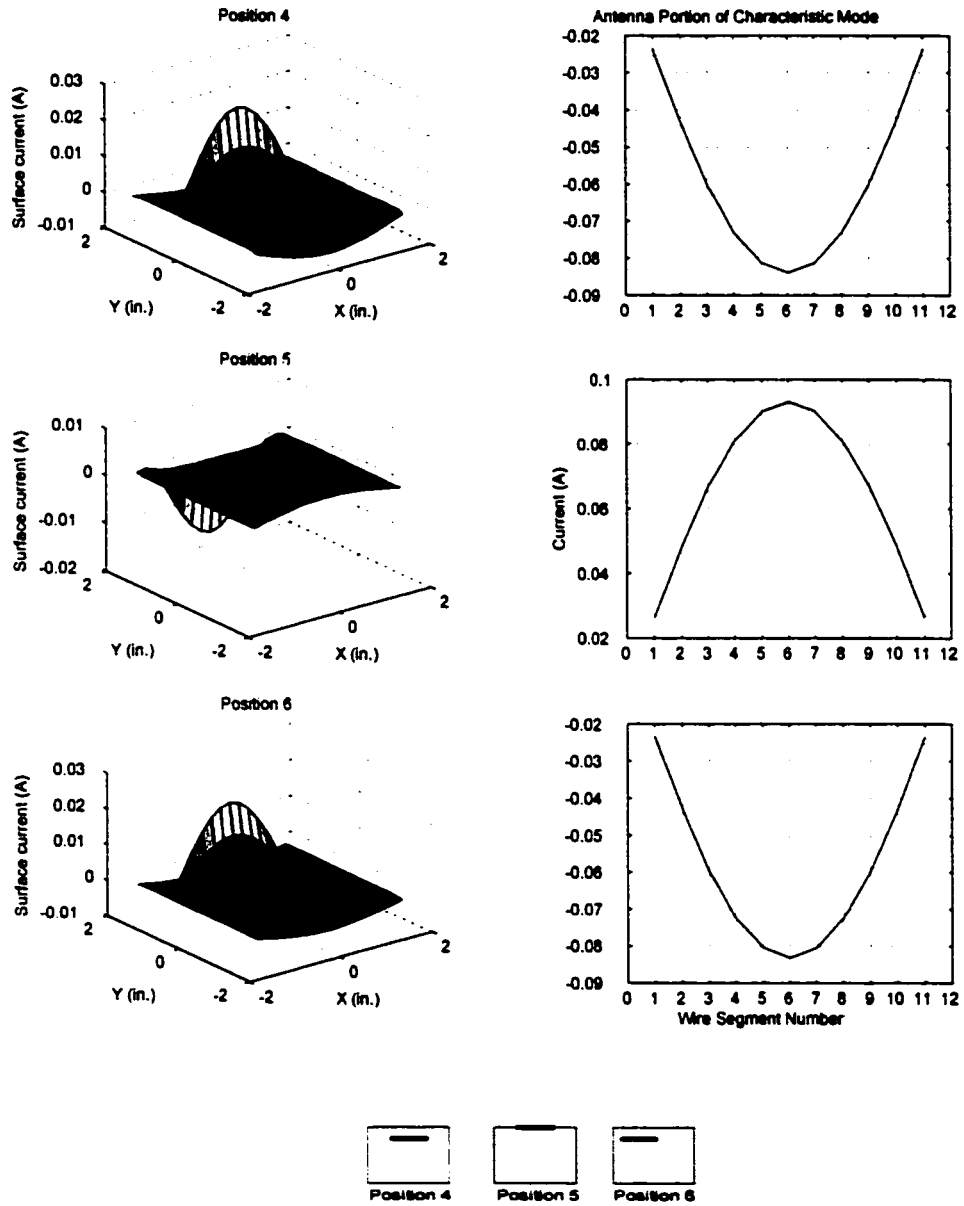
78

Figure 34:The plate and antenna portions of the first dominant system mode for the $1.0\lambda$ x $1.0\lambda$ system for antenna positions 4 - 6.

79

Figure 35:The plate and antenna portions of the first dominant system mode for the 1.25λ x 1.25λ system for antenna positions 1 - 3.

80

Figure 36:The plate and antenna portions of the first dominant system mode for the $1.25\lambda$ x $1.25\lambda$ system for antenna positions 4 - 6.
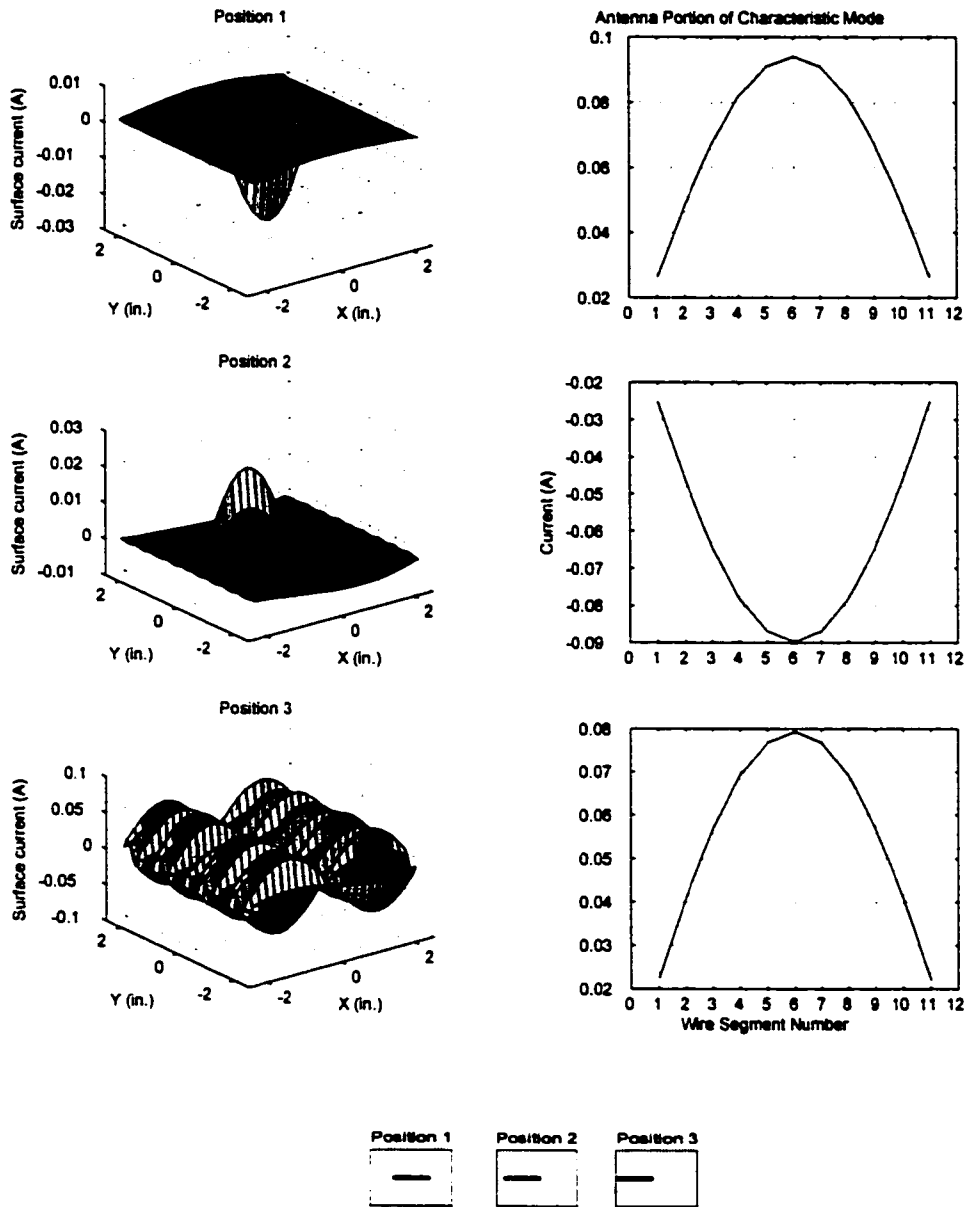
81

Figure 37:The plate and antenna portions of the second dominant system mode for the $0.75\lambda$ x $0.75\lambda$ system for antenna positions 1 - 3.

82

**Figure 38:**The plate and antenna portions of the second dominant system mode for the 0.75λ x 0.75λ system for antenna positions 4 - 6.

83

Figure 39:The plate and antenna portions of the second dominant system mode for the $1.0\lambda$ x $1.0\lambda$ system for antenna positions 1 - 3.
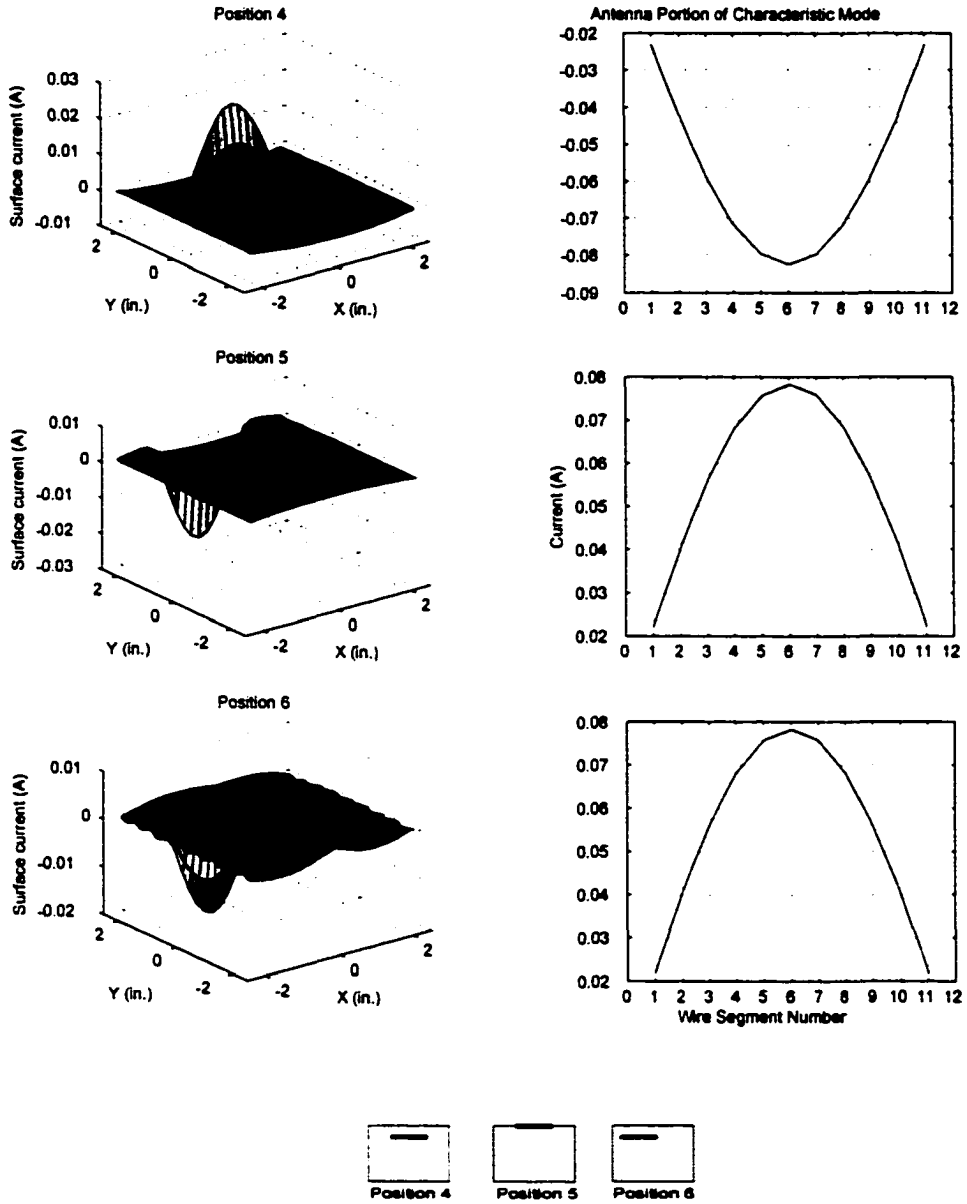
84

Figure 40:The plate and antenna portions of the second dominant system mode for the $1.0\lambda$ x $1.0\lambda$ system for antenna positions 4 - 6.
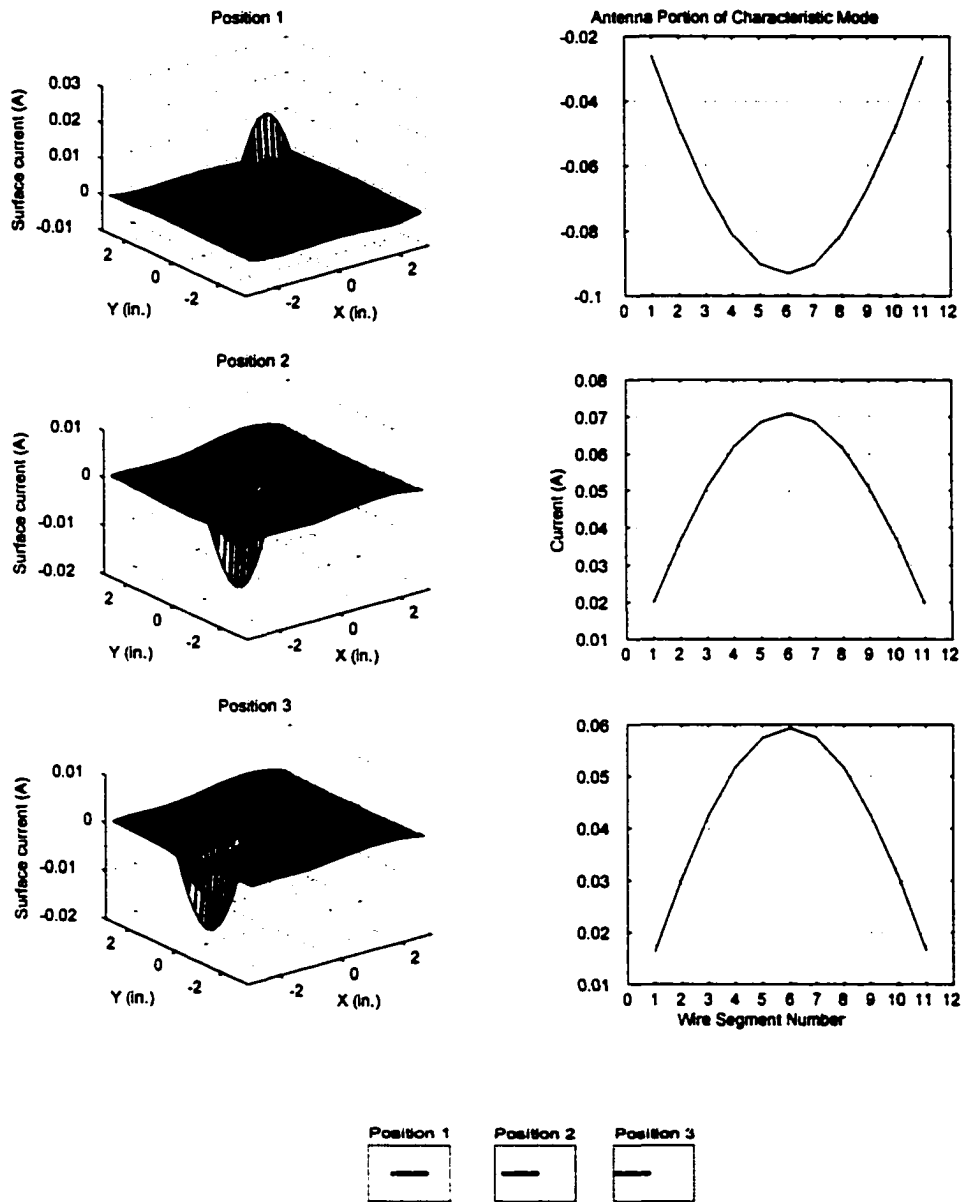
85

Figure 41:The plate and antenna portions of the second dominant system mode for the 1.25λ x 1.25λ system for antenna positions 1 - 3.
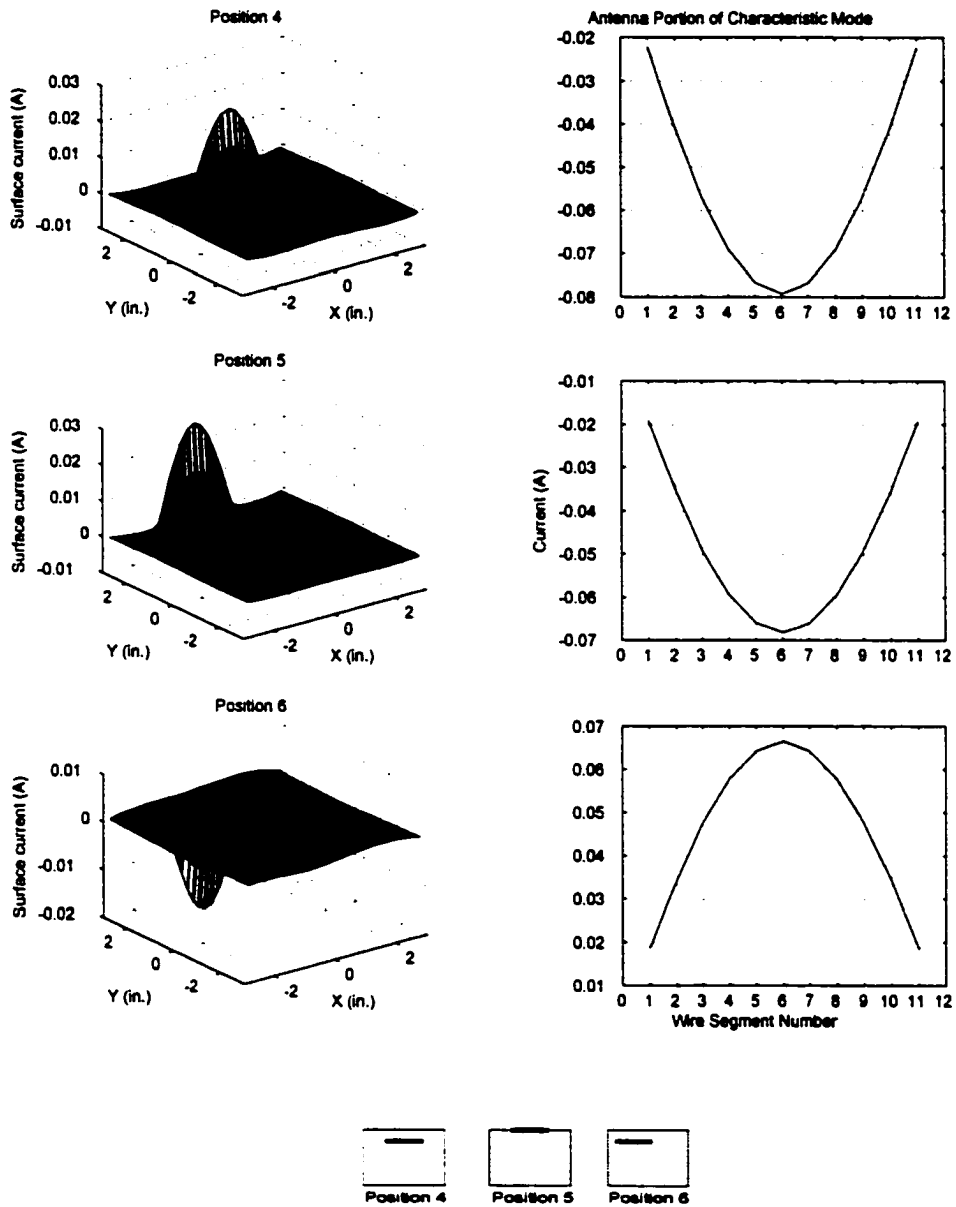
86

Figure 42:The plate and antenna portions of the second dominant system mode for the 1.25$\lambda$ x 1.25$\lambda$ system for antenna positions 4 - 6.

87
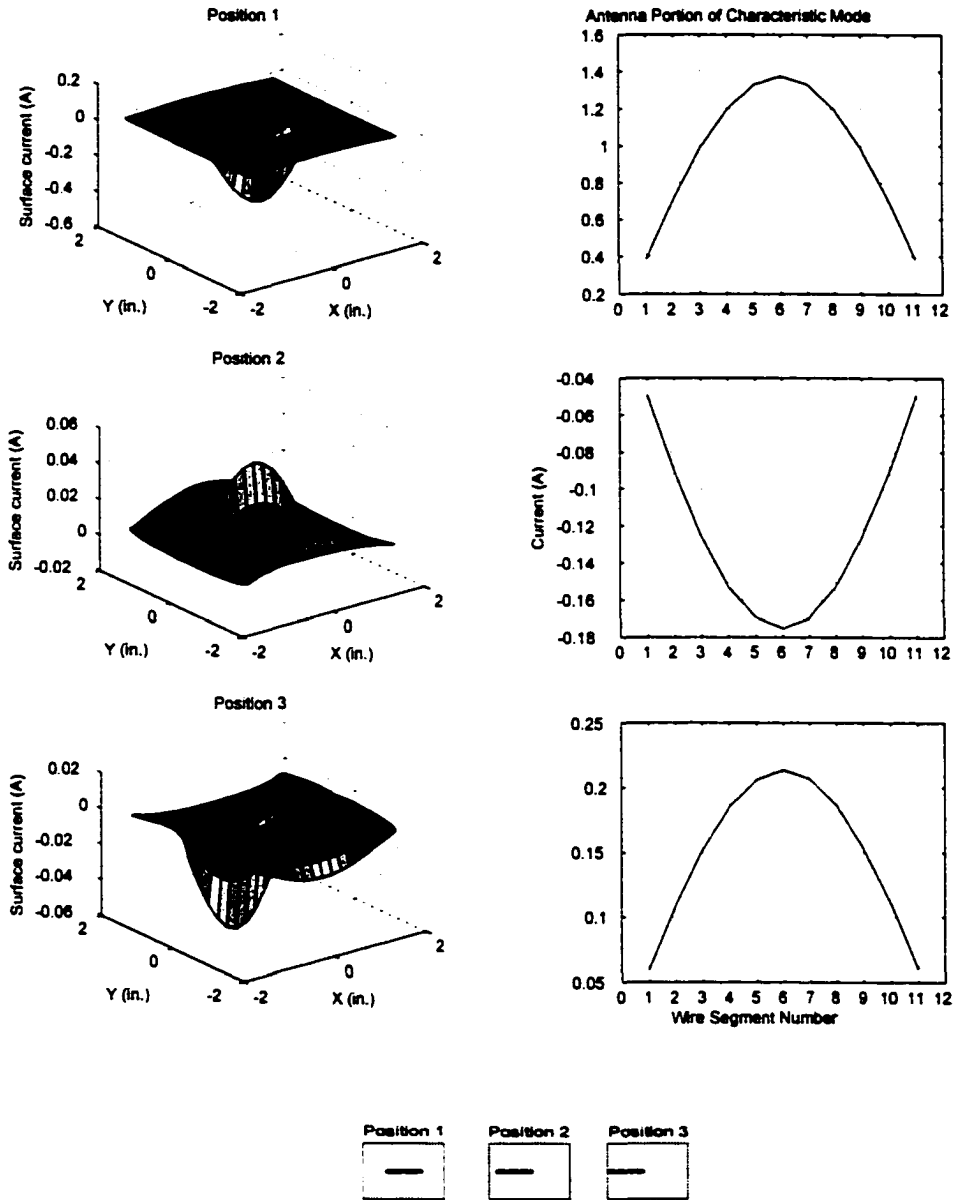
Figure 43:The plate and antenna portions of the third dominant system mode for the $0.75\lambda$ x $0.75\lambda$ system for antenna positions 1 - 3.

88
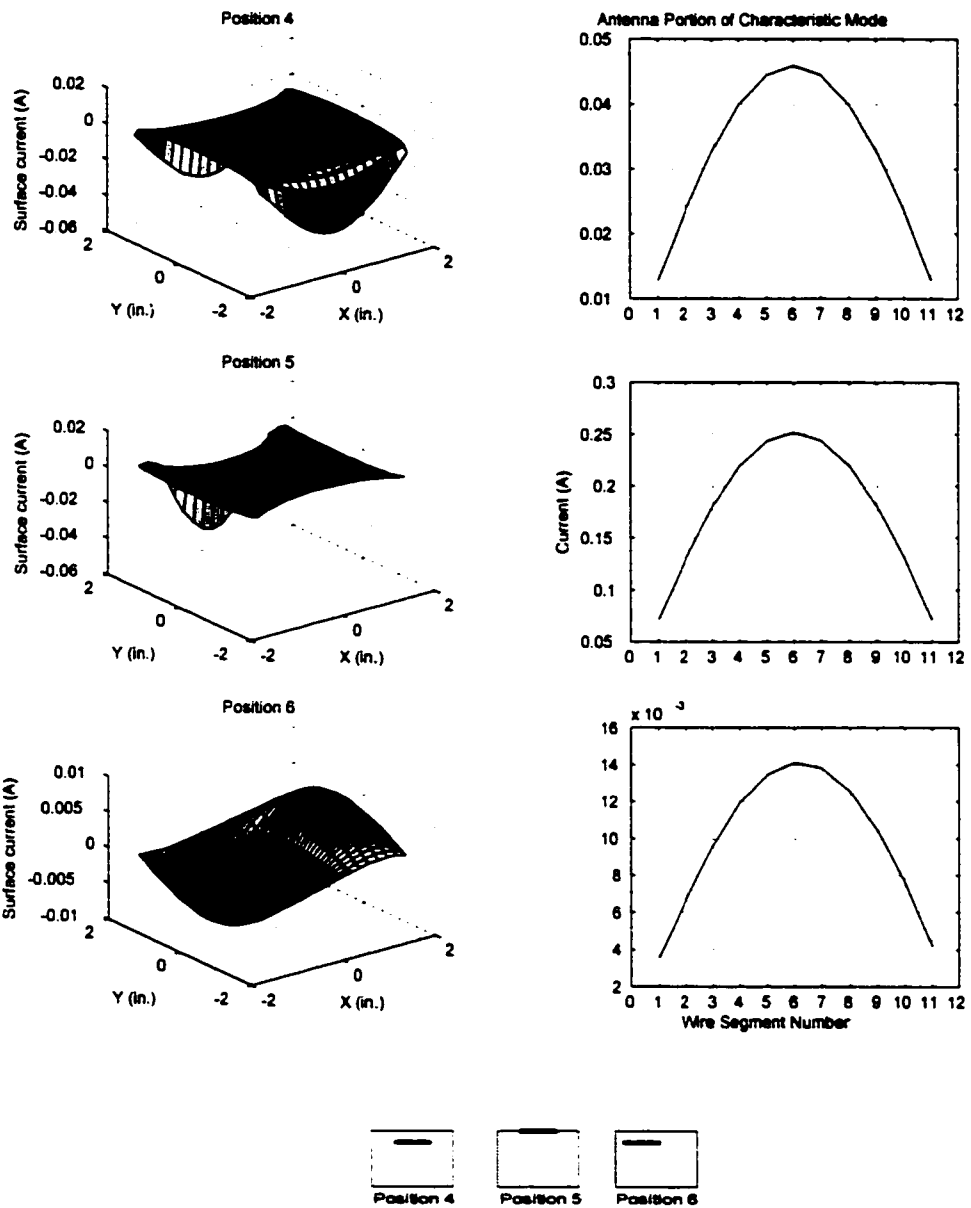
**Figure 44:** The plate and antenna portions of the third dominant system mode for the $0.75\lambda$ x $0.75\lambda$ system for antenna positions 4 - 6.

89
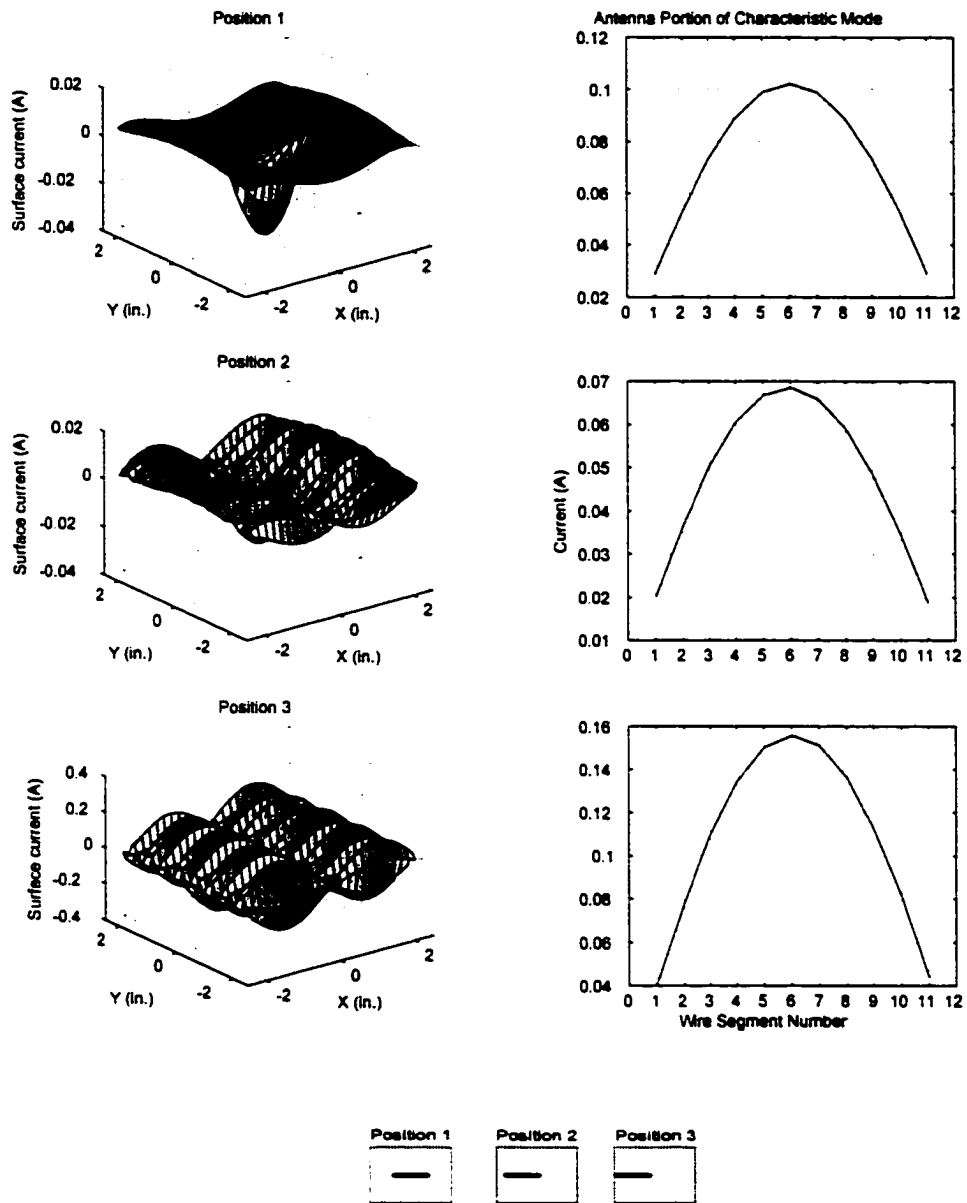
Figure 45:The plate and antenna portions of the third dominant system mode for the $1.0\lambda \times 1.0\lambda$ system for antenna positions 1 - 3.
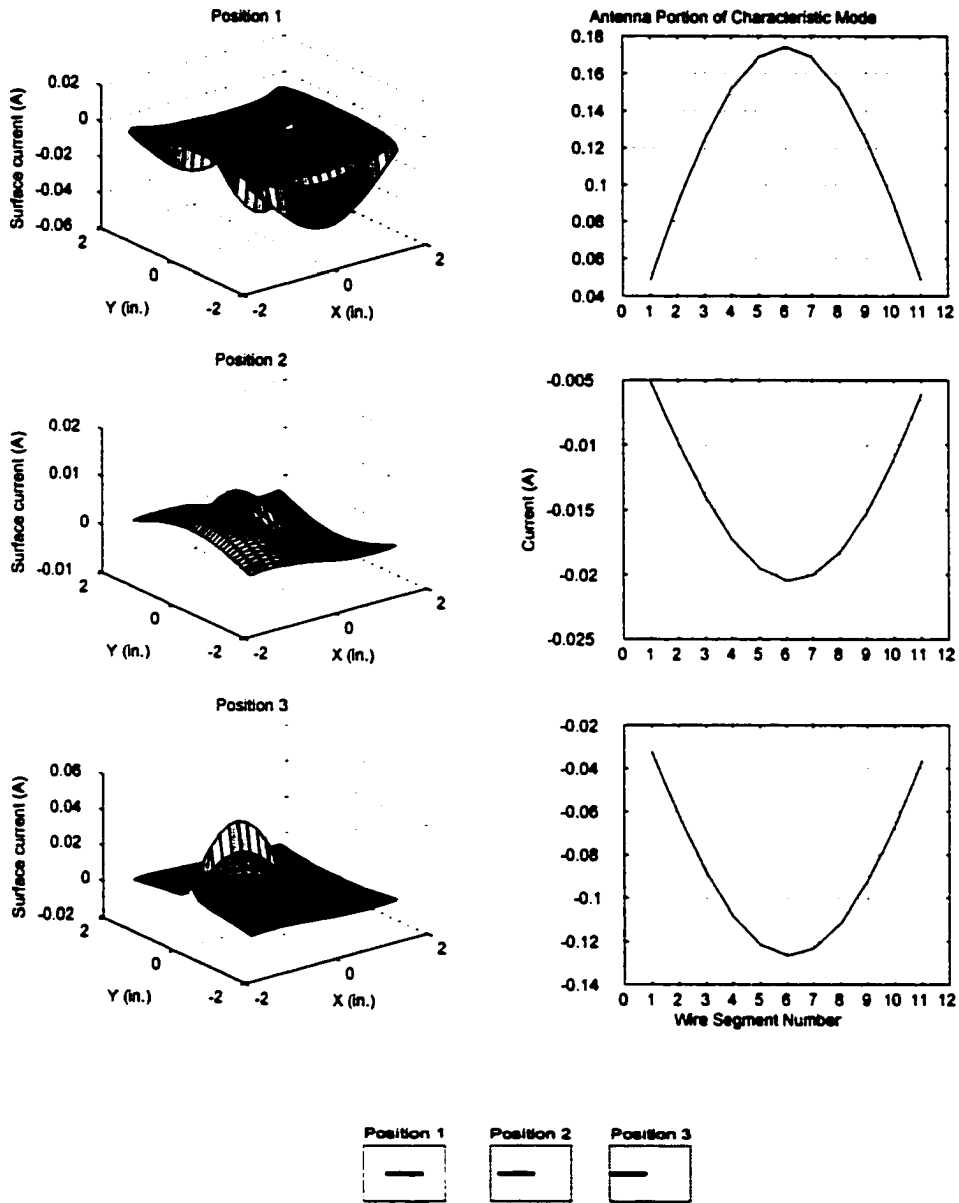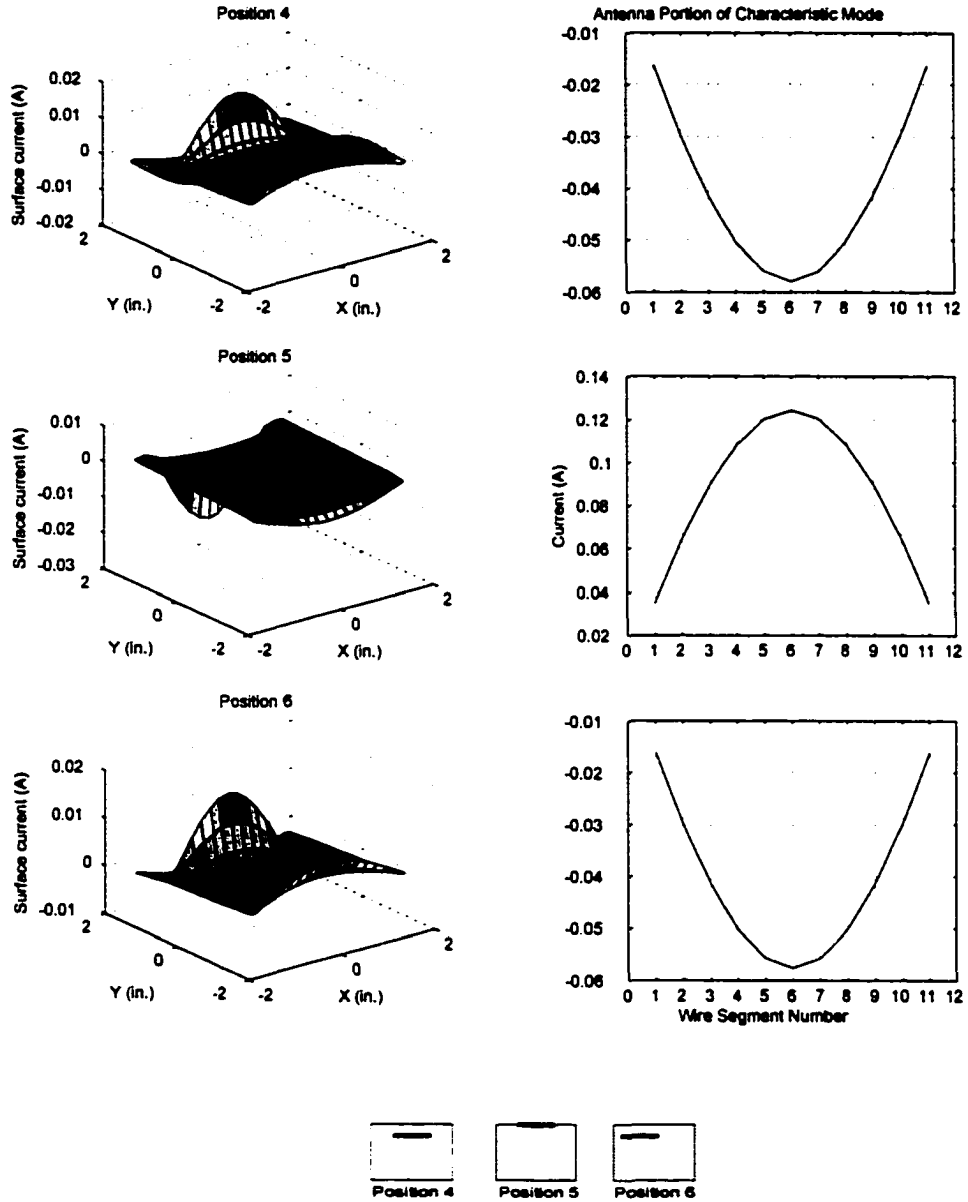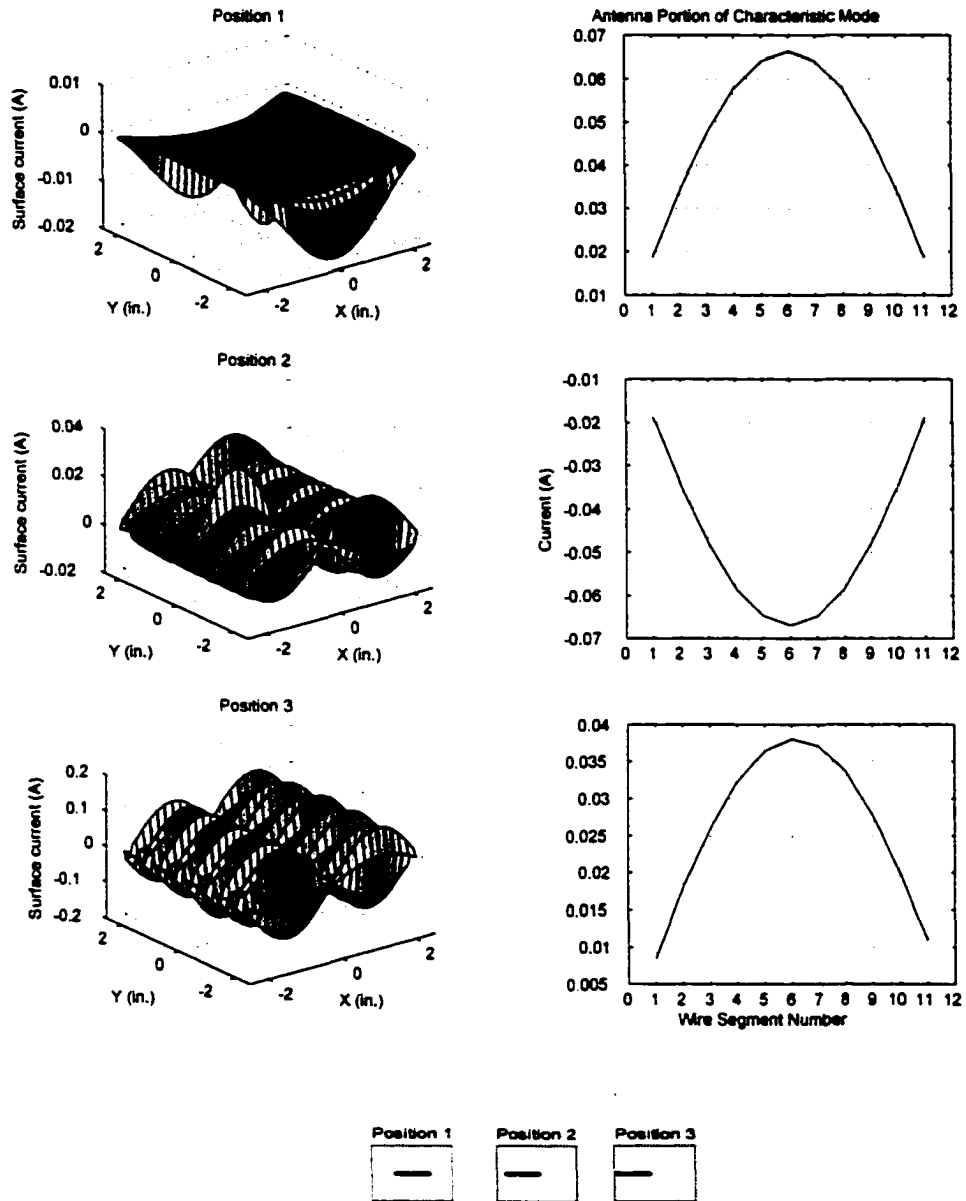
90

Figure 46:The plate and antenna portions of the third dominant system mode for the $1.0\lambda$ x $1.0\lambda$ system for antenna positions 4 - 6.

91

Figure 47:The plate and antenna portions of the third dominant system mode for the 1.25λ x 1.25λ system for antenna positions 1 - 3.

92
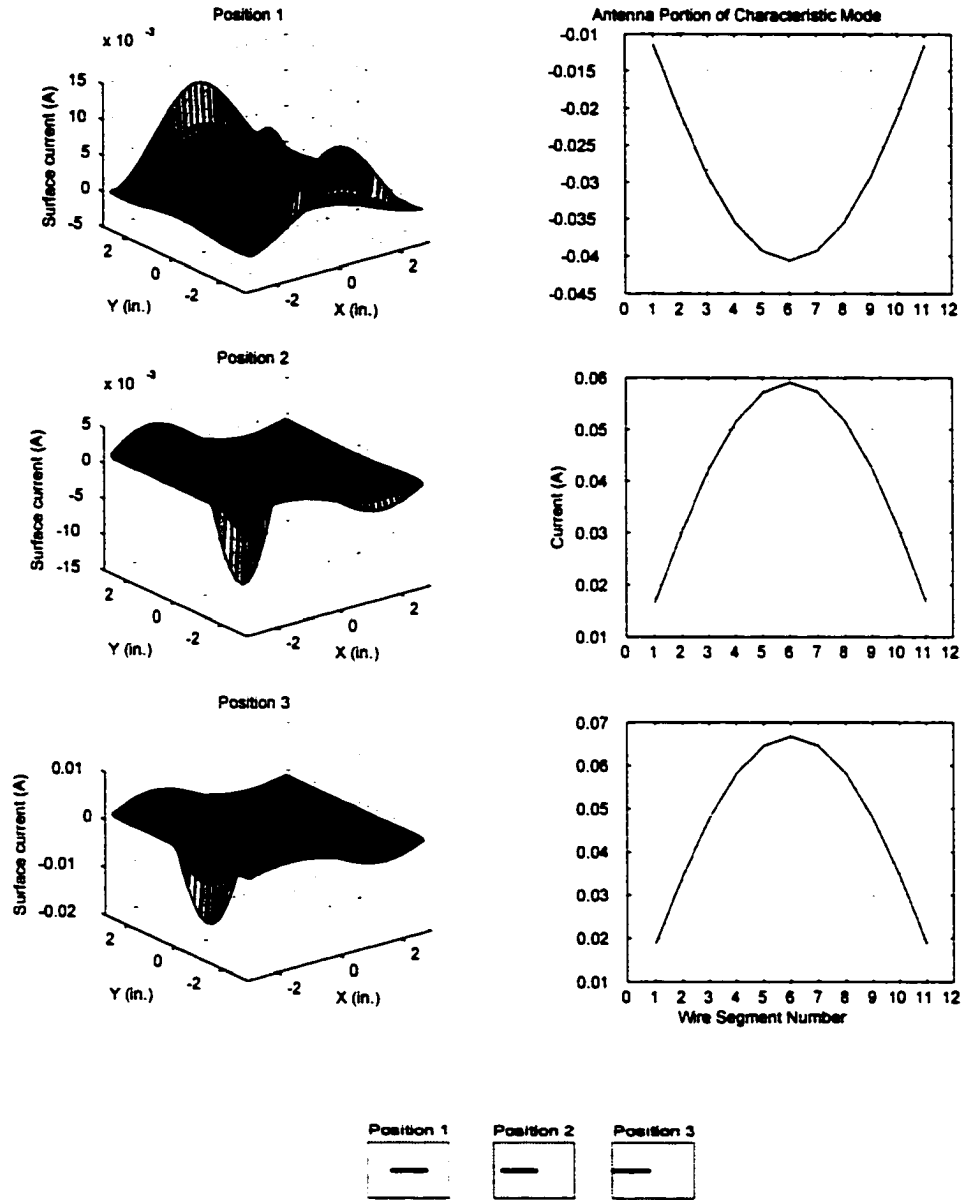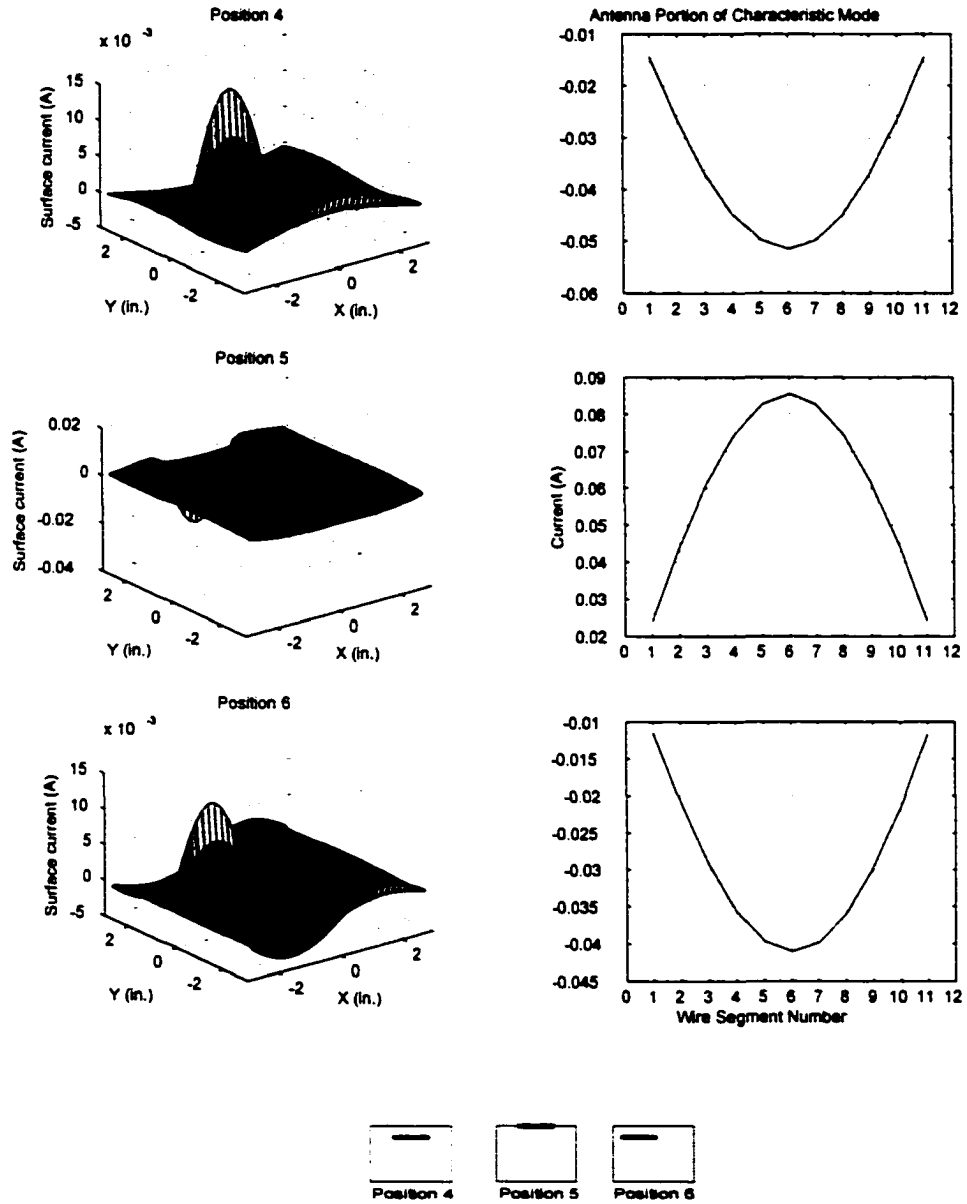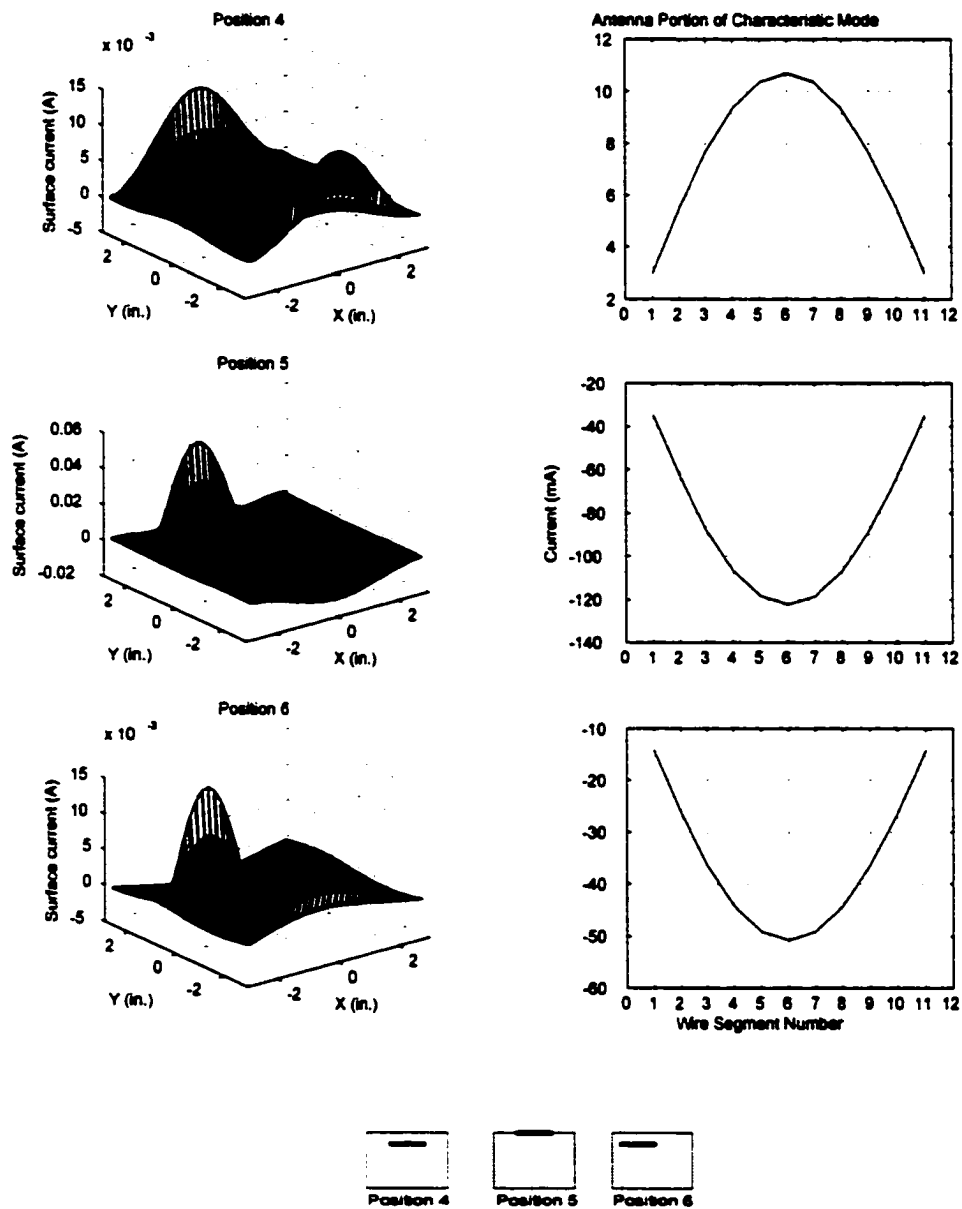
Figure 48:The plate and antenna portions of the third dominant system mode for the 1.25λ x 1.25λ system for antenna positions 4 - 6.

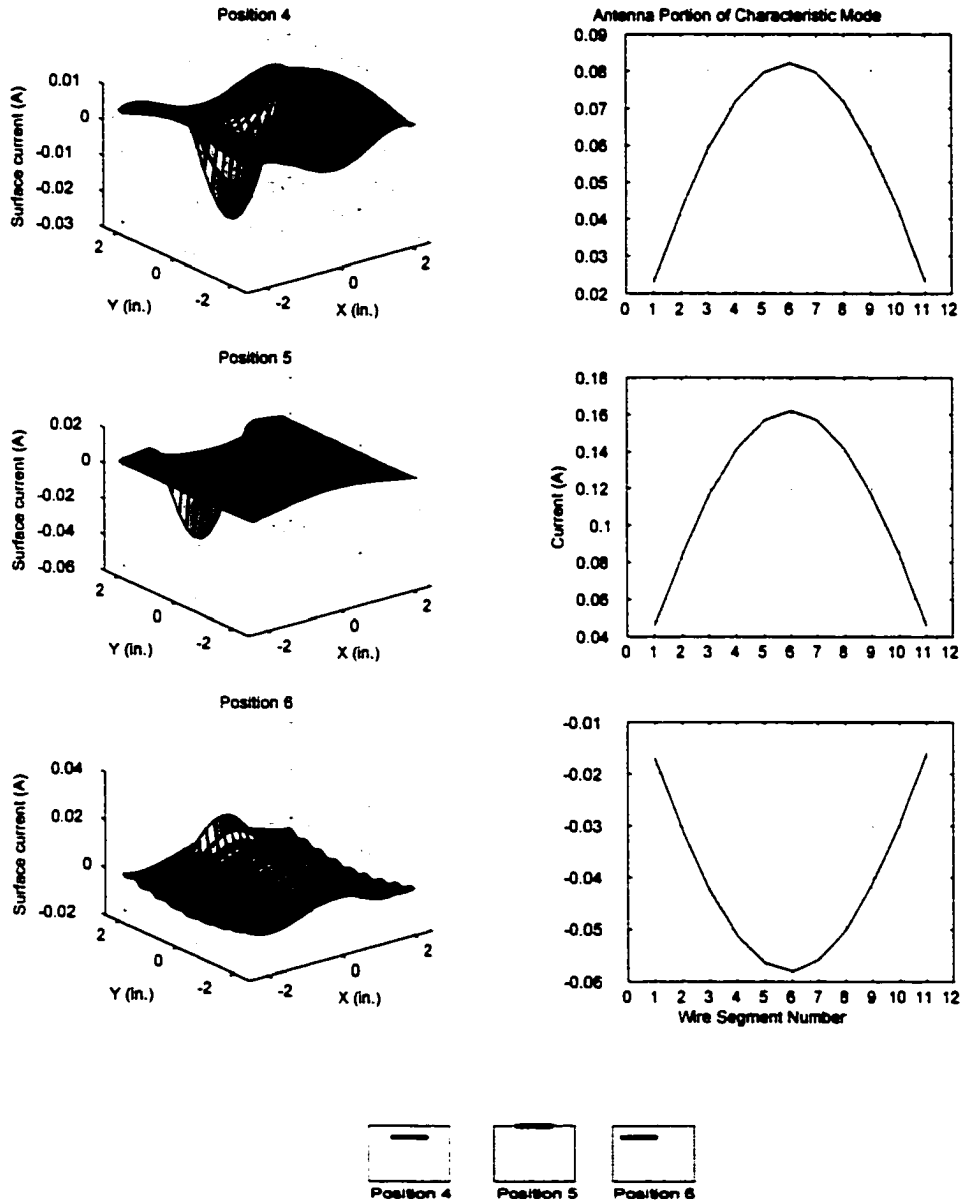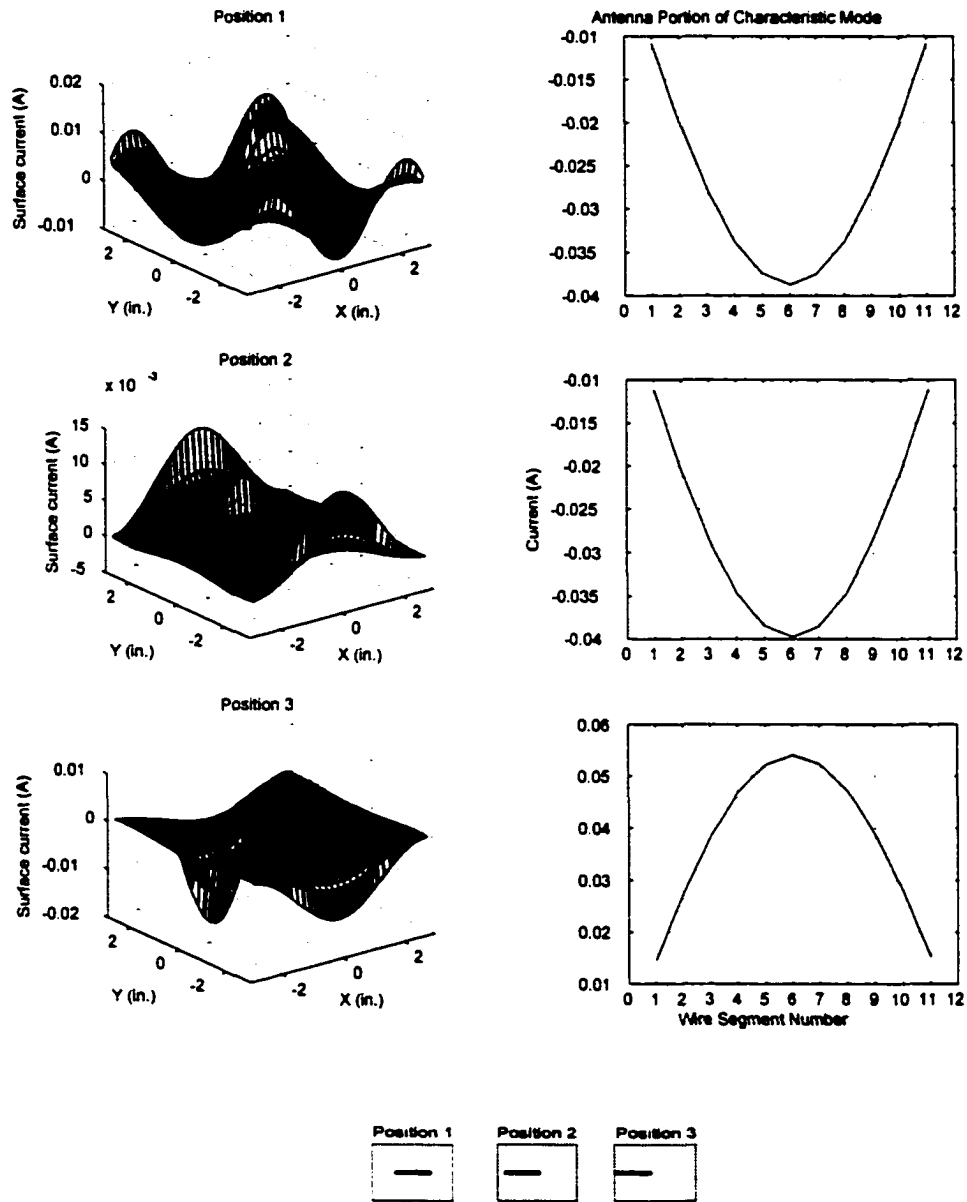### 4.2.2.5    Characteristic Mode Interpretation for Antenna / Plate Systems

Analysis of the overall system characteristic mode response indicates a marked difference in the

93

those portions of the response that lie on the antenna versus those portions that lie on the surface of the plate. Figures 31 - 48 indicates that the antenna portion of all three dominant mode responses for all three plates looks very similar to the isolated dipole's dominant characteristic mode response. This indicates that in the case of the dipole, a resonant sized antenna, the mutual impedance effect from the plate is not large enough to distort the first three dominant modes of the antenna.

However, the plate portion of the system characteristic modes for all three plate sizes indicates a more complex response. This response can be divided into two main parts: a localized response and a generalized response. The localized response appears to be a 180 degree, attenuated image of the antenna portion of the system characteristic mode. However, the generalized response of the plate portion is not so simple to describe. For the first modes of all the plates at all the positions, the generalized response of the plate appears to be a uniform current distribution. The major exception to this appears to be for the 1.0 $\lambda$ x 1.0$\lambda$ plate for the antenna at positions three and six. Note that these positions roughly correspond to the positions of maxima or minima of the second and third dominant mode of the isolated 1.0 $\lambda$ x 1.0$\lambda$ plate.

For the second modes of all plate sizes, the plate portion of the system response begins to show more variation in the appearance of the generalized response. However, even these responses seem to be very similar to the shapes found in the isolated plate analysis. For example, the generalized portion of the 0.75 $\lambda$ x 0.75$\lambda$ plate responses for the second dominant system mode are similar to the first, second, and third modes of the isolated 0.75 $\lambda$ x 0.75$\lambda$. For antenna position three, the generalized portion appears to be most similar to the uniform current shape.

The third mode generalized responses for all plate sizes are similar to the type of responses seen in the second mode generalized responses. However, certain generalized responses do not look like earlier isolated plate responses, but may have similarity to the shapes of higher order modes of the

94

isolated plates. Specific examples of this occurrence are in position six for the third dominant mode of the 0.75 $\lambda$ x 0.75$\lambda$ system and position one for the third dominant mode of the 1.25 $\lambda$ x 1.25$\lambda$ system.

### 4.2.2.6    Characteristic Modes vs. Antenna Length

Antenna length was the second parameter varied while observing the effect of this operation on the isolated characteristic modes of the antenna and the modes of the antenna / plate system. A 1.25$\lambda$ x 1.25$\lambda$ plate size was used in all the studies and the antenna was either 0.42$\lambda$ or 0.58$\lambda$ in length. The antenna was positioned at 0.254 cm above the center of the plate in both instances and the segment length for the wire and the plate was 0.508 cm. The wire radius for both the plate mesh and the antenna was 0.039764 cm and the wire spacing between elements of the plate was 0.24983 cm. Only the characteristic modes for the isolated antennas were computed as shown in Figure 49. The data for the isolated plate is the same as presented in Figures 28,29, and 30. The system models were created as previously described and the characteristic mode data was computed. The first three dominant modes for the 0.42$\lambda$ and 0.58$\lambda$ antenna systems are shown in Figures 50 and 51, respectively.

95
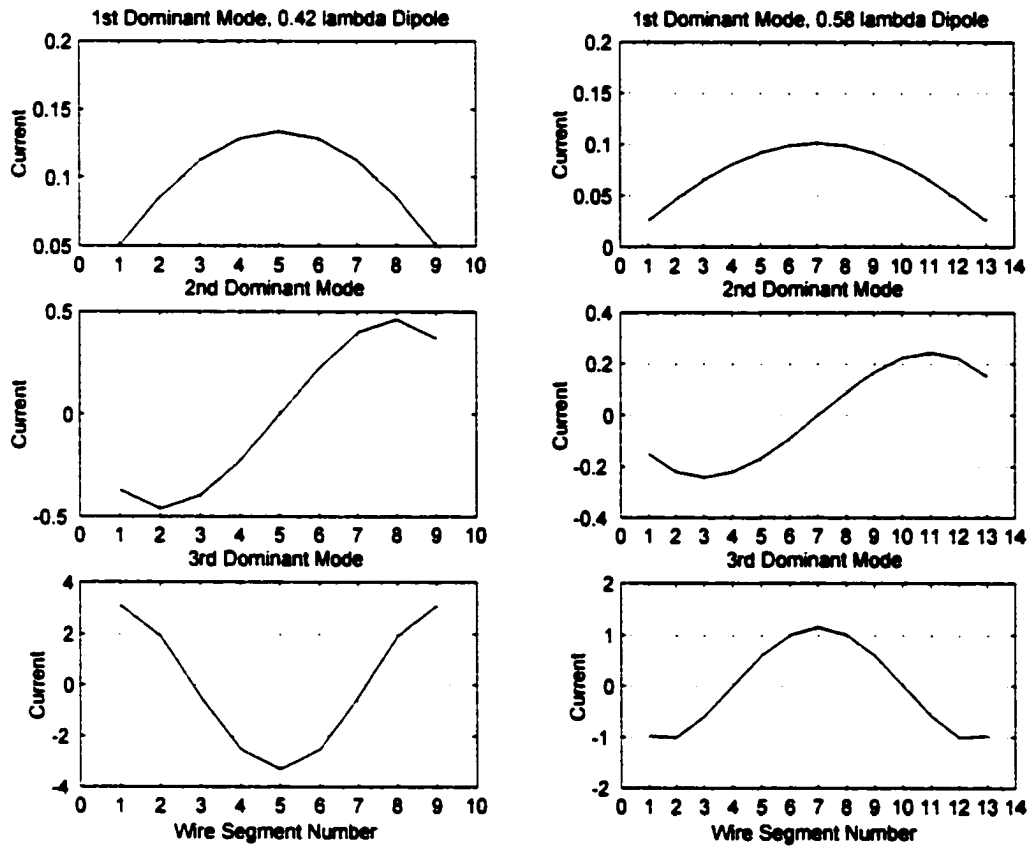
Figure 49:First three modes of the isolated 0.42λ and 0.58λ dipoles.
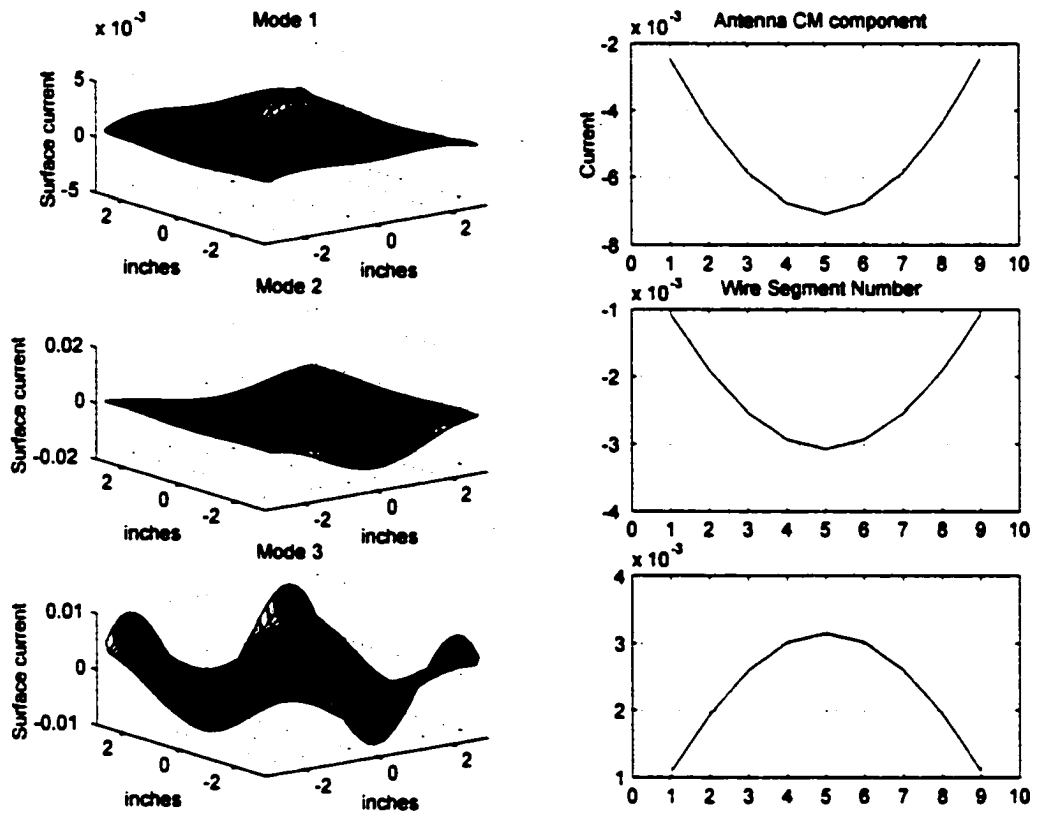
Figure 50:The plate and antenna portions of the first three characteristic modes for the 0.42$\lambda$ system.

97

Mode 1

Antenna Portion of Characteristic Mode

Surface current (mA)

Y (in.)  X (in.)

Mode 2

Surface current (mA)

Current (mA)

Y (in.)  X (in.)

Mode 3

Surface current (mA)

Y (in.)  X (in.)

Wire Segment Number
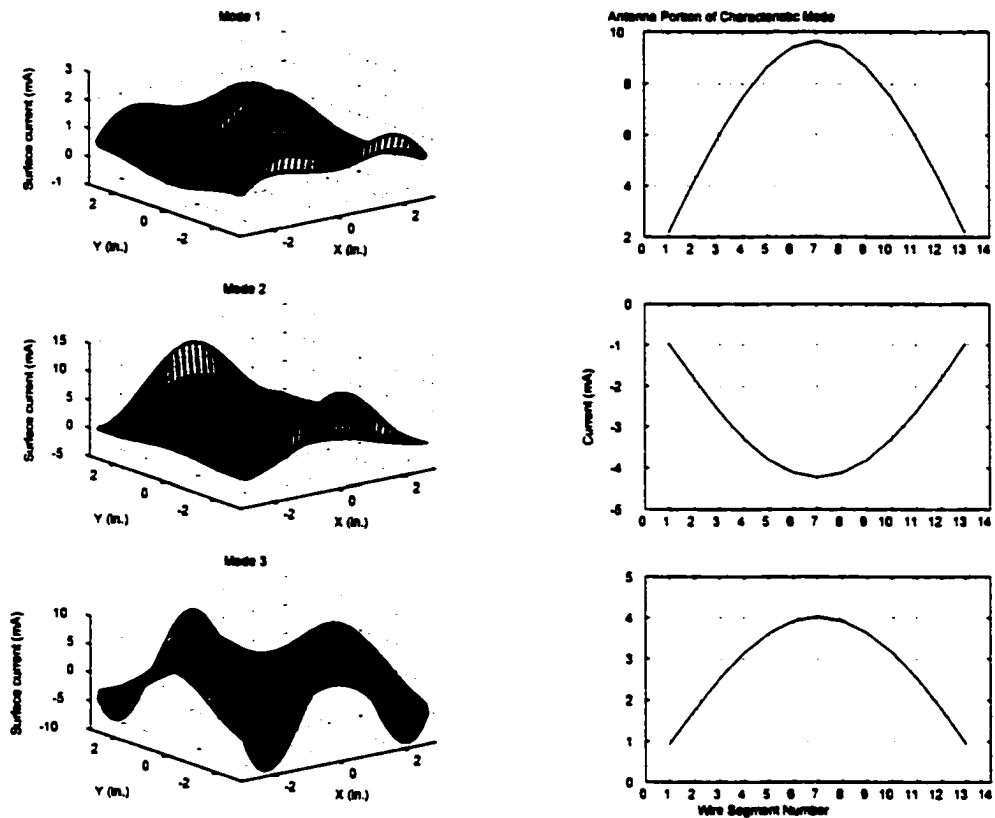
Figure 51:The plate and antenna portions of the first three characteristic modes for the 0.58λ system.

### 4.2.2.7    Characteristic Mode Interpretation for Variation in Antenna Length

The characteristic modes for the isolated 0.42 λ and 0.58 λ antenna look very similar to the same characteristic modes for the isolated 0.5 λ dipole except for a difference in peak values. This discrepancy is expected because of the input impedance difference for dipoles of different length. The modal responses of systems composed of a 0.42 λ or 0.58 λ dipole above a 1.25 λ x 1.25 λ plate demonstrate similar results to those obtained for the three different plate sizes. The plate portion of the 0.42 λ dipole system appears to have a generalized plate response and a localized antenna response. The generalized response for the first mode is very similar to first mode response for the

98

isolated 1.25 λ x 1.25 λ plate. Closer inspection of the generalized plate portions of the second and third system modes reveal that they are very similar to the fifth and eighth most dominant modes of the isolated 1.25 λ x 1.25 λ plate. These modes are shown in Figure 52.
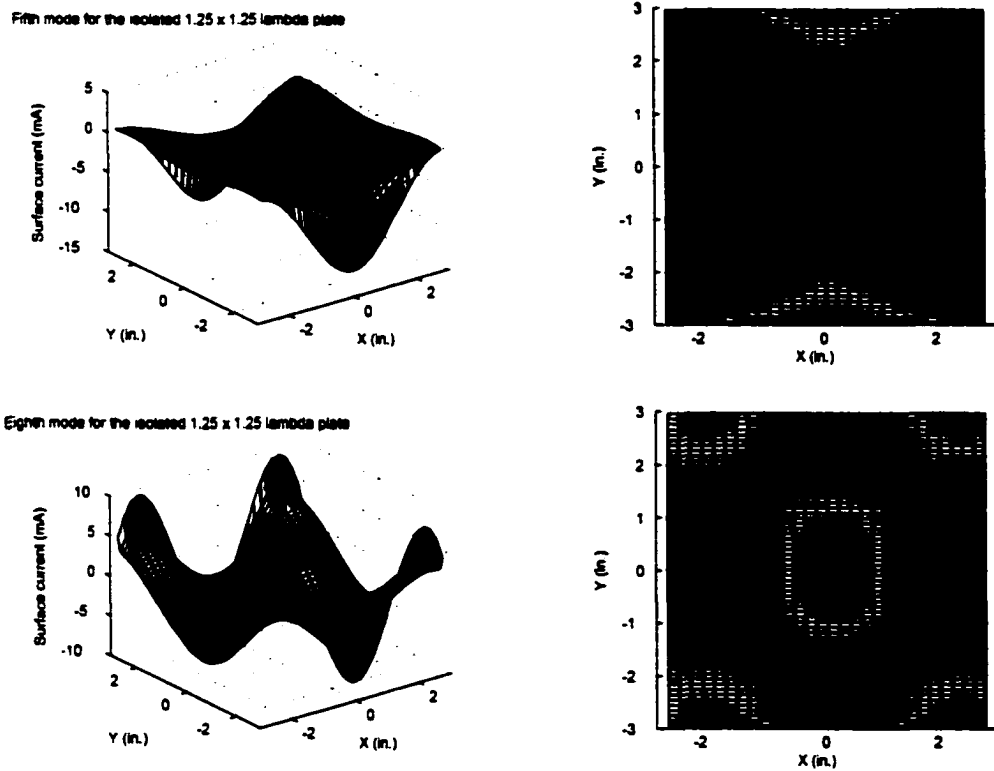


Figure 52:Oblique and overhead views of the fifth and eighth characteristic modes for the isolated 1.25λ x 1.25λ plate.

However. the localized response looks very similar to an inverted scaled image of the dominant characteristic mode for the isolated antenna. Again, the antenna portion of the system modes is a scaled version of the dominant characteristic mode for the isolated antenna.

The type of mode responses for the 0.58 λ dipole system are very similar to the type seen with the 0.42 λ dipole system and the similarity in plate and antenna portions of the system modes to those of the isolated antenna and isolated 1.25 λ x 1.25 λ plate are the same as described for the

99

0.42 $\lambda$ system.

### 4.2.2.8    Characteristic Modes vs. Antenna Height

Antenna height was the final parameter varied while observing the effect of this operation on the modes of the antenna / plate system. A 0.5$\lambda$ dipole antenna was used in all the studies and it was positioned at 0.05$\lambda$, 0.1$\lambda$, 0.25$\lambda$, 0.5$\lambda$ and 1.0$\lambda$ above the center of the 1.25$\lambda$ x 1.25$\lambda$ plate. The segment length for the antennas and the plate was 0.508 cm. The wire radius for both the plate and the antenna was 0.039764 cm and the wire spacing between elements of the plate was 0.24983 cm. The system models were created as previously described and the characteristic mode data was computed. The data for the isolated antenna and the isolated plate are the same as presented in Figures 20, 28, 29 and 30. The first three dominant modes for each system are shown in Figures 53, 54, 55, 56, 57 and 58.

100
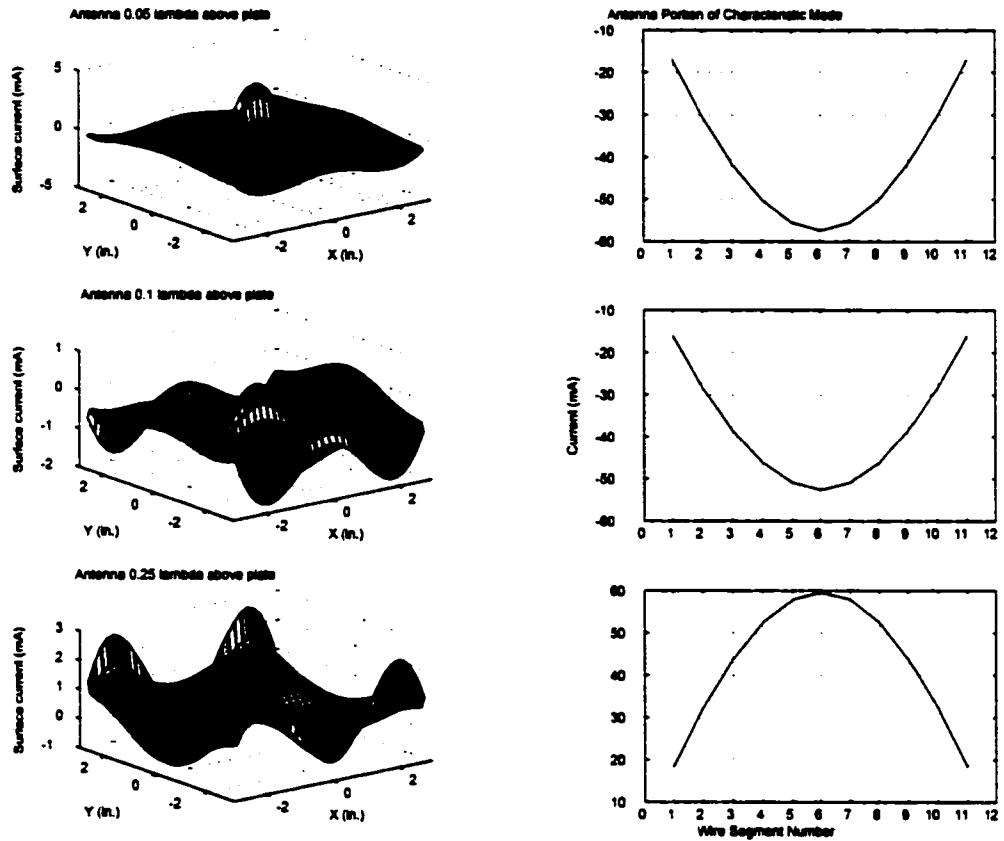
Figure 53:The plate and antenna portions of the first system mode for the antenna $0.05\lambda$, $0.1\lambda$ and $0.25\lambda$ above the plate.
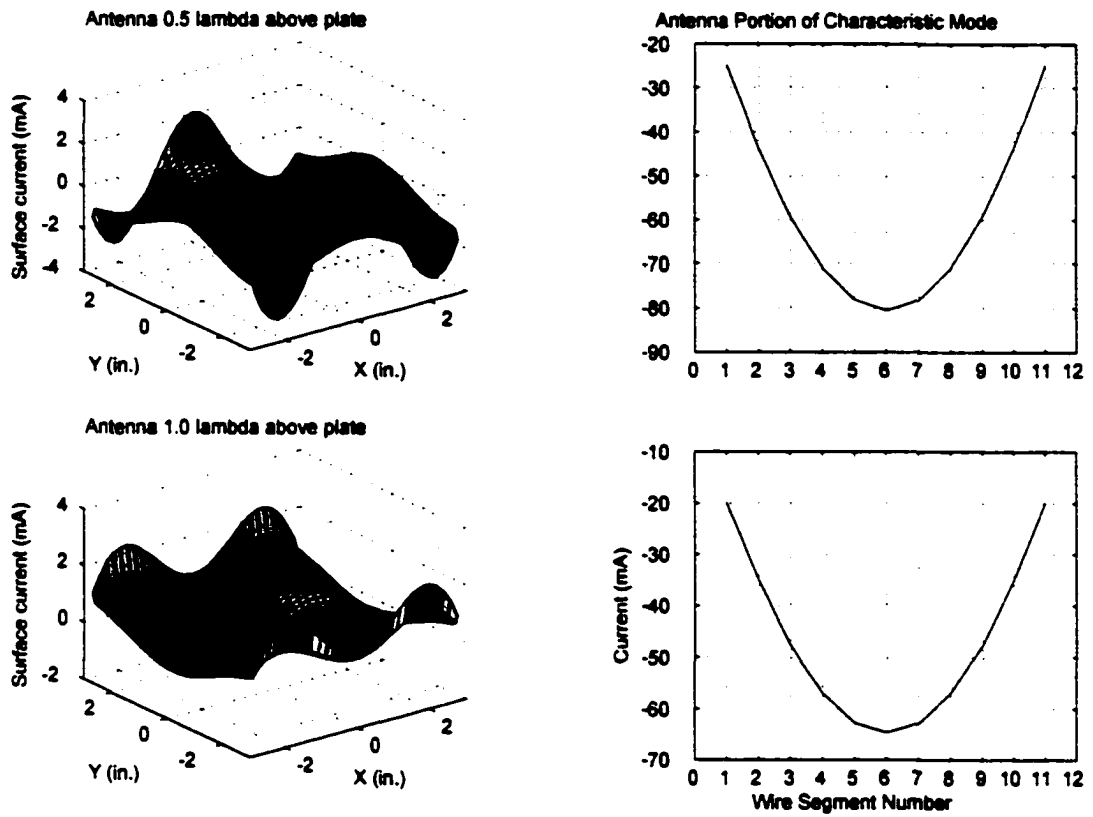
Figure 54:The plate and antenna portions of the first system mode for the antenna $0.5\lambda$ and $1.0\lambda$ above the plate.
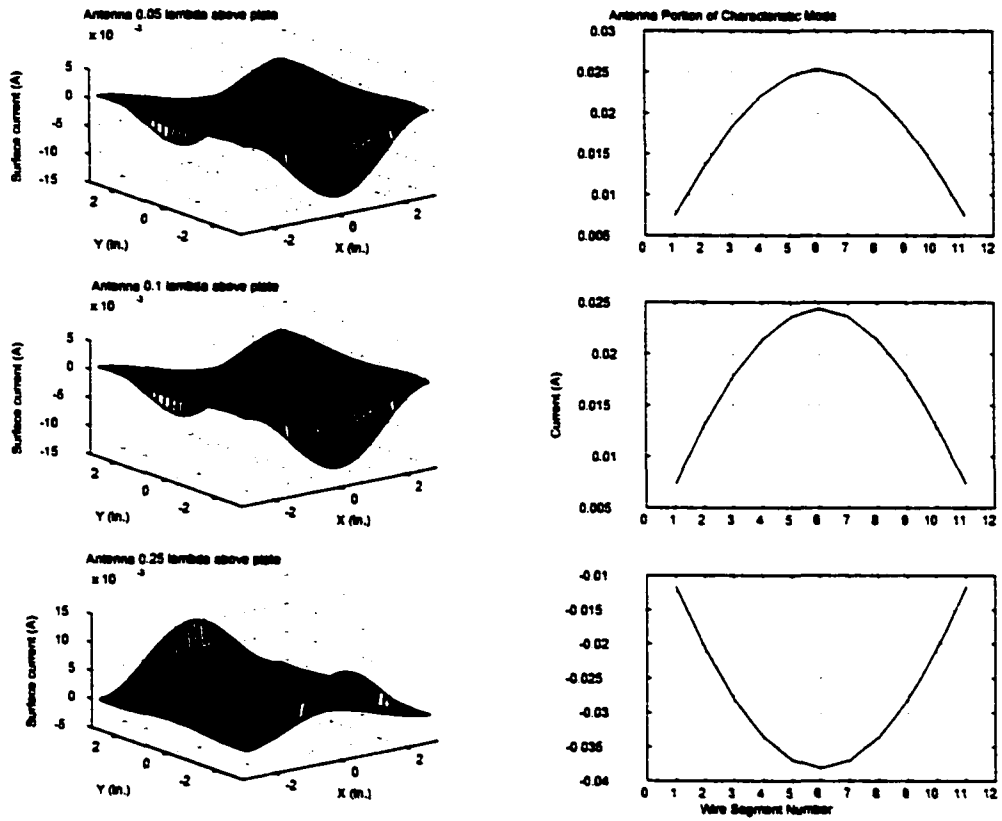
Figure 55:The plate and antenna portions of the second system mode for the antenna 0.05λ, 0.1λ and 0.25λ above the plate.

103
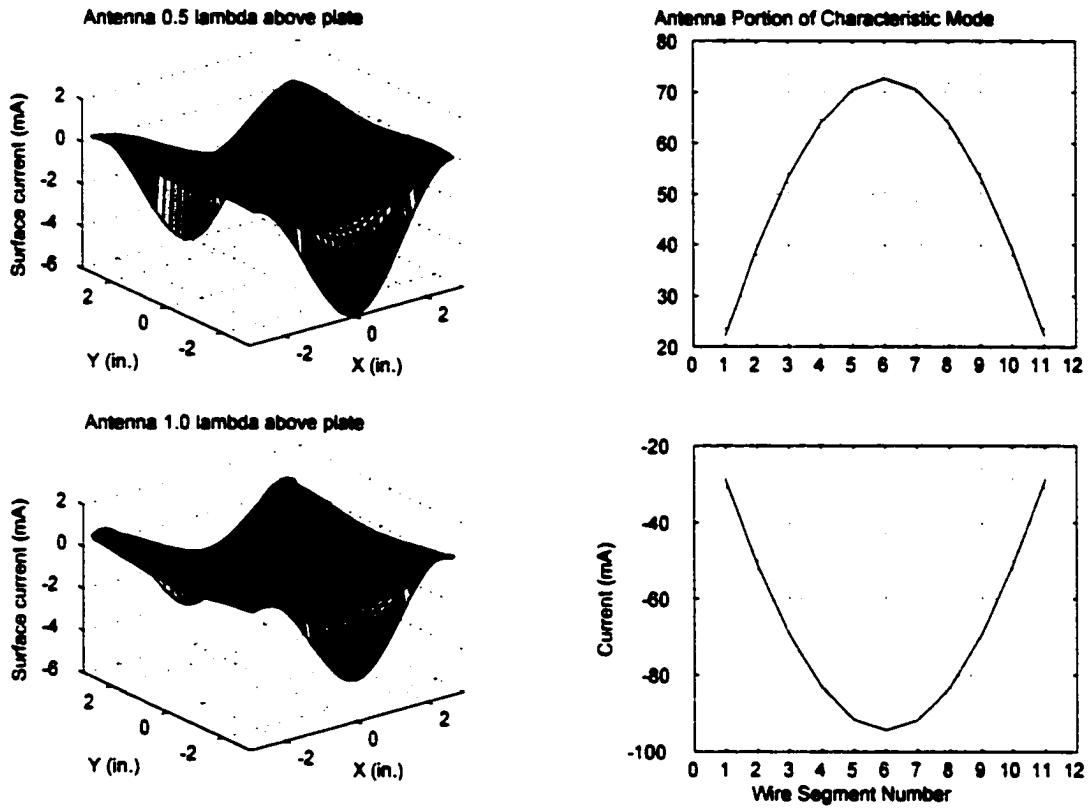
Figure 56:The plate and antenna portions of the second system mode for the antenna $0.5\lambda$ and $1.0\lambda$ above the plate.

104
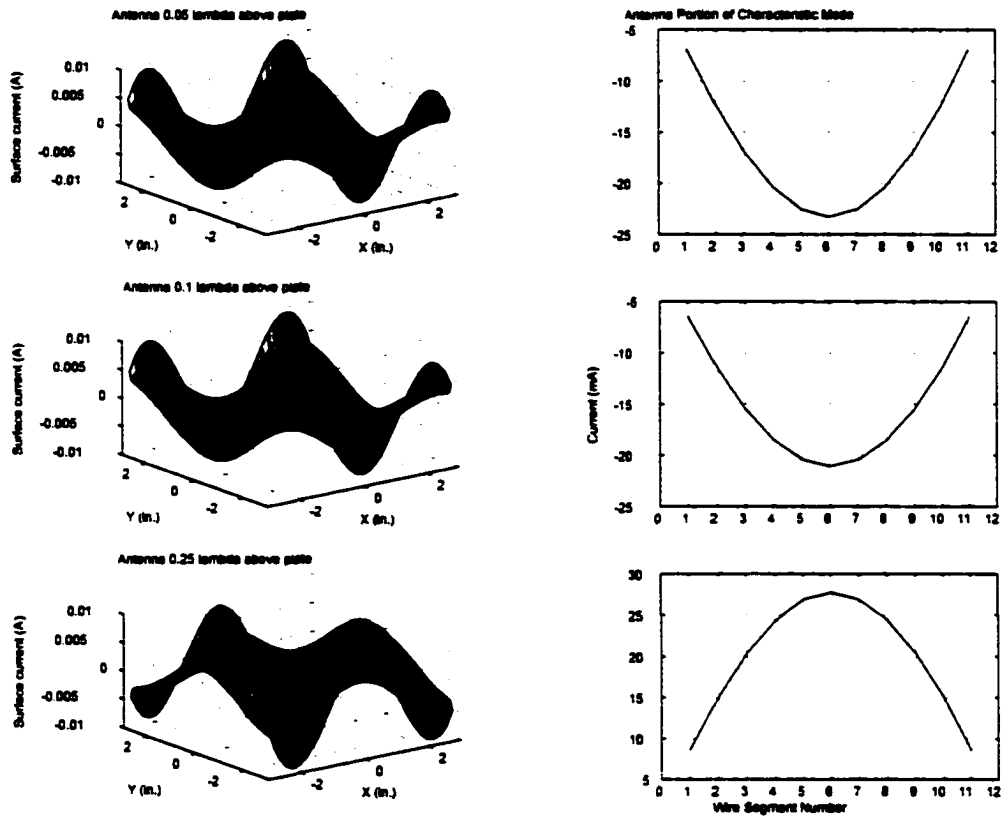
Figure 57:The plate and antenna portions of the third system mode for the antenna 0.05λ, 0.1λ and 0.25λ above the plate.

105

Figure 58:The plate and antenna portions of the third system mode for the antenna 0.5λ and 1.0λ above the plate.

### 4.2.2.9    Characteristic Mode Interpretation for Variation in Antenna Height above the Plate

The results for these systems are similar those obtained in preceding studies. The antenna portion of all responses is similar to an inverted scaled version of the dominant mode of the isolated characteristic mode, while the plate portion again looks like a weighted combination of a generalized surface effect and a localized effect. The localized effect is, as before, a scaled version of the dominant mode of the isolated characteristic mode. However, the scaling varies as the antenna is elevated off of the plate. In the case were the antenna is elevated to 0.5 λ above the plate, the

106

attenuated 'antenna image' is not visible in the generalized plate response. However, the generalized portion exhibits more range in the shape of its response for a particular mode. For the first mode, at all heights, the generalized response looks like a an attenuated version of either the first or eighth characteristic mode of the isolated plate. For the second system mode, the generalized plate response looks like an attenuated version of the fifth characteristic mode of the isolated plate. Finally, the generalized response of the third system mode looks like an attenuated version of either the fifth or the eighth characteristic mode of the isolated plate.

#### 4.2.2.10    Antenna / Plate Systems

The results of the simulations performed on the antenna / plate systems above indicate that the mutual interaction and the resulting system characteristic modes are dependent on a number of factors. These factors include the height of the antenna above the plate, the location of the antenna above the plate, the length of the antenna and the size of the plate. The system characteristic modes can be described by the portion of the response on the plate and that portion of the response on the antenna. In general the antenna portion looks very similar to the shape of the dominant mode of the isolated resonant antenna. Additionally, the plate portion can be described as having a localized shape and a general shape. The localized shape lies beneath the antenna and is an inverted, scaled version of the antenna portion of the system response. However, the general shape of the plate portion is very similar to either a flat surface or a scaled version of one of the modes of the isolated plate.

#### 4.2.2.11    Comparison of Measured and Computed Patterns

This section of the research compares E-Plane and H-plane measurements that were obtained in the lab with those patterns calculated using the characteristic mode approach and the patterns predicted

107

by the EMBPro software. Patterns were obtained for a center-fed, $0.5\lambda$ dipole located 0.254 cm above positions one and three of Figure 27. A $1.25\lambda$ x $1.25\lambda$ plate was used throughout study.

The cubes containing the antenna system and the horn antenna were positioned as depicted in Figure 19. The cubes were placed at a distance $d$ such that $d > \frac{2D^2}{\lambda}$ [23]. $D$ is the largest dimension of the radiator, which for this research was the plate. This distance, $d$, is the standard distance accepted as the near-limit of the radiation far-field. $D$ for the $1.5\lambda \times 1.5\lambda$ plate is ($\sqrt{2} \cdot 1.5\lambda$), i.e. the diagonal distance across the square plate. This gives a far-field limit beginning at approximately 1.1 meters. For these measurements, the cubes were positioned at a distance of 4 meters from each other.

The characteristic mode predictions were based on data obtained earlier in Chapter 4. Using this data, the far-field data were calculated using the algorithm in Figure 12. These data were then entered into the *pwrplt05.m* M-file and E-plane and H-plane data were calculated. EMBPro patterns were calculated using the NEC geometry descriptions. While cross-polarized and co-polarized patterns, were obtained for the measurement portion of this work only co-polarized patterns were calculated. This was based on the following reasons. First, all surface currents on the wire models are assumed to be axial in nature. The other reason is related to the parallel nature of the wires. Since the plate was approximated by wires that were parallel not only to each other, but also the antenna, a cross-polarized pattern would not exist. For the purposes of these measurements, the horn was at port one and the ASUT was at port 2. The horn was the transmitting antenna and the ASUT was the receiving antenna. This describes a $S_{21}$ measurement arrangement. The $S_{21}$ measurements are shown in Figures 59 and 60. Results computed using the characteristic mode approach are shown in Figure 61. These results can be compared with the results obtained from the EMBPro software. Position one results are shown in Figures 62 and 63 while position three results are shown in Fig-

108

ures 64, 65 and 66. Note that the results for the E and H-plane for position one and the H-plane for position three are symmetric.
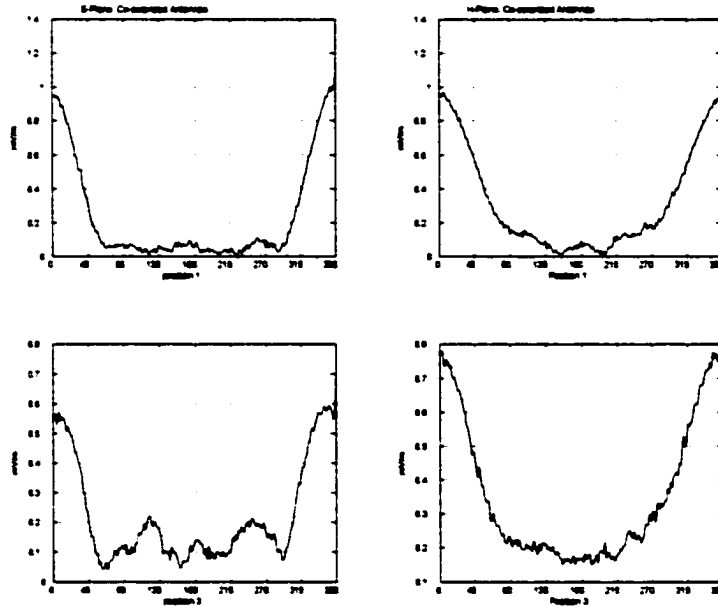


Figure 59:Co-polarized S21 E and H-plane measurements.
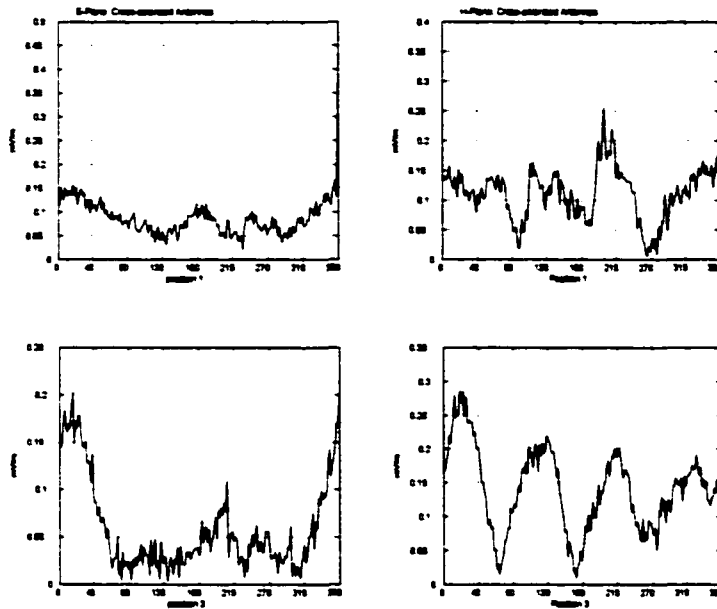
Figure 60:Cross-polarized S21 E and H-plane measurements.
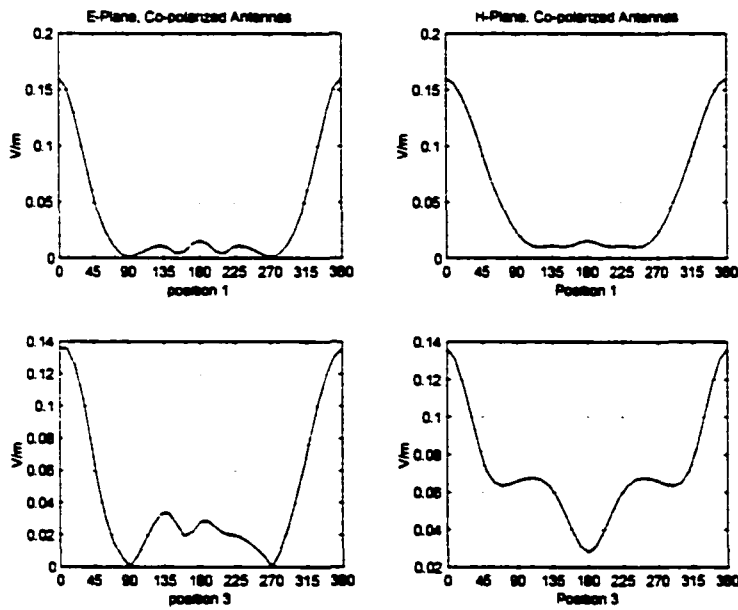
Figure 61:Computed co-polarized E and H-plane data for positions 1 and 3 using the characteristic mode approach..

110
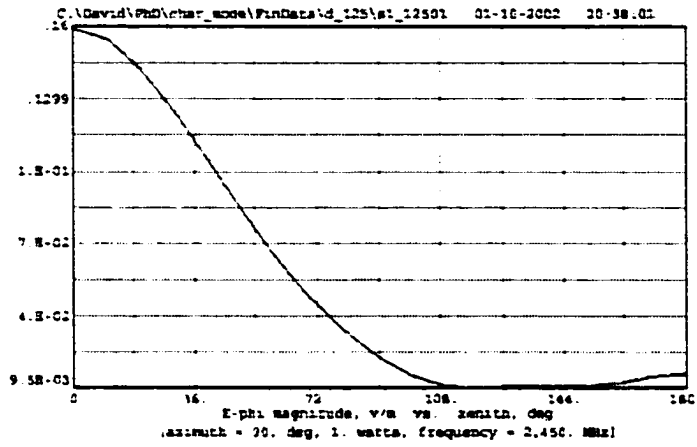
Figure 62:Calculated H-plane response for position 1.
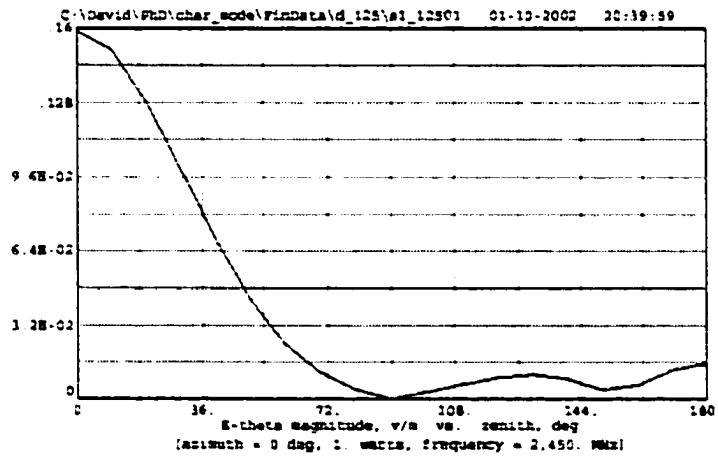


Figure 63:Calculated E-plane response for position 1.

111
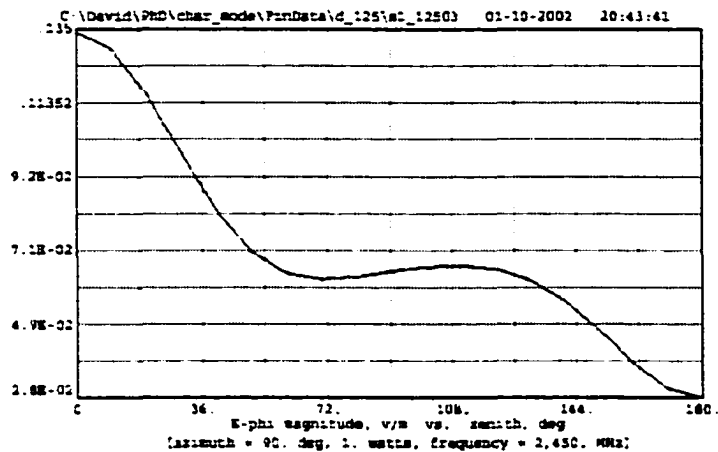
Figure 64:Calculated H-plane response for position 3.
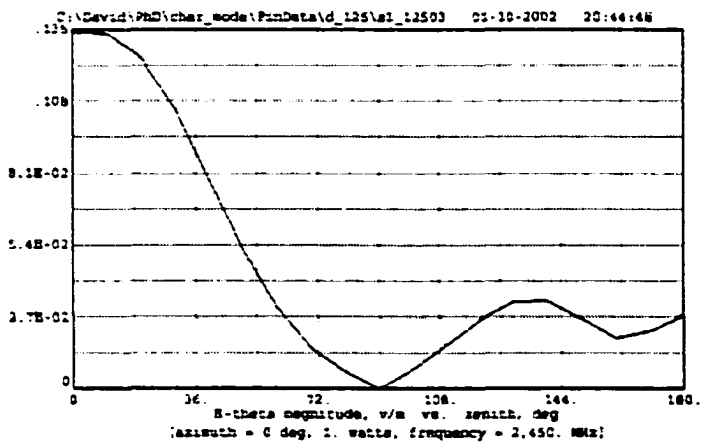


Figure 65:Left-half of the E-plane response for the antenna at position 3.

112
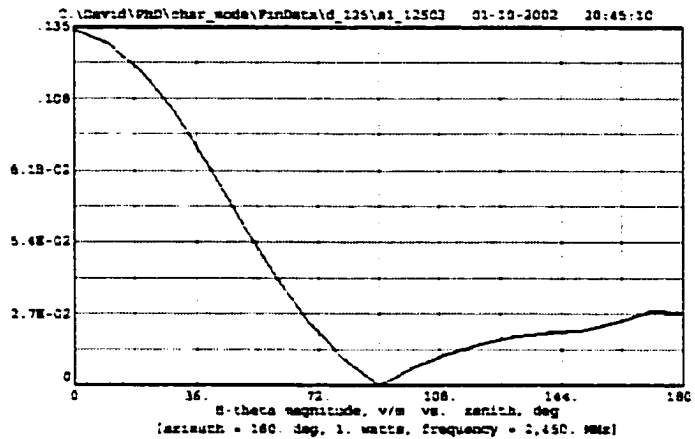
Figure 66:Right-half of the E-plane response for the antenna at position three.

Comparing the shapes Figure 59 with those of Figure 61 suggests that there is reasonable qualitative agreement between the measured data and calculated pattern for position 1; pattern trends are very similar. The difference in magnitude can be attributed to a scaling factor that was not determined for these calculations. However, there is considerable qualitative discrepancy between the measured pattern for position 3 and the calculated data for position 3. Such a large discrepancy is most likely attributed to the fact that the simulated results were based on a parallel wire model of the plate. This type of model does not support any currents perpendicular to the axes of the wires. Such currents become very significant near the edge of the plate when the antenna approaches this region, as is the case for position 3. Additionally, the lack of a fully gridded wire model of the plate precluded the calculation of the contribution to the radiation pattern from cross-polarized antenna components.

### 4.2.2.12    Mode Contribution

Another issue of interest in this research is the relationship between the number of characteristic

113

modes used to calculate a far-field radiation pattern and the accuracy of the approximate pattern obtained. Characteristic mode data obtained from the dipole antenna suggests that only a single characteristic mode, or very few of them, are needed to calculate a reasonable approximation of the far-field radiation pattern. This begs the question, "How many modes are needed for a simple system to reasonably approximate the actual radiation pattern?"

The data obtained here approximates the E-Plane and H-plane patterns using an increasing number (from one to five) of dominant modes of a system. A system consisting of a center-fed, $0.5\lambda$ dipole mounted 0.254 cm above the center of the $1.25\lambda$ x $1.25\lambda$ plate was studied. The patterns obtained are shown in Figures 67 and 68.
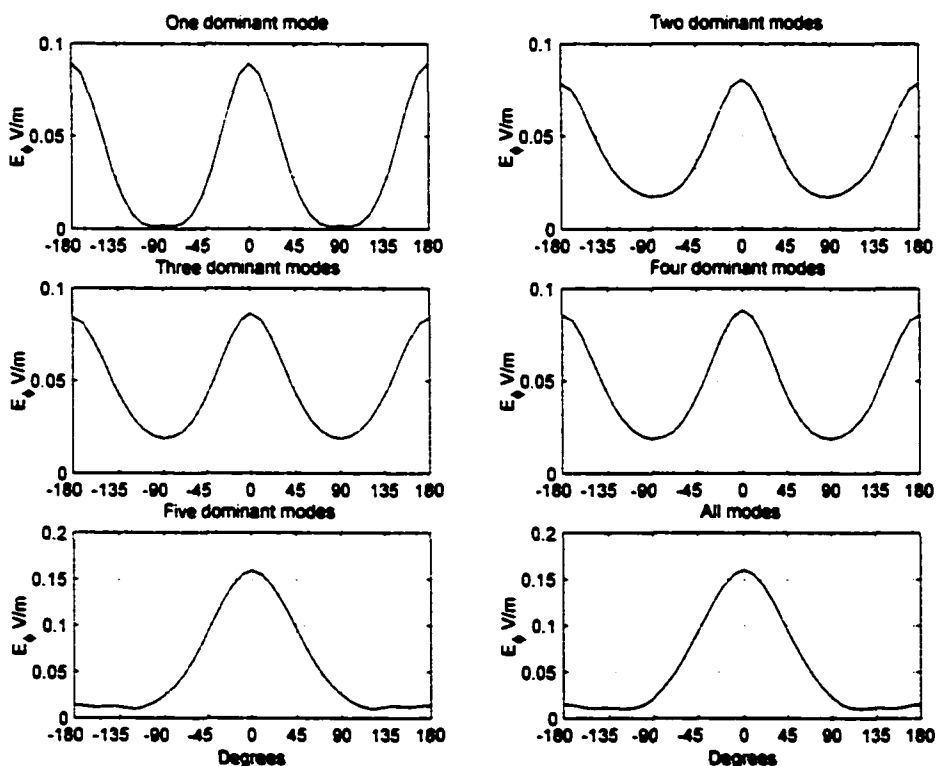


Figure 67:H-plane patterns that result from using the contributions of one to all of the characteristic modes.
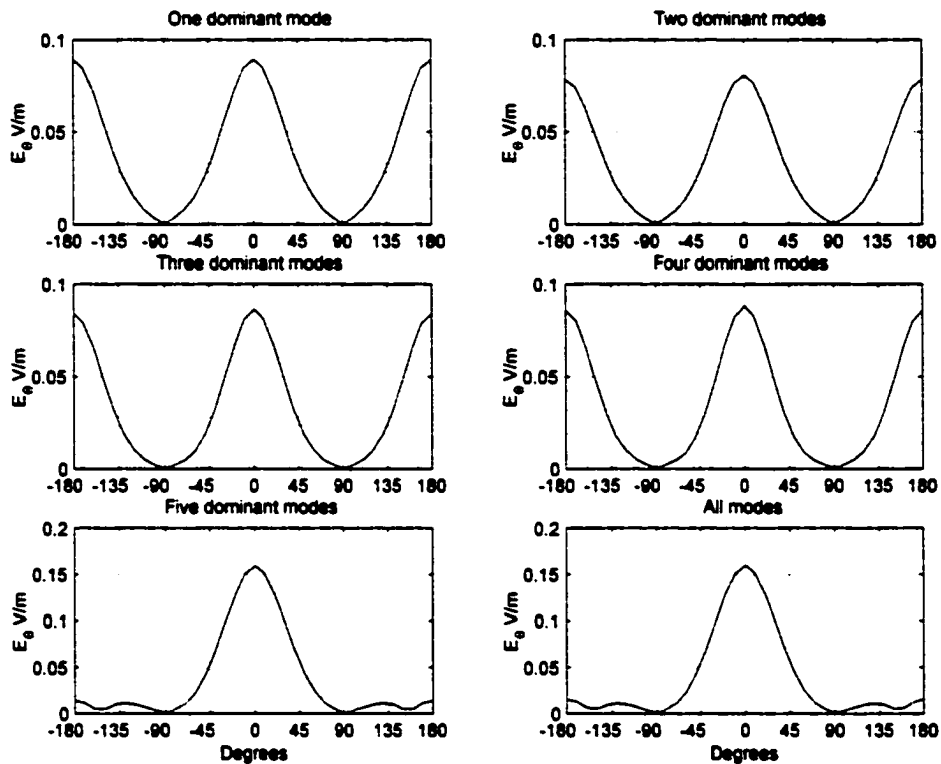
Figure 68:E-plane patterns that result from using the contributions of one to all of the characteristic modes.

One of the features of the characteristic modes approach is that it enables approximation of the surface current density (and as a result, the far-field radiation pattern) by use of a weighted sum of characteristic modes. As discussed earlier, the current distribution for a center-fed half-wavelength dipole can be approximated by a single characteristic mode, the dominant mode of the dipole. The number of modes necessary to approximate the far-field radiation pattern accurately was determined from the results of Figures 67 and 68 to be no less than five modes for this example. Using this number of modes leads to a reasonable approximation of the far-field pattern. These results suggest that even for relatively simple geometries, i.e. plates, several modes may be necessary in order to reasonably model the far-field radiation pattern.

115

Additionally, the determination of those modes that should be included in the list of required nodes is dependent on two factors: the magnitude of the associated eigenvalue and the *modal excitation factor* as defined in Chapter 2. Even though a mode may have an eigenvalue with magnitude that is much less than one, it does not mean this mode will contribute significantly to the radiation pattern. For example, if the probe or feedpoint lies at a null or zero-point of this mode, then it will have a modal excitation factor of zero and no power is radiated. An example of this is seen in the dipole antenna. Because the characteristic mode associated with the second smallest eigenvalue has a null at the location of the antenna feedpoint (Figure 2) this mode does not contribute to the radiated pattern.

### 4.2.2.13 Comparison of Computational Methods for Pattern Calculation

The final section of the experimental work investigates various approaches that have been suggested as ways to model (or approximate ) antenna placement within a system of variable geometry operating in the near-resonant range. The radiation patterns, E-plane and H-plane, of several antenna / plate systems were calculated using three different approaches.

The first approach calculated the patterns using a superposition of patterns obtained from the characteristic mode analysis of the isolated antenna and the isolated plate. The antenna was probed in the center and the plate was fed 180 degrees out of phase, with respect to the antenna feed, at a point on the plate that would be directly below the superimposed antenna pattern origin. A spatial phase term was incorporated based on their relative distance from each other. The second approach calculated the patterns using the data obtained from the characteristic mode analysis of the combined antenna / plate system. In both of these approaches, all the characteristic modes were used and the method for calculating the antenna pattern was described in Chapter 3 and outlined in Figure 12. The method of images was the final method used for approximating the far-field pattern.

116

In this approach, the pattern of the system was approximated by modeling the dipole antenna 0.254 cm above an infinite perfectly electrically conducting plane. These three approaches were applied to systems composed of a 0.5λ dipole positioned 0.254 cm above each of the six positions on each of the three plates previously described.

The results of these three approaches are shown in the Figures 69 - 74.
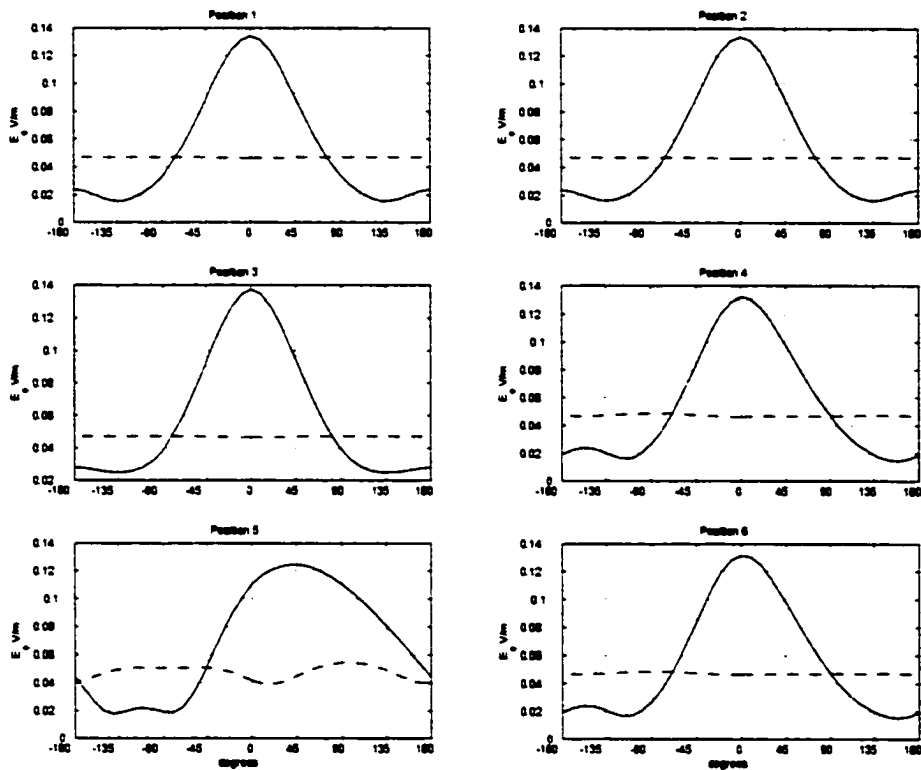


Figure 69:H-plane patterns using superposition (dashed plot) and characteristic mode approaches. Plate size is 0.75λ x 0.75λ.

117
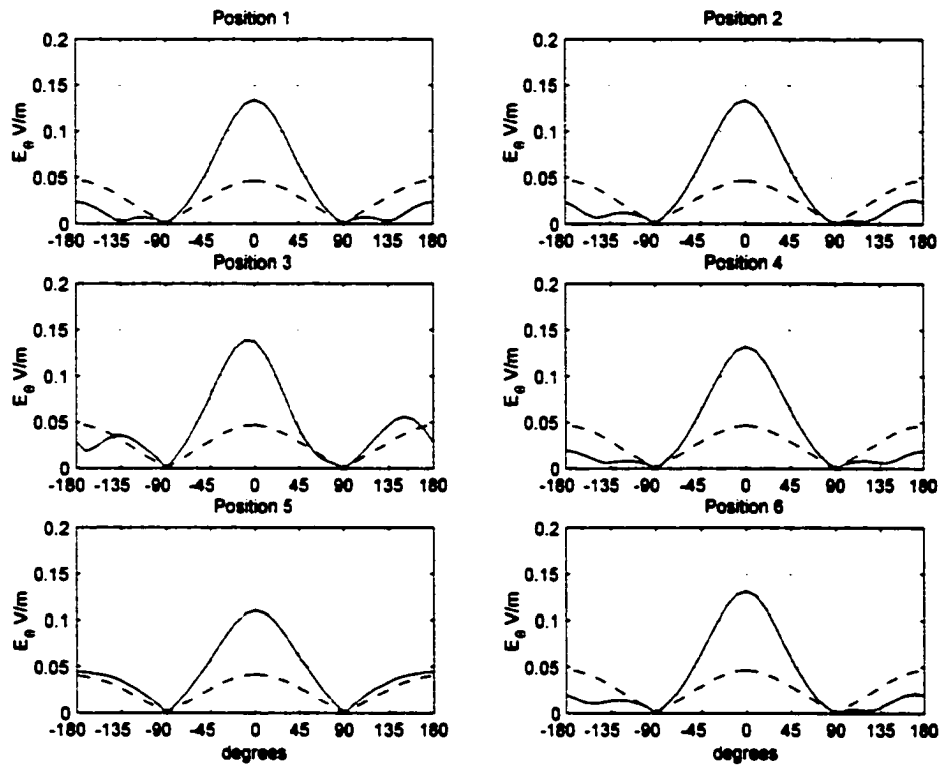
Figure 70:E-plane patterns using superposition (dashed plot) and characteristic mode approaches. Plate size is $0.75\lambda$ x $0.75\lambda$.

118
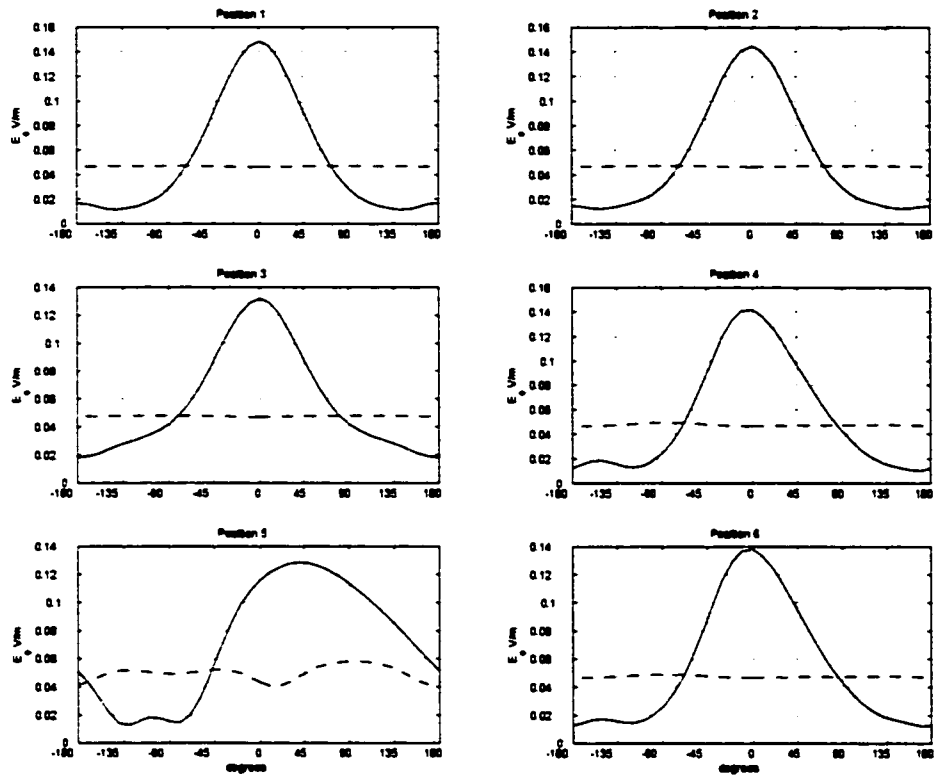
Figure 71:H-plane patterns using superposition (dashed plot) and characteristic mode approaches. Plate size is $1.0\lambda$ x $1.0\lambda$.

119
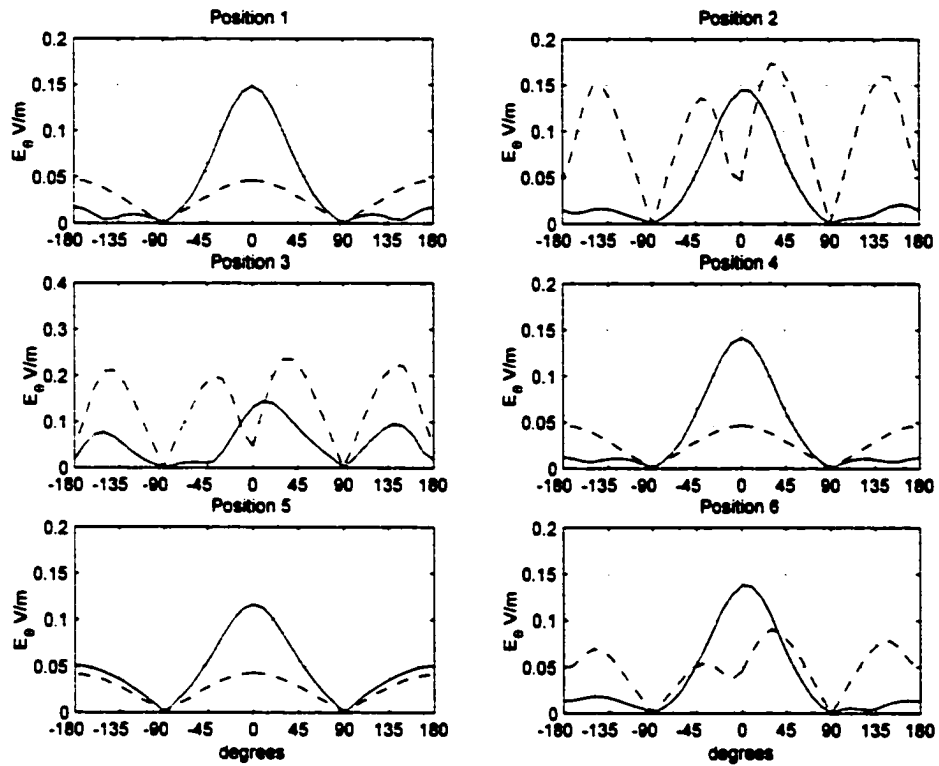
Figure 72:E-plane patterns using superposition (dashed plot) and characteristic mode approaches. Plate size is 1.0λ x 1.0λ.

120
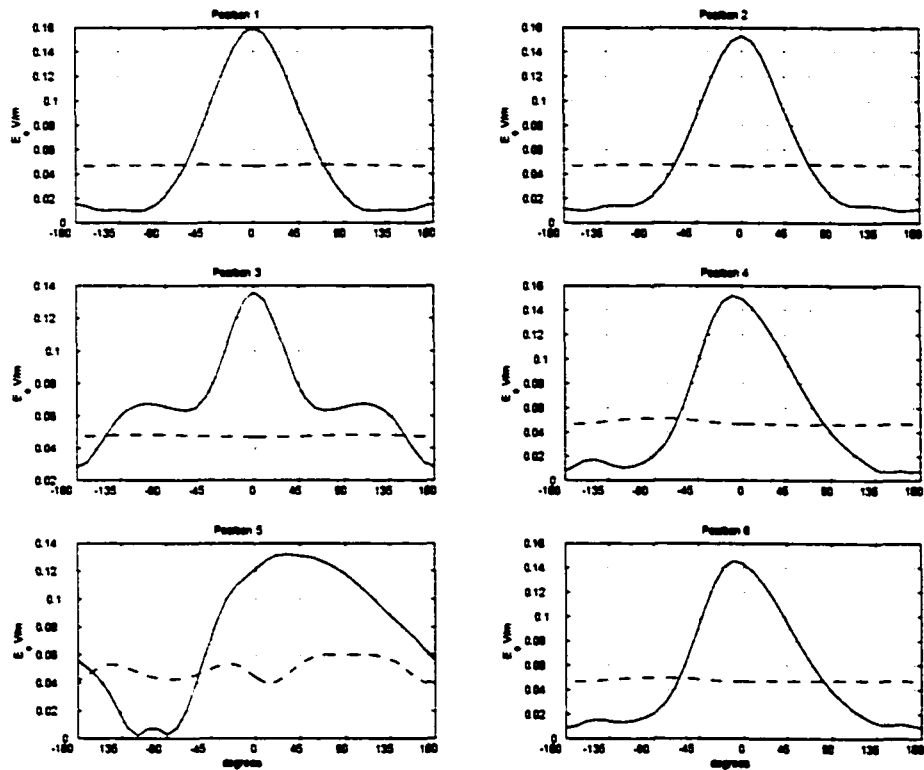
Figure 73:H-plane patterns using superposition (dashed plot) and characteristic mode approaches. Plate size is 1.25λ x 1.25λ.

121
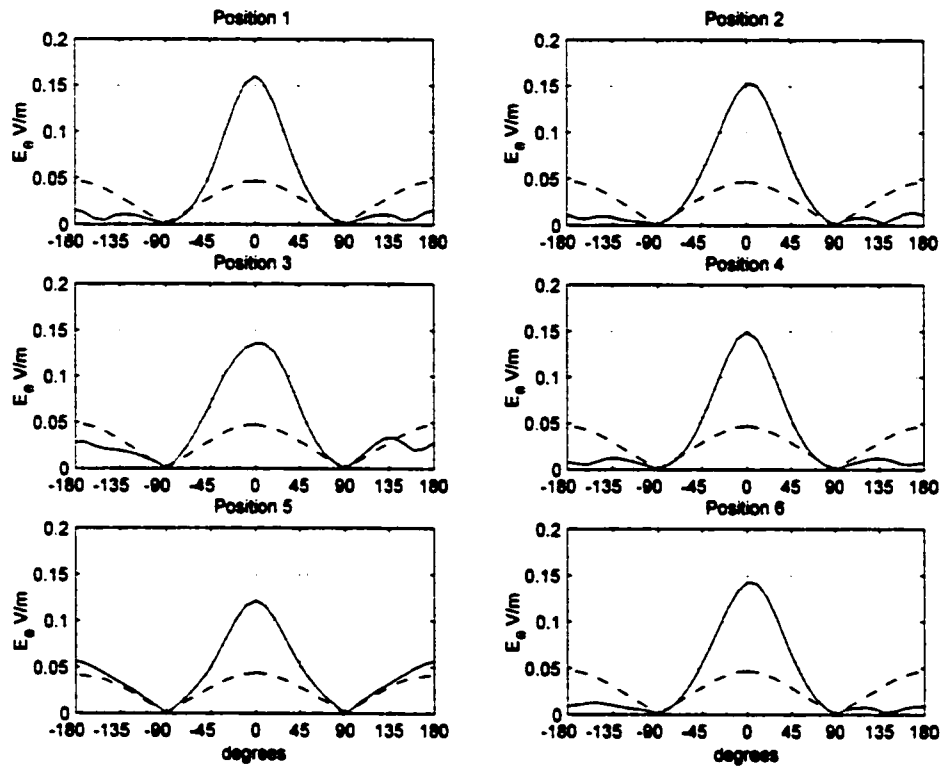
Figure 74:E-plane patterns using superposition (dashed plot) and characteristic mode approaches. Plate size is 1.25λ x 1.25λ.

Figure 75 illustrates the results of the method of images approximation. There is only one plot for all positions, because this approach assumes an infinite plate.

122
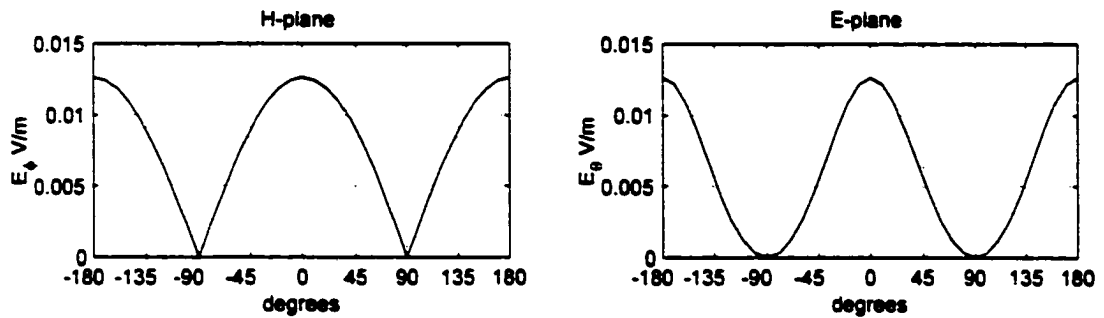
Figure 75:E-plane and H-plane results for the method of images approximation of a dipole 0.254 cm above an infinite ground plane..

Results from a comparison of the radiation patterns demonstrates how simplifications such as a simple superposition approach and the method of images are significantly less accurate in their ability to predict the radiation pattern of even these relatively simple systems. A more accurate approximation would be a superposition of radiation patterns from the isolated antenna and an isolated plate that is probed in a number of locations, thereby reflecting the diffuse interaction imparted by the mutual impedance with the antenna positioned above the plate. This suggests that the electromagnetic interaction or coupling between the antenna and the non-driven object, the plate in this example, is significant and needs to be considered when predicting radiation patterns of systems of near-resonant structures. This precludes the use of such simplifications as the method of images or merely adding the radiation patterns of the isolated structures that comprise the system. The coupling effect is further manifested in the changes that take place in the shapes of the plate portions of the system characteristic mode response.

123

# Chapter 5
# CONCLUSION

Previously, characteristic mode analysis had only been applied to systems with constant geometry that operated in the near-resonant range and the system had constant characteristic modes independent of the probe location. In this research, we investigate variable antenna placement in systems operating in the near-resonant frequency range where the antenna and wireless device are both comparable in size to a wavelength. For the analysis of such a system, we have used the characteristic mode approach to study the electromagnetic interaction between the antenna and the wireless device. To achieve this, new characteristic mode software was developed and a number of dynamic systems composed of a driven dipole antenna positioned close to either a wire or planar arrangement of parallel wires, simulating the antenna / wireless device system, were studied. Both computational and experimental results were obtained. The results clearly demonstrate, that as expected, the dominant system characteristic modes are dependent upon antenna position due to the interaction between the antenna and the device.

The array representing the characteristic modes of the system can be split into two sub-arrays: one representing the antenna portion and the other array representing the device portion of the mode. These were plotted and one can note the similarity between the shape of the antenna portion with the shape of the dominant modes of the isolated antenna. Additionally, certain aspects of the shape of the device portion were similar to the shape of the dominant modes of the isolated device and the isolated antenna. Further division of the device portion into a general response region and a local response region improved our understanding of the similarity between the dominant modes of the isolated antenna and device with those regions of the device portion of the system response.

124

This analysis indicates that in systems with variable antenna placement, the system characteristic modes are not simple sums of the characteristic modes of the isolated device and antenna. Instead, there is a more complex relationship between the shape of the antenna portion and the device portion of the system characteristic modes with the antenna position, antenna geometry and the device geometry. This relationship can be approximated by equations 84, 85, 86, 87, and 88. In these equations, the dominant system characteristic modes are written as a linear superposition of the modes of the isolated antenna and those of the isolated device where the coefficients are functions of the antenna position.

The device portion of the system characteristic mode, $CM_{Device}$ can be approximated by

$$CM_{Device} \approx \beta(CM_{Isolated\_Antenna}) + \gamma(CM_{Isolated\_Device}), \qquad (84)$$

where

$$\beta = f_1(Antenna\ Position), \qquad (85)$$

$$\gamma = f_2(Antenna\ Position), \qquad (86)$$

$CM_{Isolated\_Antenna}$ represents the characteristic modes of the isolated antenna, $CM_{Isolated\_Device}$ represents the characteristic modes of the isolated device and $f_1$ and $f_2$ represent functions yet to determined. Additionally, the dominant modes of the antenna portion of the system, $CM_{Antenna}$, are scaled images of the dominant mode of the isolated antenna, as represented by

$$CM_{Antenna} \approx \zeta(CM_{Isolated\_Antenna}), \qquad (87)$$

where

$$\zeta = f_3(Antenna\ Position), \qquad (88)$$

and $f_3$ represents a yet to determined function. While the functions $f_1$, $f_2$, and $f_3$ are as yet

125

unknown, results from this research demonstrate that the antenna-device coupling mostly impacts the plate portion of the system characteristic mode and has little impact on the antenna. The antenna portion of the system characteristic mode remains a scaled version of the dominant mode of the isolated antenna.

Therefore. knowledge of the characteristic modes of the isolated antenna and device and the functions $f_1$, $f_2$, and $f_3$ could be used to predict the behavior of the system characteristic mode responses as the antenna is repositioned within the system. However, further investigation is needed to identify the exact nature of the functions relating antenna position to $\beta$, $\gamma$, and $\zeta$. Initial studies lead us to believe that these functions are dependent on certain relationships, such as distance from antenna center to the edge of the device and to the device center and the relative positions of the extrema of the dominant modes of the isolated antenna and device as the antenna is repositioned above the plate. Generalizing the functions $f_1$, $f_2$, $f_3$, $\beta$, $\gamma$, and $\zeta$ to more complex devices than those studied, and combining this with knowledge of the dominant characteristic modes of the isolated antenna and the device, would enable prediction of the dominant modes of such complex systems as a function of the proposed antenna positions.

In conclusion. this work establishes the foundation for the development of an antenna placement algorithm for systems operating in the near-resonant range with variable antenna placement by examining the relationship between antenna position and the variation of the system characteristic modes.

## 5.1  Future Work

The future work on this project would be directed first at improving the existing method of moments software or writing new software. This will be done to address the geometry constraints

126

such as segment length and the simplification of only using parallel wires rather than a rectangular mesh grid to model surfaces. New software would allow the creation of fully-meshed wire grids that provide symmetric impedance matrices. This would enable the study of more complex structures. Once the new code is written, more complex structures and antennas such as patches and monopoles could be examined.

As knowledge is gained about more complex structures, it would be incorporated into our evolving knowledge of how characteristic modes change with respect to dynamic system geometries operating in the near-resonant range. Such knowledge could eventually be condensed into functional relationships for use in a predictive paradigm for antenna placement.

127

# Appendix A

## A.1  Maxwell's Equations and Boundary Conditions

Maxwell's equations and boundary conditions are reviewed to orient the reader to the electromagnetic environment at the interface between two regions. This interface is of particular importance to many electromagnetic problems. Additionally, a study of the boundary conditions between a structure and the surrounding region forms the basis for the development of the initial equations relating the electric fields, both impressed and scattered, with the surface currents existing on a structure. Once described, the boundary conditions were used as a necessary first step in developing the MoM approach and ultimately the characteristic mode approach.

## A.2  Maxwell's Equations

Maxwell's equations are a compact set of vector equations that describe the relationship between time-varying electromagnetic fields and sources. These equations can be written in either differential or integral form and are valid for all regions of space. Additionally, proper application of these equations at the interface between two regions leads to the development of boundary conditions.

The differential form of Maxwell's equations are shown in the following equations:

$$\nabla \times \overline{E} = -\frac{\partial \overline{B}}{\partial t},$$

$$\nabla \times \overline{H} = \overline{J} + \frac{\partial \overline{D}}{\partial t},$$

$$\nabla \bullet \overline{B} = 0,$$

and

$$\nabla \bullet \overline{D} = \rho$$

128

where $\overline{E}$ is the electric field strength, $\overline{B}$ is the magnetic flux density, $\overline{H}$ is the magnetic field strength, $\overline{J}$ is the electric current density, $\overline{D}$ is the electric flux density, and $\rho$ is the electric charge density. While the point form is relatively useful for relating the interaction and coupling between the electric and magnetic fields, they are not as useful for determining boundary conditions. Determination of the boundary conditions requires the use of the integral form of Maxwell's equations. This approach will be developed in the next section.

## A.3 Boundary Conditions

As stated above, boundary conditions are derived by application of Maxwell's equations to the boundary between two regions, $R_1$ and $R_2$, of material that have parameters $\varepsilon_1, \mu_1, \sigma_1$ and $\varepsilon_2, \mu_2, \sigma_2$ respectively. These conditions simplify the calculation of values for various electromagnetic quantities at the boundary. As a result, boundary conditions are an important step in obtaining the electromagnetic fields that exist both at the boundary and at an arbitrary distance from the boundary. The boundary conditions will be addressed in the following order. First, the tangential $E$ and $H$ field boundary condition will be calculated. The normal magnetic and electric fields conditions will then be calculated.

It is important to keep in mind that once the boundary conditions are obtained, they do not express the value of the field. Instead, they describe the physical and mathematical conditions that must be satisfied at the boundary. They are refinements of the more general set of electromagnetic equations, Maxwell's equations. The boundary conditions are simplifications of Maxwell's equations as they are applied at the interface of two regions.

### A.3.1 Tangential Electric Field

Formulation of the tangential electric field boundary condition begins by application of Stokes

theorem to the differential form of Faraday's law. This results in the integral form of Faraday's law as expressed in Equation 89

$$\oint \mathbf{E} \cdot dl = -\frac{\partial}{\partial t} \iint_{S_0} \mathbf{B} \cdot ds \qquad (89)$$

where $S_0$ is the surface enclosed by the contour integral that integrates $\mathbf{E}$. The closed contour for the integral on the left side of the equation is shown in Figure 76.
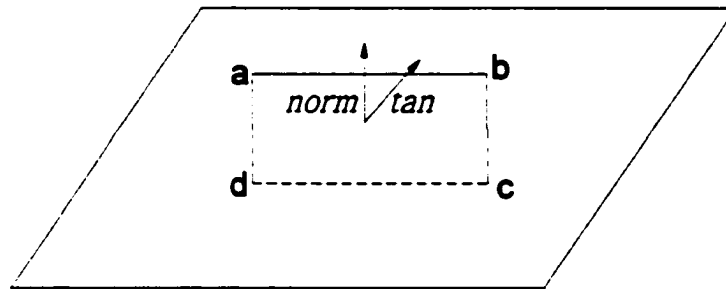


Figure 76:Contour for integral of tangential E-field and integral of the tangential H-field.

The contour integral path is composed of segments "a,b", "b,c", "c,d" and "d,a". The orientation of the electric and magnetic fields are shown at the boundary surface. Now consider the left-hand side integral from Equation 89 and break the path of integration into the four segments described above. Now let all the segments of the integral approach zero with segments "b,c" and "d,a" approaching more quickly. As this happens, the surface circumscribed by the four segments approaches zero also. Therefore, Equation 89 can be rewritten as

$$\int_{\,\check{a},b\check{}} \mathbf{E}_{1_{tan}} \cdot dl - \int_{\,\check{c},d\check{}} \mathbf{E}_{2_{tan}} \cdot dl = 0 . \qquad (90)$$

Stated more simply, only the electric field parallel to the segments "a,b" and "c,d" contributes to the contour integral. Since the segment lengths are the same, the following simplification must

130

be true for the equation to hold,

$$E_{1_{tan}} = E_{2_{tan}}.$$

This expression can be written in terms of the more generic vector equation as

$$\hat{n} \times (E_1 - E_2) = 0 \tag{91}$$

where $\hat{n}$ is defined as the unit vector normal to the boundary. Equation 91 illustrates that the tangential electric field is continuous across the boundary.

## A.3.2   Tangential Magnetic Field

A similar argument will be used to determine the boundary condition for the tangential magnetic field. The development begins with Ampere's law,

$$\nabla \times H = J + \frac{\partial D}{\partial t}. \tag{92}$$

Stokes theorem is again applied to Equation 92. This results in

$$\oint H \cdot dl = \iint_{S_0} J \cdot ds + \frac{\partial}{\partial t} \iint_{S_0} D \cdot ds. \tag{93}$$

A simplification process similar to that performed for Equation 89 is applied to Equation 93, and the geometry of Figure 76 is used. As the area bounded by the contour integral approaches zero, so too does the contribution of $\frac{\partial}{\partial t} \iint_{S_0} D \cdot ds$ from Equation 93. This assumes that $D$ is a finite-valued field. Additionally, if the surface of the boundary has zero conductivity, then $J$ will be zero. This makes sense because there will be no mobile charges in the material. If the surface has finite conductivity, then $J$ will be finite. Therefore, the integral of $J$ over the surface, $S_0$, approaches zero as the surface gets smaller.

If the segments "b,c" and "d,a" are allowed to approach zero much faster than segments "a,b" and "c,d" then the following simplification is true.

$$\int_{"a,b"} H_{1_{tan}} \cdot dl - \int_{"c,d"} H_{2_{tan}} \cdot dl = 0 \tag{94}$$

131

Since the path of integration for $H_1$ and $H_2$ is the same, then $H_{1_{tan}} = H_{2_{tan}}$. This expression can then be rewritten in vector form as

$$\hat{n} \times (H_1 - H_2) = 0. \tag{95}$$

This expression demonstrates that the tangential components of magnetic field are equal at the boundary.

If one of the materials that forms the boundary is a PEC, then Equation 93 does not reduce to Equation 94. Instead, the current exists only on the surface of the conductor. As a result, as the "b" and "d" segments approach zero, the surface current density remains constant since the current exists along the surface of the conductor (which has zero height). This is alternatively expressed as

$$J = \delta h J_v \, |_{\delta h \to 0} \, .$$

This suggests that $J_v$ goes to infinity or the volume current can be infinite to support the resultant surface current density. Recall that a perfect electrical conductor has infinite conductivity. Therefore, even if the current exists on the surface, in zero height, it has a non-zero value. Therefore, as "b" and "d" approach zero, the surface $S_0$ approaches zero, yet $J$ remains non-zero. Also, a time-varying magnetic field does not exist in the conductor. thus, $H_2 = 0$. Incorporating this result into Equation 93 results in

$$\hat{n} \times H_1 = J. \tag{96}$$

This equation states that the tangential magnetic field on the surface of the conductor is equal to the surface current density generated on the surface of the conductor. Having developed the boundary condition equations for the tangential electric and magnetic fields, the normal boundary conditions for the two fields will be developed.

132

## A.3.3 Normal Electric Field

The boundary conditions for the normal electric and magnetic fields will be based on the integral forms of the electric and magnetic Gauss laws. Development of the boundary condition for the normal electric field begins with the electric Gauss law,

$$\nabla \cdot \mathbf{D} = \rho. \tag{97}$$

Application of the divergence theorem to this equation results in

$$\oint_{S_0} \mathbf{D} \cdot d\mathbf{s} = \iiint_{v_0} \rho_v dv. \tag{98}$$

This equation is then applied for the conditions illustrated in Figure 77.
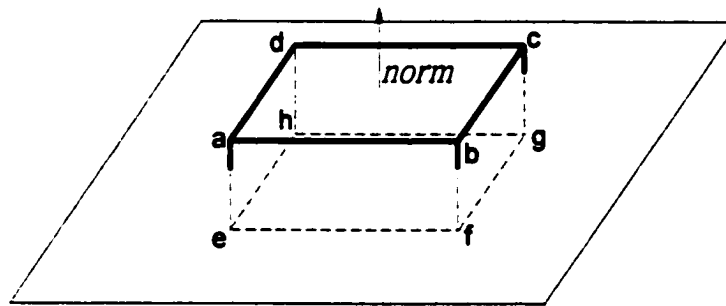
Figure 77:Geometry used for determining normal boundary conditions.

The outline of the "pillbox" represents the volume enclosed by the integral on the right-hand side of Equation 98, while the left-hand side of the equation integrates across the surface of the "pillbox."

Referring to Equation 98, assume that the height of the "pillbox" decreases faster than the area of the top or bottom surface. As a result, the volume of the box approaches zero while the top and

133

bottom surfaces of the "pillbox" are still present. Incorporating this into Equation 98 yields

$$\iint_{s_t} \mathbf{D}_1 \cdot ds - \iint_{s_b} \mathbf{D}_2 \cdot ds = \iint_{s} \rho_s ds. \tag{99}$$

Therefore, the only charge density that has any significant contribution is from the surface charge, $\rho_s$, if it exists. The integral on the right side of Equation 99 is equal to zero if a surface charge does not exist. If that is the case, Equation 99 reduces to the expression

$$\hat{n} \cdot (\mathbf{D}_1 - \mathbf{D}_2) = 0. \tag{100}$$

For the case of a perfect electric conductor, a surface charge can exist and electric fields do not exist within region 2. If a small section of the surface is observed such that $\mathbf{D}$ and $\rho_s$ are uniform, then the simplification,

$$\hat{n} \cdot \mathbf{D}_1 = \rho_s, \tag{101}$$

can be made.

In other words, the normal electric field at a point is equal to the surface charge located at that point.

## A.3.4 Normal Magnetic Field

The development of the normal magnetic field boundary condition is very similar to the development of the normal electric field boundary condition. Here the magnetic Gauss law in point form is used as the basis of development.

$$\nabla \cdot \mathbf{B} = 0 \tag{102}$$

Application of the divergence theorem to Equation 102 results in

$$\oint_{S_0} \mathbf{B} \cdot ds = 0. \tag{103}$$

The surface integral of Equation 103 refers to the surface of the "pillbox" in Figure 77. As before, the height of the pillbox is reduced much more quickly than the area of the top or bottom

134

surface. As a result, the contribution to the integral from the side of the pillbox approaches zero while the contribution of the top and bottom surfaces of the pillbox remain appreciable. This simplification is expressed as

$$\iint_{s_t} \mathbf{B}_1 \cdot ds - \iint_{s_b} \mathbf{B}_2 \cdot ds = 0. \tag{104}$$

This equation can written in vector form as

$$\hat{n} \cdot (\mathbf{B}_1 - \mathbf{B}_2) = 0. \tag{105}$$

This equation states that the normal portion of the $\mathbf{B}$ vector is continuous at the boundary between the two regions.

In the case where one of the regions is a PEC, no time-varying magnetic field exists in the region. If a time-varying electric field cannot exist in the conductor, then the associated time-varying magnetic field cannot exist. Since the normal components of the $\mathbf{B}$ fields in both regions must be equal (Equation 105), both normal fields must equal zero. This is summarized by

$$\hat{n} \cdot \mathbf{B}_1 = 0 \tag{106}$$

where $\mathbf{B}_1$ is the magnetic field present at the boundary of the PEC. Therefore, the normal component of the magnetic field at the boundary is zero.

135

# Appendix B

## B.1    cmcomp01.c

/* CMCOMP01.C v4.00 Nov 14,2001

    Input Files:     r_matrix, x_matrix

Output Files:     e_srtd, l_srtd, a_matrix, b_lambda, b_vector, cmvector

    Jan 31,2000 v1.10

This program calculates the eigenvalues and eigenvectors using the algorithm

outlined in "Computation of Characteristic Modes" by Harrington & Mautz

This program relies heavily on the numerical subroutines from the book,

"Numerical Recipes in "C""

Feb 1. 2000 v1.20

Added the ability to determine smallest U and partition the U & A matrices

    Feb 1, 2000 v2.10

Changing the eigenvalues and eigenvector routines to use the "Jacobi" method

instead of the "Givens-Householder" method

Feb 3, 2000 v3.00

Fixed erroneous "cmvector" problem. I was saving the wrong tmp file when

writing out the data to the "cmvector" file. Solved by comparing data for

the half-wavelength dipole example from Mirrata as obtained using the

"b_calc.m" file and using the 'mdump' function.

    Apr 13, 2000 v4.00

136

Modified the file for use with Linux OS. Removed all vestages of the 'mdump' command. Entered several 'printf' commands to monitor the progress of the program

Aug 16,2000 CMCOMP.C v4.00 (CMCOMP01.C v1.00)

This program is modified from the third version of cmcomp.c. The big change is in the calculation of the first eigenvectors and eigenvalues of the 'R_MATRIX'. This is now calculated by first averaging the 'X' and 'R' matrices before being used by this equation. Then the first set of eigen information is determined using the 'svdcmp.c' routine.

Aug 17, 2000 v2.00

After examining the results from output of this program decided to increase the "condition #, M" to 1000000 or .000001

Aug 20, 2000 v2.10

Changed "M" back to 1000 or 0.001. The added accuracy didn't add anything to the calculations.

May 02, 2001 v3.00

Commented out the second "fclose(Rin)" command. This was causing a 'segmentation fault, core dumped'. Recompiled and program now executes successfully.

Nov 14, 2001 v4.00

Changed "M" back to 0.000001 so that it would calculate the characteristic modes to the correct accuracy. Could also increase accuracy by using 'double float' variables.

137

```c
*/

#include <stdio.h>

#include <math.h>

#include <float.h>

#include <stdlib.h>

#include <stddef.h>

#define NR_CHECK

#include "nr.h"

#include "nrutil.h"

/* useful macros */

#define True 1

#define False 0

int main( void )

{

float smallst_u;

int i,j, cols, rows, error, errors;

int N, n, P, M, z_indx, nrot;

FILE *Rin, *Xin; /* data input */

FILE *fptr_1, *fptr_e, *A_out, *B_lambda, *B_vector, *cm_vec; /* data output */

float **u_matrix; /*matrix of inner products and eigenvectors*/

float *w, **a, **v;/* These elements are required for SVD Calculation*/

float **x_matrix, **u_transpose, **a_matrix, **m_tmp1, **m_tmp2;

float **a11, **a12, **a12T, **a22, **a22inv, **u11_12, **u11_12inv;
```

138

```c
float **b_matrix, **ident1, **ident2, **b_eigvec;

float **lambda; /*matrix of eigenvalues*/

float *diag_elem; /*diagonal elements of the tridiagonal matrix

                               and eigenvalues*/

float *off_diag; /*off-diagonal elements */

Rin = fopen("r_matrix","r");

/* Opening the output files for storing sorted eigenvalues and

// eigenvectors*/

if (( fptr_l = fopen("l_srtd", "a+")) == NULL){

        printf("Cannot open the file 'l_srtd'\n");

} else {

        printf("Ready to write to file, 'l_srtd'\n");

        }

if (( fptr_e = fopen("e_srtd", "a+")) == NULL){

        printf("Cannot open the file 'e_srtd'\n");

} else {

        printf("Ready to write to file, e_srtd.\n");

        }

printf("Enter the number of Rows(Columns) in the matrix r_matrix.\n");

scanf("%d",&N); /*Reads in the number of rows and columns*/

printf("The program expects 'r_matrix' to be a %d X %d matrix\n",N,N);

u_matrix=matrix(1,N,1,N);

lambda=matrix(1,N,1,N);
```

139

```c
w=vector(1,N);

a=matrix(1,N,1,N);

v=matrix(1,N,1,N);

rows = cols = N;

printf("Reading the r_matrix —> u_matrix\n");/* r_matrix file read*/

for(i=1;i<=rows;i++){ /*r_matrix -> a -> u_matrix*/

        for(j=1;j<=cols;j++){

                fscanf(Rin,"%f",&a[i][j]);

                u_matrix[i][j] = a[i][j];

                lambda[i][j] = 0;

                }

        }

printf("\n");

printf("read in 'R_Matrix'.\n");

printf("The number of rows = %d \nThe number of cols = %d\n",rows,cols);

fclose(Rin);

printf("Beginning SVD ......\n");

svdcmp(u_matrix,N,N,w,v);

printf("Finished SVD. Now beginning the eigenvalue/eigenvector sorting operation. \n");

/*Sorting the eigenvalues from highest to lowest and rearranging their

        affiliated eigenvectors using numerical recipes routine*/

eigsrt(w,u_matrix,N);

printf("Sorting complete.\n");
```

140

```
/*Priting to file "l_srtd" the sorted eigenvalues

//Fills in "0" for the off-diagonal elements of matrix.

//printf("rows = %d and columns = %d\n",rows,columns);*/

for(i=1;i<=N;i++){

        lambda[i][i] = w[i];

        for(j=1;j<=cols;j++){

                fprintf(fptr_l,"%f ",lambda[i][j]);

        }

        fprintf(fptr_l,"\n");

    }

printf("Sorted eigenvalues.\n");

for(i=1;i<=rows;i++){

    for(j=1;j<=cols;j++){

        fprintf(fptr_e,"%f ",u_matrix[i][j]);

        }

    fprintf(fptr_e,"\n");

    }

printf("Sorted eigenvectors.\n");

/*Determining the smallest 'u' and deterimining partition size for

the 'U' and 'A' matrices */

/*Changed the folloing value from 0.001 to 0.000001 */

smallst_u = 0.000001*lambda[1][1];

for(n=2;n<=N;n++){
```

141

```c
        if(lambda[n][n] < smallst_u){

            lambda[n][n] = 0;

            M = n-1;

            break;

        }

    }

    P = N - M;

    printf("M = %d\nN = %d\nP = %d\n",M,N,P);

    z_indx = M + 1;

    /* Setting rest of U elements, past the smallest U, to zero*/

    for(n=z_indx;n<=N;n++){

        lambda[n][n] = 0;

    }

    /* Read in the `X` matrix*/

    x_matrix=matrix(1,N,1,N);

    Xin = fopen("x_matrix","r");

    printf("Reading the x_matrix —> x_matrix\n");

    for(i=1;i<=rows;i++){

            for(j=1;j<=cols;j++){

                fscanf(Xin,"%f ",&x_matrix[i][j]);

            }

    }

    printf("Read in `X_Matrix`.\n");
```

142

```
u_transpose=matrix(1,N,1,N);

printf("Calculating U transpose'.\n");

mtranspose(u_matrix,N,N,u_transpose);  /*Calculates U-transpose, U' */

m_tmp1=matrix(1,N,1,N);

a_matrix=matrix(1,N,1,N);

printf("Calculating X*U .\n");

mmult(x_matrix,N,N,u_matrix,N,N,m_tmp1);  /* X*U */

printf("Calculating X*U .\n");

mmult(u_transpose,N,N,m_tmp1,N,N,a_matrix);  /* A = U'*X*U */

free_matrix(u_transpose,1,N,1,N);

free_matrix(m_tmp1,1,N,1,N);

A_out = fopen("A_matrix","a+");

for(i=1;i<=rows;i++){

        for(j=1;j<=cols;j++){

                fprintf(A_out,"%f ",a_matrix[i][j]);

        }

        fprintf(A_out,"\n");

}

printf("Beginning calculation of A11, A12, A12T, & A22 .\n");

/* Compute the A11, A12, A12T, & A22 matrices*/

a11=matrix(1,M,1,M);

a12=matrix(1,M,1,P);

a12T=matrix(1,P,1,M);
```

143

```
a22=matrix(1,P,1,P);

/*Calculate 'A11'*/

for(i=1;i<=M;i++){

    for(j=1;j<=M;j++){

        a11[i][j] = a_matrix[i][j];

    }

}

printf("Calculating of A12 .\n");

/*Calculate 'A12'*/

for(i=1;i<=M;i++){

    for(j=1;j<=P;j++){

        a12[i][j] = a_matrix[i][M+j];

    }

}

printf("Calculating of A12T .\n");

mtranspose(a12,M,P,a12T); /*Calculates 'A12' transpose*/

printf("Calculating of A22 .\n");

/*Calculate 'A22'*/

for(i=1;i<=P;i++){

    for(j=1;j<=P;j++){

        a22[i][j] = a_matrix[M+i][M+j];

    }

}
```

144

```c
printf("Initializing the U^(-1/2) matrix .\n");

u11_12inv=matrix(1,M,1,M); /* Generate the U^(-1/2) matrix*/

for(i=1;i<=M;i++){

    for(j=1;j<=M;j++){

        u11_12inv[i][j] = 0;

    }

}

printf("Calculating the diagnonal elements of U11_12INV .\n");

for(i=1;i<=M;i++){

    u11_12inv[i][i] = 1/(sqrt(lambda[i][i]));

}

free_matrix(lambda,1,N,1,N);

printf("Inverting A22 .\n");

a22inv = matrix(1,P,1,P);/* Inverting A22*/

inverse(a22,P,a22inv);

free_matrix(a22,1,P,1,P);

printf("Inversion of A22 complete\n");

/* Calculation of 'B'*/

printf("Calculating A12*A22inv*A12T .\n");

m_tmp1=matrix(1,P,1,M); /* Calculating A12*A22inv*A12' */

mmult(a22inv,P,P,a12T,P,M,m_tmp1);

m_tmp2 = matrix(1,M,1,M);

mmult(a12,M,P,m_tmp1,P,M,m_tmp2);
```

145

```
free_matrix(a12,1,M,1,P);

free_matrix(m_tmp1,1,P,1,M);

m_tmp1 = matrix(1,M,1,M);

printf("Calculating A11 - A12*A22inv*A12T .\n");

msub(a11,M,M,m_tmp2,m_tmp1); /* Calculating A11 - A12*A22inv*A12'*/

free_matrix(m_tmp2,1,M,1,M);

free_matrix(a11,1,M,1,M);

printf("Calculating (A11 - A12*A22inv*A12T)*U11_12INV .\n");

m_tmp2 = matrix(1,M,1,M); /*(A11 - A12*A22inv*A12')*u11_12inv*/

mmult(m_tmp1,M,M,u11_12inv,M,M,m_tmp2);

free_matrix(m_tmp1,1,M,1,M);

printf("Calculating U11_12INV*(A11 - A12*A22inv*A12T)*U11_12INV .\n");

b_matrix=matrix(1,M,1,M); /*u11_12inv*(A11 - A12*A22inv*A12')*u11_12inv */

mmult(u11_12inv,M,M,m_tmp2,M,M,b_matrix);

free_matrix(m_tmp2,1,M,1,M);

lambda=matrix(1,M,1,M); /*Eigenvalues and vectors of 'B' */

diag_elem=vector(1,M);

off_diag=vector(1,M);

printf("Storing B_matrix values into B_vector.\n");

B_vector = fopen("b_vector", "a+");

for(i=1;i<=M;i++){

        for(j=1;j<=M;j++){

               fprintf(B_vector,"%f ",b_matrix[i][j]);
```

146

```
                  }

                  fprintf(B_vector,"\n");

      }

      b_eigvec = matrix(1,M,1,M);

      mcopy(b_matrix,M,M,b_eigvec);

      tred2(b_eigvec, M, diag_elem, off_diag);

      printf("finished tridagonal matrix of B\n");

      tqli(diag_elem, off_diag, M, b_eigvec);

      printf("finished tridagonal QL implicit of B\n");

      printf("Storing B_lambda values .\n");

      B_lambda = fopen("b_lambda", "a+");

      for(i=1;i<=M;i++){

                  fprintf(B_lambda,"%f ",diag_elem[i]);

            }

      printf("Storing B_eigenvecor values in B_vector.\n");

      for(i=1;i<=M;i++){

            for(j=1;j<=M;j++){

            fprintf(B_vector,"%f ",b_eigvec[i][j]);

            }

            fprintf(B_vector,"\n");

      }

      /* Calculation of the final equation in Harrington & Mautz to find the

            eigenvectors that correspond to the smaller eigenvalues of the original
```

147

```
        'R' matrix.

*/

printf("Calculating the final matrices to generate 'cmvector' elements .\n");

ident1 = matrix(1,N,1,M); /*Generate a M x M identity matrix in top submatrix*/

for(i=1;i<=M;i++){

    for(j=1;j<=M;j++){

        ident1[i][j]= 0;

    }

ident1[i][i] = 1;

}

ident2 = matrix(1,P,1,M);

mmult(a22inv,P,P,a12T,P,M,ident2);

for(i=1;i<=P;i++){

    for(j=1;j<=M;j++){

        ident1[i+M][j] = -(ident2[i][j]);

    }

}

m_tmp1 = matrix(1,M,1,M);

mmult(u11_12inv,M,M,b_eigvec,M,M,m_tmp1);

m_tmp2 = matrix(1,N,1,M);

mmult(ident1,N,M,m_tmp1,M,M,m_tmp2);

free_matrix(m_tmp1,1,M,1,M);

m_tmp1 = matrix(1,N,1,M);
```

148

```c
mmult(u_matrix,N,N,m_tmp2,N,M,m_tmp1);

cm_vec = fopen("cmvector","a+");

printf("Opened the cmvector file\n");

for(i=1;i<=N;i++){

    for(j=1;j<=M;j++){

        fprintf(cm_vec,"%f ",m_tmp1[i][j]); /*This should be m_tmp1? */

    }

    fprintf(cm_vec,"\n");

}

fclose(Xin);

fclose(cm_vec);

fclose(B_vector);

fclose(A_out);

fclose(fptr_l);

fclose(fptr_e);

return 0;

}

fclose(Xin);

fclose(cm_vec);

fclose(B_vector);

return 0;(fptr_e);(fptr_l);(A_out);

fclose(fptr_l);

fclose(fptr_e);
```

149

```
        return 0;

    }
```

# Appendix C

## C.1 pwrplt05.m

%PwrPlt05.m Oct 26,2001 v5.00

%Input File: e_fld.dat

%Output File: stdout

%

%This file will read in the data from the file 'e_fld.dat'

%This data file is produced from 'efield02.c'

%The user selects which plane they would like to view and the

%data is plotted in polar form. The center value of the circle

%is the greatest negative value dB in the 'e_fld.dat' file.

%This file is based on 'EthtPlt.m'

% Note the value of -999dBi has been translated to zero. ie all

% values are increased by 999

%Oct 26,

%This version was changed to only do 0->180 deg theta for a given

% phi cut.

clear

f_name = input('Enter the name of the "e_fld.dat" file ');

e_field = fopen(f_name,'r');

cols = 9;

151

```
theta_cnt=input('Enter the # theta measurments. ');

phi_cnt=input('Enter the # of phi measurments. ');

rows = (theta_cnt + 1) * (phi_cnt + 1);

E = fscanf(e_field,'%f',[cols,rows]);

vec = E';

disp('column 3: Power in Theta directed E-Field')

disp('column 6: Power in Phi directed E-Field')

disp('column 9: Total power in the E-Field')

disp('Select the desired type of E-field power, i.e. 3, 6 or 9')

col=input('The desired type is ');

disp('For power pick 1, for electric field pick 2')

pwr_type=input('Pwr or V/m, 1 or 2 respectively ')

%Now choose the free variable and the fixed variable

%between theta and phi

disp('Enter the independent angle')

disp('theta or phi, the other variable shall be where the ang. slice')

disp('is made through the pattern')

disp('The independent variable: Theta or phi ,1 or 2, respectively')

free_angle=input('The independent variable is ')

if free_angle == 1

phi_cut=input('Enter the phi cut angle,0—>360,in increments of 10 ');

phi_inc = 10; %Remember to enter the smaller of the two phi-cut

tht_inc = 10;
```

```
        phi_cut = phi_cut/phi_inc;%To determine where to begin theta set

        row_indx = (theta_cnt + 1)* phi_cut;

        end_cnt = theta_cnt + 1;

        rng = 999

for t = 1:end_cnt

rw = row_indx + t;

if pwr_type == 1

tmp_E(t) = vec(rw,col);

else

tmp1 = vec(rw,(col+1));

tmp2 = vec(rw,(col+2));

z_fld = complex(tmp1,tmp2);

ang_z(t) = (180/pi)*(angle(z_fld));

tmp_E(t) = sqrt(tmp1^2 + tmp2^2);

end

end

%%%%%%

%%%END OF FIRST HALF OF PHI CUT PLOT

%%%%%%%

%%%%%%%%%%

%%

%Do the following if this is a THETA cut

%%%%
```

153

```
else

%The free variable is phi. Phi varies from 0-360 degrees

tht_cut=input('Enter the theta cut plane , 0 <= theta <= 180 ');

        tht_inc = 10; %Remember to enter the smaller of the two phi-cut

                        %angles so 180 + phi_cut <= 360

        tht_cut = tht_cut/tht_inc;%To determine where to begin theta set

        end_cnt = phi_cnt + 1;

for p = 1:end_cnt

tht_grp = 19 * (p-1);

rw = (tht_grp + tht_cut + 1);

if pwr_type == 1

tmp_E(p) = vec(rw,col);

else

tmp1 = vec(rw,(col+1));

tmp2 = vec(rw,(col+2));

z_fld = complex(tmp1,tmp2);

ang_z(p) = (180/pi)*(angle(z_fld));

tmp_E(p) = sqrt(tmp1^2 + tmp2^2);

end

end

end

subplot(2,1,1); plot(tmp_E')

subplot(2,1,2); plot(ang_z')
```

154

# BIBLIOGRAPHY

[1] S. Ponnanpalli and F. Canora, "Whip antenna design for portable RF systems," *Proceedings of SPIE - The International Society for Optical Engineering, v 2601*, pp. 32–40, 1995.

[2] S. Ponnapalli, "Modeling and design of antennas for RF wireless systems," *IEEE Transactions on Components, Packaging, and Manufacturing Technology-Part B.*, vol. 19, pp. 487–502, Aug. 1996.

[3] S. L. A.W.C. Chu and D. Wilton, "The radiation pattern of a monopole antenna attached to a conducting box," *IEEE Transactions on Antennas and Propagation*, vol. 38, pp. 1907–1912, Dec. 1990.

[4] V. Austin and K. Murray, "The application of characteristic-mode techniques to vehicle-mounted NVIS antennas," *IEEE Antennas and Propagation Magazine*, vol. 40, pp. 7–21, Feb. 1998.

[5] E. Newman, "Small antenna location synthesis using characteristic modes," *IEEE Transactions on Antennas and Propagation*, vol. AP-27, pp. 530–531, Jul. 1979.

[6] R. Harrington, *Field Computation by Moment Methods*. Robert E. Krieger Publishing Company, INC., 1982.

[7] C. Balanis, *Advanced Engineering Electromagnetics*. John Wiley and Sons, 1989.

[8] W. Stutzman and G. Thiele, *Antenna Theory and Design*. John Wiley & Sons, Inc., 1998.

[9] J. Wang, *Generalized Moment Methods in Electromagnetics*. John Wiley & Sons, Inc., 1991.

[10] R. Harrington and J. Mautz, "Theory of characteristic modes for conducting bodies," *IEEE Transactions on Antennas and Propagation*, vol. AP-19, pp. 622–628, Sep. 1971.

[11] R. Garbacz, *A generalized expansion for radiated and scattered fields*. PhD thesis, Ohio State University, Columbus, 1971.

[12] R. Garbacz and R. Turpin, "A generalized expansion for radiated and scattered fields," *IEEE Transactions on Antennas and Propagation*, vol. AP-19, pp. 348–358, May 1971.

[13] R. Harrington and J. Mautz, "Computation of characteristic modes for conducting bodies," *IEEE Transactions on Antennas and Propagation*, vol. AP-19, pp. 629–639, Sep. 1971.

[14] K. Murray, *The Design of Antenna Systems on Complex Structures Using Characteristic Modes*. PhD thesis, University of Liverpool, 1993.

[15] A. Poggio and E. Miller, "Integral equation solution of three dimensional scattering problems," in *Computational Techniques for Electromagnetics* (R. Mittra, ed.), ch. 4, Pergamon, 1973.

[16] G. Thiele, *Computer Techniques for Electromagnetics*. Pergamon Press, 1973.

[17] K. Fujimoto, "Some considerations of small antenna measurements," in *Analysis, Design, and Measurement of Small and Low-Profile Antennas* (K. Hirasawa and M. Haneishi, eds.), ch. 9, Artech House, 1992.

[18] R. A. of Austin Antenna, 1998. Private Communication.

[19] J. C. L. J. W. Rockway, "Expert mininec series wire antenna modeling codes."

[20] J. T. Mayhan, "Characteristic modes and wire grid modeling," *IEEE Transactions on Antennas and Propagation*, vol. 38, pp. 457–469, April 1990.

[21] A. C. Ludwig, "Wire grid modeling of surfaces," *IEEE Transactions on Antennas and Propagation*, vol. 35, pp. 1045–1048, Sept. 1987.

155

[22]   J. Rockway. Private communication, 2001. EM Scientific INC.

[23]   C. Balanis, *Antenna Theory Analysis and Design*. John Wiley & Sons, Inc., 1997.